Noise spectroscopy with large clouds of cold atoms

Samir Vartabi Kashanian

UNIVERSITE DE NICE-SOPHIA ANTIPOLIS
UFR Sciences

Ecole Doctorale
Sciences Fondamentales et Appliquées

THESE

pour obtenir le titre de

Docteur en Sciences

de l'Université de Nice - Sophia Antipolis
Discipline : PHYSIQUE

présentée et soutenue par

Samir VARTABI KASHANIAN

Noise Spectroscopy with Large Clouds of Cold Atoms

Thèse dirigée par: Robin KAISER
Michel LINTZ

soutenue le 16 Septembre 2016

Jury :

Dr.	Robin KAISER	-	Directeur de thèse
Pr.	Farrokh VAKILI	-	Président du jury
Pr.	Frank SCHEFFOLD	-	Rapporteur
Dr.	Christoph WESTBROOK	-	Rapporteur
Dr.	Caroline CHAMPENOIS	-	Examinateur
Pr.	Gian-Luca LIPPI	-	Examinateur

Abstract:
In this thesis, I present some measurements of fluctuations of light after interaction with a cloud of laser-cooled rubidium atoms. These measurements can provide useful information on the source itself as well as on the medium in which light propagates. I address a particular configuration in which intensity noise are measured on a laser beam transmitted through the atomic cloud. This geometry is relevant to investigate different properties, such as the atomic motion. However, in our experiment the intrinsic noise of the incident laser has an important contribution to the detected noise spectrum. This technical noise may be hard to distinguish from the signal under study and a good understanding of this process is thus essential.

Experimentally, the intensity noise spectra show a different behavior for low and high Fourier frequencies. Whereas one recovers the "standard" frequency to intensity conversion at low frequencies, due to the atomic resonance as a frequency discriminator, some differences appear at high frequencies. We show that a mean-field approach, which corresponds to describing the atomic cloud by a dielectric susceptibility, is sufficient to explain the observations. Using this model, the noise spectra allow to extract some quantitative information on the laser noise as well as on the atomic sample. This is known as noise spectroscopy.

The perspective of this thesis aims at applying noise measurement to obtain complementary signatures of the cold-atom random laser by studying the temporal coherence of the emitted light. The manuscript therefore outlines a review on random laser phenomena with a focus on cold-atom random lasers and its coherence properties.

KEY-WORDS : Cold atom, noise spectroscopy, random laser

Résumé:
Dans cette thèse je présente des mesures de fluctuations de la lumière après propagation dans un nuage d'atomes de rubidium refroidi par laser. Ces mesures fournissent des informations sur la source et sur le milieu de propagation. Je considère une configuration particulière en transmission, le laser se propageant au travers du nuage atomique. Cette géométrie est pertinente pour étudier différentes propriétés, comme le mouvement des atomes. Cependant, le bruit intrinsèque du laser a une contribution importante sur les spectres de bruit. Ce bruit technique peut alors devenir gênant pour extraire le signal étudié et une bonne compréhension du phénomène est donc essentielle.

Expérimentalement, les spectres de bruit en intensité montrent un comportement différent aux fréquences basses et hautes. Alors que l'on observe la conversion "standard" du bruit de fréquence en bruit d'intensité pour les fréquences basses, la résonance atomique correspondant à un discriminateur de fréquence, des différences apparaissent à hautes fréquences. Nous montrons qu'une approche de champ moyen, en associant une susceptibilité électrique au nuage atomique, est suffisante pour expliquer les observations. Partant de ce modèle, les spectres permettent d'extraire des informations quantitatives sur le laser et sur le nuage atomique. Ceci est connu sous le nom de spectroscopie de bruit.

La perspective est d'utiliser ces mesures de bruit afin d'obtenir une signature claire du laser aléatoire à atomes froids en étudiant la cohérence temporelle de la lumière émise. Cette thèse expose une revue du phénomène de laser aléatoire, en particulier sur le laser à atomes froids et ses propriétés de cohérence.

Mots-clés : atomes froids, la spectroscopie de bruit, laser aléatoire

Résumé

Le laser aléatoire

L'idée du laser aléatoire a été proposée par Letokhov, qui a étudié la propagation de la lumière en présence d'amplification (ou gain) dans un milieu fortement diffusant. Dans une telle situation, la diffusion multiple augmente la longueur effective du chemin dans le milieu à gain et donc augmente l'effet d'amplification. Letokhov développa un modèle théorique basé sur l'équation de diffusion et obtint un seuil sur la taille du système au-delà duquel l'amplification dans le volume du milieu surpasse les pertes à la surface, provoquant une augmentation exponentielle de l'intensité de la lumière piégée dans le milieu, et par conséquent de la lumière émise. Cela est très similaire au principe d'un laser, qui oscille lorsque le gain produit par le milieu amplificateur surpasse les pertes de la cavité. Ici, la cavité est remplacée par le piégeage de radiation dû à la diffusion multiple. Les propriétés des modes spatiaux et spectraux sont donc différentes des lasers standard.

Des lasers aléatoires ont été observés dans différents milieux, dont des lasers à colorant, des poudres de semi-conducteurs, des céramiques, des films minces nanostructurés ou non, etc. Récemment, un laser aléatoire basé sur des atomes froids a été obtenu dans notre équipe, en utilisant des atomes de rubidium refroidis dans un piège magnéto-optique (PMO). Ici les atomes froids fournissent à la fois le gain et la diffusion multiple. Dans ce système, le gain est obtenu par une transition Raman à deux photons entre les états hyperfins du niveau fondamental. La fréquence du laser Raman peut être choisie telle que le laser lui-même soit peu diffusé par les atomes et que la fréquence de gain soit résonante avec une transition procurant de la diffusion.

Les lasers aléatoires sont généralement basés sur une excitation impulsionnelle et sur des matériaux solides ou liquides. Un fonctionnement quasi-continu et utilisant une vapeur atomique sont deux particularités du laser aléatoire à atomes froids. Ces deux propriétés seraient également une caractéristique des lasers aléatoires naturels *"astrophysique"*, dont

l'existence n'est juste qu'une hypothèse à l'heure actuelle.

Motivations

Différencier l'émission d'un laser aléatoire parmi d'autres source de radiation, d'objets astrophysiques par exemple, nécessite de développer de nouvelles techniques de mesure. En particulier, dans le cas du laser aléatoire basé sur des atomes froids, développé à l'INLN, il est difficile de séparer spectralement ou spatialement la lumière du laser des autres lumières diffusées. Plus précisément, il y a quatre raies séparées de quelques dizaines de megahertz et l'émission du laser aléatoire est l'une d'elle.

Les propriétés de cohérence temporelle et spatiale permettent de caractériser et de classifier une source inconnue de lumière. Plusieurs travaux théoriques et expérimentaux ont démontré que, en générale, l'émission d'un laser aléatoire est partiellement cohérente. Cependant cette cohérence est généralement inférieure à celle d'un laser conventionnel. Ces propriétés de cohérence dépendent des paramètres expérimentaux et du matériau utilisé, et peuvent être très différentes d'une expérience à l'autre. A cause de la complexité de la situation due à la diffusion multiple, les propriétés de cohérence des lasers aléatoires ne sont pas complètement connues et restent donc une question ouverte.

Le but à long terme de ce travail est de caractériser la cohérence temporelle du laser aléatoire à atomes froids. Cela pourrait en particulier fournir une nouvelle signature du seuil du laser. La cohérence de la lumière diffusée par des atomes froids a déjà été étudiée dans plusieurs expériences en régime de diffusion simple, ce qui nous fournit des exemples de techniques de mesure applicables à notre cas. Afin d'aller pas à pas vers l'implémentation et l'exploitation de ce genre de techniques et de les appliquer au laser aléatoire, la première étape est d'abord de caractériser le bruit intrinsèque dû aux lasers utilisés dans l'expérience, et l'impact de ce bruit sur les mesures futures. Ensuite, nous pourrons étudier la cohérence temporelle de la lumière en diffusion multiple dans le nuage d'atomes. Enfin, nous étudierons l'effet de l'ajout de gain dans le système et du franchissement du seuil du laser aléatoire.

Travail de cette thèse

Dans ce contexte, cette thèse présente une étude détaillée sur le bruit de la lumière diffusée vers l'avant par un nuage d'atomes froids. Une partie de mon travail durant ces trois dernières années a consisté à manipuler et amélioré le dispositif expérimental d'atomes froids. Nous avons installé un montage de détection du bruit en transmission afin

d'étudier le bruit induit par les atomes froids sur un faisceau laser sonde traversant le nuage. Nous avons d'abord caractérisé les bruits du laser ainsi que la forme et la largeur de son spectre, puis nous avons étudié l'effet du bruit de fréquence et du bruit d'intensité du laser sur le bruit en transmission. En utilisant un modèle simple, nous avons démontré la spectroscopie de bruit sur un niveau hyperfin dans un gros nuage d'atomes froids.

Au chapitre 2 de ce manuscrit, nous introduisons plus en détail le laser aléatoire. Il s'agit d'un laser basé sur un milieu à gain très désordonné. Comme il n'y a pas de cavité optique, les modes spatiaux et spectraux sont complètement différents de ceux des lasers conventionnels. La diffusion multiple produit la rétroaction et détermine les modes émis. Bien que des travaux théoriques et expérimentaux aient montré que l'émission des lasers aléatoires est partiellement cohérente, cette cohérence est réduite par rapport aux lasers standard. A cause de la complexité de la diffusion multiple, il n'y a pas encore de théorie précise de la cohérence des lasers aléatoires, et des études complémentaires sont donc nécessaires dans ce domaine. Bien que le laser aléatoire à atomes froids ait été observé dans notre équipe, des mesures de la cohérence pourraient apporter une observation plus directe.

Au chapitre 3 nous décrivons notre dispositif expérimental de production d'atomes froids. Nous avons un piège magnéto-optique de rubidium 85 contenant $\sim 10^10$ atomes, avec une épaisseur optique $b_0 = 100$, une taille $\sigma = 1$ mm et une température de 100 μK. Nous avons installé un nouveau système d'asservissement laser, dit "offset-lock", afin de stabiliser et contrôler la fréquence du laser des faisceaux de refroidissement et des faisceaux pompe et sonde. L'avantage de ce système est qu'il permet de balayer la fréquence du laser sur une grande plage tout en maintenant l'intensité constante, ce qui est particulièrement important pour le faisceau Raman du laser aléatoire. De plus, plusieurs informations techniques utiles sur le contrôle et la caractérisation du PMO sont données.

Pour comprendre le bruit ajouté par les atomes sur un faisceau laser se propageant à travers le PMO, il est nécessaire de d'abord caractériser les bruits intrinsèques existant dans le faisceau incident. Ces bruits peuvent évoluer de manière non triviale et être convertis en d'autres types de bruit par l'interaction avec les atomes. En appliquant la méthode dite de la "ligne de séparation β", la largeur spectrale du laser a pu être estimée à partir de la puissance spectrale du bruit de fréquence, elle-même mesuré grâce à la conversion du bruit de fréquence en bruit d'intensité lorsque le faisceau est transmis sur le flanc d'une résonance d'une cavité Fabry-Perot. Le résultat a ensuite été confirmé par une mesure de battement avec un laser plus fin.

De manière similaire, le bruit de fréquence du laser peut être mesuré

en utilisant la résonance atomique comme filtre fréquentiel. Au chapitre 4 nous discutons nos mesures de bruit de fréquence utilisant le PMO. L'effet Doppler est négligeable et les transitions hyperfines peuvent convertir les fluctuations de fréquence du laser incident en fluctuation d'intensité. Une propriété intéressante des atomes froids est qu'en contrôlant l'épaisseur optique du nuage on peut changer l'efficacité de cette conversion du bruit de fréquence en bruit d'intensité. C'est un peu analogue à changer la largeur d'une cavité optique. De même que dans le cas de la cavité Fabry-Perot, nous avons mesuré le bruit de fréquence du laser et appliqué la méthode de la ligne de séparation β. L'estimation résultante de la largeur spectrale du laser est en accord avec les autres résultats.

Les larges ailes du spectre optique du laser peuvent être considérées comme un balayage de fréquence. On peut donc réaliser de la spectroscopie avec une fréquence laser fixe. Cette technique est nommée spectroscopie de bruit. Le bruit de la transmission du laser à travers le nuage d'atomes froids est modélisé en supposant que le bruit du laser incident comporte une modulation de phase. Les bandes latérales qui en résultent simulent la largeur spectrale. Une modulation d'amplitude produit également des bandes latérales qui pourraient aussi décrire la spectroscopie de bruit. Cependant les résultats des deux modèles sont qualitativement différents. En les comparant aux résultats expérimentaux nous obtenons que le modèle basé sur la modulation de phase est en très bon accord, mais ce n'est pas le cas avec celui basé sur la modulation d'amplitude. Cela démontre que la spectroscopie de bruit nous renseigne sur la nature du bruit du laser incident. Nous démontrons également que la spectroscopie de bruit donne aussi des informations sur l'échantillon atomique, par exemple son épaisseur optique. La compréhension qualitative et quantitative de la conversion du bruit de fréquence en bruit d'intensité par le nuage sera utile pour toute expérience où un faisceau laser est détecté après transmission à travers un nuage d'atomes froids, même si le modèle présenté dans cette thèse ne prend pas en compte les sous-niveaux Zeeman.

Perspective

Plusieurs techniques de mesure de la cohérence ont déjà été implémentées dans la communauté des atomes froids pour caractériser la diffusion de la lumière par un PMO en régime de diffusion simple. Afin de comprendre les propriétés de cohérence du laser aléatoire à atomes froids, nous proposons de commencer par étudier les propriétés de cohérence de la lumière ayant subi de la diffusion multiple dans le nuage d'atomes froids. Il s'agit en fait d'appliquer la technique dite de spectroscopie d'onde diffusée (*diffusive wave spectroscopy*, DWS), qui permet de sonder les déplacements des diffuseurs avec une très grande précision grâce à la dynamique de la lumière diffusée

en régime de diffusion multiple. Comme le DWS est sensible à de petits déplacements et dépend du nombre moyen d'évènements de diffusion, toute variation de température ou d'épaisseur optique entraine un changement significatif du résultat. En pratique, il s'agit d'effectuer une mesure de la fonction d'autocorrélation d'intensité temporelle. L'évolution du temps de cohérence en fonction de l'épaisseur optique pourrait contenir une information pertinente sur l'impact du seuil laser sur la cohérence du laser aléatoire. Cette mesure pourra être effectuée en régime de comptage de photons.

Une autre mesure intéressante peut être effectuée en étudiant la statistique de photon du laser aléatoire à atomes froids. Comme montrée par Cao et al., les statistiques de photons en-dessous et au-dessus du seuil laser sont respectivement des lois de Bose-Einstein et de Poisson.

Acknowledgments

The research included in this dissertation could not have been performed if not for the assistance, patience, and support of many individuals. I would like to extend my sincere gratitude to my thesis supervisor Robin Kaiser for his continuous support during my PhD study. His insight leads to the proposal of noise spectroscopy with cold atoms. I would like to cordially thank my co-supervisor Michel Lintz for his support in both the research and especially the revision process that has lead to this document.

Besides my supervisors, I would like to thank the rest of my thesis committee: Dr. Christoph Westbrook, Prof. Frank Scheffold, Prof. Farrokh Vakili, Dr. Caroline Champenois and Prof. Gian-Luca Lippi, for their insightful comments.

I am also grateful to my collaborators for their contributions to this thesis. I acknowledge William Guerin, for mentoring me over the basis and principles of the cold-atom experiment. He has helped me over the writing of the dissertation and for that I sincerely thank him. This research would not have been possible without the assistance of Mathilde Fouché. for her support in both the modeling and data analysis and furthermore for the revision process that has lead to this document. Her knowledge and understanding of the written word has allowed me to fully express the concepts behind this research. I would additionally like to thank Aurélian Eloy for his collaboration in the experiment and data acquisition. Moreover for pursuing this project towards the characterization of cold-atom random laser. I wish him a successful and productive PhD program.

I would also like to extend my appreciation to all my colleagues, officemate and friends at INLN and in OCA for their supports. I would have difficulty to complete all the administrative work without the help of David Andrieux and all the secretaries at INLN.

A special thank to Patrizia Vignolo for mentoring me over numerical computations in the field of optics and atomic physics and for a fruitful collaboration which leads to this PhD program.

Finally, I would like to extend my deepest gratitude to my parents Mina Azimi and Ahmad Vartabi Kashanian, my parents in law Fatemeh Jafari and Morteza Khorrami, my amazing sister Sama, and kind sister and brothers in law Zahra, Hooman and Amir without whose love, support and understanding I could never have completed this doctoral degree. At the

end I appreciate my beloved Zeinab for her extreme support through all the difficult times. No words can describe how grateful I am for her endless love and patience and confidence in me.

This research was supported financially in part by the directors of OCA: Farrokh Vakili and Thierry Lanz.

Contents

List of Figures

List of Tables

Chapter 1

Introduction

Random laser

The idea of random lasing was first proposed by Letokhov who considered the propagation of light in the presence of amplification or gain in a multiple scattering medium [1]. In such a situation, multiple scattering increases the effective path length in the gain medium and thus enhances light amplification. Letokhov developed a theoretical model based on the diffusion equation and he defined a threshold on the system size above which the amplification in the volume overcomes losses at the surface of the medium, leading to an exponential increase of the light intensity trapped in the medium and hence of the subsequent emitted light [1, 2]. This is very similar to the principle of a laser, which starts oscillation when the gain produced by the amplifying medium overcomes the cavity losses. Here, the cavity is replaced by radiation trapping due to multiple scattering [3], and therefore the spatial and spectral lasing modes are different.

Random laser has been observed in many different media including laser dyes, semiconductor powders, ceramics, nanostructured and non-nanostructured thin films, etc [2]. Recently cold-atom random laser was also observed in our team [4] by investigation of the level of fluorescence from the atoms. The rubidium atoms are cooled in a magneto-optical trap (MOT). Here the cold atoms provide both gain and multiple scattering. In this system, a two-photon Raman transition between the hyperfine atomic levels provides gain. Considering the hyperfine structure of the rubidium atoms, the frequency of the laser which makes this Raman transition can be tuned, where the scattering of the laser by the atoms is minimized and simultaneously the scattering of the induced gain is maximized.

State-of-the-art random lasers are usually based on pulsed excitation of condensed matter systems and quasi cw operation of random lasing in dilute atomic vapors had not been realized prior to our recent study [4].

Motivations

Existence of a natural laser emission has long been an open question for scientists. Astronomical observations in the microwave domain have led to the discovery of anomalously bright emission lines from molecules in stellar atmospheres [5]. Moreover spectroscopic data from the atmosphere of planet Mars and planet Venus revealed an extraordinary emission line in infrared

(IR) domain ($\lambda \sim 10\,\mu m$) from CO_2 molecules [6, 7]. Much later, this type of emission was also observed in stellar atmospheres in the far IR [8]. This amplification by stimulated emission in Mars was first observed by Charles Townes' team [6], and later identified as a "natural laser". It was used later as a diagnostic probe of the temperature and wind patterns on Venus [9]. Due to the low densities of the lasing species in the mesosphere and thermosphere of Mars the gain is low, comparable to single-pass gains in some earth based CO_2 lasers [7]. The low gain though is partly compensated by the extremely large volumes of active lasing medium.

It should be noted here that astrophysicists often call "lasers" what a laser physicist would describe as amplification, or Amplified Spontaneous Emission (ASE) [10].

Owing to the huge amount of gain medium in combination with very intense sun light in the Venus atmosphere, scientists in NASA proposed an ambitious project [11]. They designed some satellites carrying mirrors to be located around the Venus atmosphere in order to enhance natural lasing emission for interstellar communication. This was a part of the program *"search for extraterrestrial intelligence" (SETI).* However this proposal was never implemented.

Discriminating the random laser emission among all the other sources of radiation from an astronomical object for instance, requires well-developed knowledge and measurement techniques. In particular, for the case of cold-atom random lasing developed at INLN, it is very difficult to resolve random laser spectrally and spatially among all the other emitted or scattered light. In fact there are at least four spectral lines which are separated by 10s of MHz and random laser emission has to be resolved amongst them.

Temporal and spatial coherence are strong tools which can potentially help to better understand and also to classify an unknown source of light emission. Several theoretical and experimental efforts demonstrated that, in general, random lasing emission is partially coherent [12, 13]. However its coherence is usually less compared with the conventional lasers [14]. These coherence properties depend on the experimental parameters and material used, and could be different from one experiment to the other. However, due to very complicated mechanism of multiple scattering, the coherence of random laser is not completely known and it seems an open question.

The long term goal of this work is to characterize the temporal coherence properties of the cold-atom random laser. This can help to distinguish the lasing modes and threshold condition. The coherence of the scattered light through the cold atoms in the single scattering regime has been already investigated in some experiments [15, 16, 17], which provides us with solid applicable coherence measurement techniques and physics beyond it. Nevertheless to approach step by step coherence measurement and analysis

of a cold-atom random laser, we should first fully characterize the intrinsic noise existing in the laser used in this experiment and its impact on our future measurements. Next, we have to study the coherence of multiple scattered light. Finally, the impact of adding gain has to be taken into account below and above the lasing threshold.

Thesis outline

The content of this thesis is organized as follows. In chapter 2 we introduce the "random laser" phenomena. The results of some theoretical and experimental research on the coherence properties of random laser are summarized briefly. Then the prior observation of cold-atom random laser is also reported, and some possible experimental techniques for studying its coherence properties, which can be possibly applied in cold-atom random laser, are introduced.

In chapter 3, we explain the current status of our ^{85}Rb MOT experiment. Furthermore some experimental and technical informations will be provided about characterizing and modifying the important physical parameters such as temperature, density, and optical thickness.

Finally, in chapter 4 we characterize the lasers used for probing the cold atoms. These properties include laser line shape and linewidth, intensity and frequency noise. Then, using those information, we study the noise power spectral density (PSD) of a laser beam transmitted through the cold atoms. In order to understand the noise features, two models based on phase and amplitude modulation are introduced and compared with the experimental results.

Chapter 2

RANDOM LASER

Two fundamental ingredients of a conventional laser are an amplifying material, which provides optical gain, and an optical cavity that partially traps the light and induces feedback. When the total gain overcomes the losses, the system reaches a threshold and lasing occurs. The mode properties of a laser are determined by the cavity, i.e. the frequency and directionality of the output light. Similar to a conventional laser, random lasers are based on the same principles, but here it is multiple scattering that induces feedback and determines the lasing modes instead of the cavity (Fig. 2.1). The term "random laser" was introduced and suggested in 1995 by Wiersma et. al. [18].

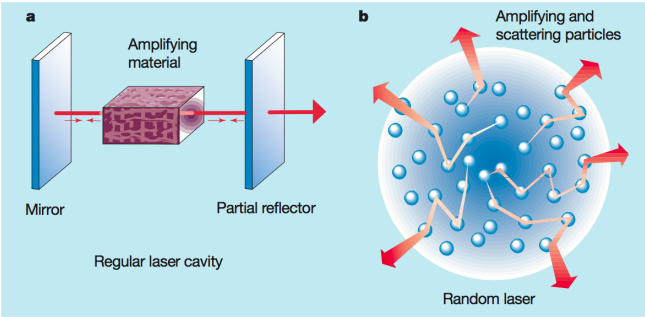

Figure 2.1 – Comparison between a conventional laser (a) and a random laser (RL) (b). In a regular laser the light is captured in the optical cavity and passes through the amplifying material several times. The gain amplification in this situation can be sufficiently large for the onset of lasing. Although the optical cavity is absent in the RL, the photon lifetime in the amplifying material due to the multiple scattering can be long enough that the amplification corresponding to the stimulated emission becomes efficient and the lasing begins in random directions [19].

Multiple scattering is a well-known phenomena, which occurs almost in all the opaque optical materials. The resemblance between a human tissue and a white paint is that the light propagating in both media undergoes multiple scattering. The propagation of light in such a system can be described as a random walk, like the process which happens to a photon inside

the core of sun before it escapes. This type of propagation can be modeled and studied by the diffusion equation. In 1968 Letokhov investigated the diffusion of light due to multiple scattering in the presence of gain and he found a critical situation where the amplification of light gets larger than losses and the so-called self-generation of photons occurs [1]. Letokhov's prediction was observed for the first time in 1994 by Lawandy et al. [20].

2.1 Random laser (RL)

2.1.1 Introduction

Although in the conventional lasers multiple scattering is usually considered as a detrimental effect, which removes lasing photons from the laser cavity mode, this effect combined with the gain can establish lasing. Multiple scattering increases the propagation length of a photon diffusing in that medium. This enhances the light amplification related to stimulated emission. Of course the mode properties are different from the lasers with cavity.

This type of lasing was first discussed theoretically by Letokhov. He showed that for light diffused in a medium in the presence of gain, the total amplification is scaled with the volume of the system whereas the losses are proportional to the total surface [1]. He predicted a threshold where the gain overcomes the losses and consequently the intensity of light increases with time and diverges. In the case of frequency dependent gain, the diffusion model also predicts narrowing in the spectrum of the emission above the threshold with a maximum at the same frequency as the maximum of the gain.

To describe the scattering process, two basic lengths are defined. The mean free path, ℓ_{sc}, which is the average distance that light travels between two consecutive scattering events, and the transport mean free path, ℓ_t, which is defined as the average distance that the incident light propagates in the medium before its direction gets randomized. These two length scales are linked by

$$\ell_t = \frac{\ell_{sc}}{1 - \langle \cos(\theta) \rangle}, \tag{2.1}$$

where θ is the scattering angle.

To characterize the light amplification due to stimulated emission, the gain length ℓ_g is defined as the path length over which the intensity of the light is amplified by a factor of e, and the amplification length ℓ_{amp} which is the rms average of distance from the beginning to the ending point for paths of length ℓ_g [2]. When the medium is transparent and homogeneous, light travels in a straight line and thus $\ell_{amp} = \ell_g$, whereas in a strongly scattering regime where a photon diffuses in the medium, $\ell_{amp} = \sqrt{Dt}$, where D is the diffusion coefficient and for a 3-dimensional system is $D = v\ell_t/3$, where v is

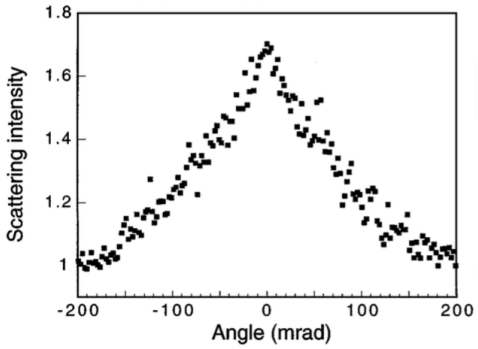

Figure 2.2 – Coherent backscattered light cone from ZnO powder film. Reprinted from [26].

the transport velocity of light. t also can be written as $t = \ell_g/v$, thus

$$\ell_{amp} = \sqrt{\frac{\ell_g \ell_t}{3}}. \tag{2.2}$$

Generally three regimes of light transport are considered in a 3D disordered medium

- The ballistic regime, $\ell_t \geq L$
- The diffusive regime, $L \gg \ell_t \gg \lambda$
- The localization regime, $k_e.\ell_{sc} \approx 1$

where L is the size of the medium and $k_e = k_0/n$ is the effective wave-vector and k_0 is the wavevector and n is refractive index [21]. Experimentally ℓ_t can be measured from the angular width of the backscattered cone of light in a coherent backscattering (CBS) experiment [22, 23, 24, 25]. In this experiment the angle of the backscattered light cone (Fig. 2.2) at the full-width at half-maximum (FWHM) is written

$$\Delta\theta \simeq \frac{0.7}{k_e \ell_t}. \tag{2.3}$$

2.1.2 Letokhov photonic bomb

In the diffusive regime, the diffusion of photons in a medium with a uniform and linear gain is described by

$$\frac{\partial W(\vec{r},t)}{\partial t} = D\nabla^2 W(\vec{r},t) + \frac{v}{\ell_g} W(\vec{r},t), \tag{2.4}$$

where $W(\vec{r},t)$ is photon energy density, D is the diffusion coefficient of the photon. A general solution to Eq. 2.4 is

$$W(\vec{r},t) = \sum_n a_n \psi_n(\vec{r}) e^{-(DB_n^2 - \frac{v}{\ell_g})t}, \tag{2.5}$$

where a_n are arbitrary constants and depend on the initial and boundary conditions, B_n and $\psi_n(\vec{r})$ are respectively eigenvalues and eigenfunctions of the equation

$$\nabla^2 \psi_n(\vec{r}) + B_n^2 \psi_n(\vec{r}) = 0, \tag{2.6}$$

which is obtained by substituting Eq. 2.5 into Eq. 2.4 and using modal decomposition. The boundary condition in such a system is defined as $\psi_n(\vec{r})|_{\vec{r}=z_e} = 0$ at distance z_e, which is known as the extrapolation length and quite often is much smaller than the physical dimension of the random medium and hence it can be approximated as $\psi_n = 0$ at the boundary of the medium.

Eq. 2.5 shows a change from an exponential decay to an exponential increase in time when the system crosses the threshold

$$DB_1^2 - \frac{v}{\ell_g} = 0, \tag{2.7}$$

where B_1 is the lowest eigenvalue. The values of B_n depend on the geometry of the medium, for example in a spherical shape with diameter L, $B_n = 2\pi n/L$, and for a cube shape with side length L, $B_1 = \sqrt{3}\pi/L$ [2]. Regardless of the shape of the scattering medium, order of magnitude for B_1 is $1/L$. For a spherical shape, Eq. 2.7 results to a critical size for the system

$$L_{cr} = 2\pi\sqrt{\frac{\ell_t \ell_g}{3}}. \tag{2.8}$$

If the gain length ℓ_g and the transport length ℓ_t are kept fixed, for a size of the medium above a critical value, $W(\vec{r},t)$ starts growing exponentially with time. Because of the similarity between this self-generation of the photons and the neutron multiplication in a nuclear bomb, this process is sometimes referred as a photonic bomb.

Although this model predicts a divergence for the light intensity, because of the gain depletion no explosion occurs. The gain begins to deplete quickly and consequently ℓ_g increases. By considering the gain saturation, Letokhov predicted a damped oscillation (pulsation) in the transient process of the generation. He also calculated the emission linewidth. The main limiting factor for the width of the lasing spectrum in the stationary regime comes from the spontaneous emission. Otherwise the Doppler effect from moving scatterer particles also induces some noise in the photon frequency [1].

Fig. 2.3 demonstrated the spectral features of RL emission from semiconductor powder while the pump intensity increased.

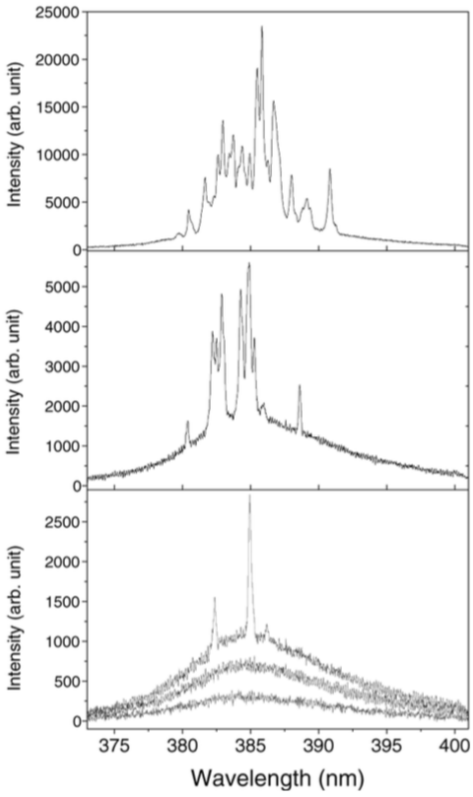

Figure 2.3 – Spectra of emission from ZnO semiconductor powder observed by Cao et al., while the pump intensity increased from below to above RL threshold (from bottom to top pump energy is 400, 562, 763, 875, 1387 kW/cm^2). During this experiment the excitation area was kept the same [26].

2.1.3 Coherent and incoherent feedback

Classifying random laser (RL) into coherent and incoherent feedback lasing categories, has been debated in the past two decades. It was initially believed that as the density of scatterers increases, the probability that the light comes back in closed loops during its propagation increases. That means the interference of light in this situation has to be taken into account. When the gain in such a loop exceeds the loss, laser oscillation can occur. The required constructive interference due to the total phase shift along the loop determines the frequency of oscillation. This is known as RL with coherent feedback [26, 27, 28].

The incoherent feedback can be interpreted in terms of modes. Instead of individual high-Q resonances there appear a large number of low-Q resonances which spectrally overlap and form a continuous spectrum. This corresponds to the occurrence of incoherent feedback. The absence of coherent feedback means that the cavity spectrum tends to be continuous, i.e., it does not contain discrete components at selected resonant frequencies [2]. By increasing the density of scatterers Cao et al. [29] observed the transition from incoherent to coherent feedback random laser (Fig. 2.4).

One main difference between the two types of feedback is that, in the incoherent one the interference effect is negligible, the photon is diffused and makes random walk in the disordered medium and mathematically the intensity can be analyzed by a diffusion equation to explain the lasing. Indeed this is at the heart of Letokhov's model. Whereas in the coherent feedback lasing, the interference effect cannot be neglected and is essential, so the electric field has to be studied instead of the intensity. The picture of closed loops is intuitive but naive. In general light can go back to its origin in many different paths, and all the backscattered light interferes and determines the lasing. Thus the coherent feedback RL is a randomly distributed feedback laser.

In order to develop a model which describes the coherent RL emission, instead of the diffusion equation for the light intensity, the Maxwell equations for the electro-magnetic fields should be used [30]. Several theoretical models have been already introduced, such as time-dependent theory [31], the collective modes of resonant scatterers [32], the prelocalized modes in diffusive media [33], the Anderson model [34], etc.

2.1.4 Coherence properties of random lasers

Temporal coherence and photon statistics

One important feature of the laser emission is its temporal coherence. Theoretical studies predicted that the random laser above threshold could be a coherent light [35] and its photon statistics could be very similar to those of a conventional laser.

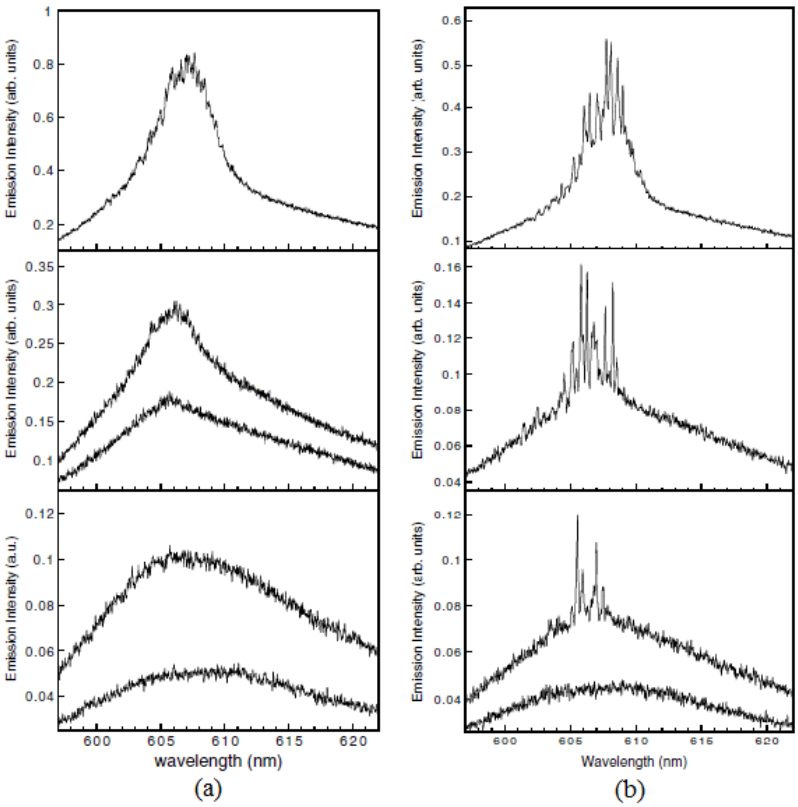

Figure 2.4 – Spectra of emission from the rhodamine 640 dye solution containing ZnO nanoparticles corresponding to (a) incoherent and (b) coherent feedback random laser. The ZnO particle density is $\sim 3 \times 10^{11}\,\mathrm{cm}^{-3}$ and $\sim 1 \times 10^{12}\,\mathrm{cm}^{-3}$ respectively. The incident pump pulse energy is (from bottom to top) 0.68, 1.5, 2.3, 3.3, 5.6 μJ in (a) and 0.68, 1.1, 1.3 and 2.9 μJ in (b) [29].

In quantum optics, correlation functions are used to characterize the statistical and coherence properties of light [36]. First order correlation function represents the fluctuations in the electric field

$$g^{(1)}(\tau) = \frac{\langle E^*(t)E(t+\tau)\rangle}{\langle |E(t)|^2\rangle}, \tag{2.9}$$

where $0 <= \left|g^{(1)}(\tau)\right| <= 1$, and $\left|g^{(1)}(\tau)\right| = 0, 1$ represents incoherent and coherent electric field respectfully. On the other hand, the degree of second-order coherence characterizes the intensity fluctuations

$$g^{(2)}(\tau) = \frac{\langle I(t)I(t+\tau)\rangle}{\langle I(t)\rangle^2}, \tag{2.10}$$

where $0 <= g^{(2)}(0) <= 1$. A light source is called coherent when $g^{(1)}(\tau) = g^{(2)}(\tau) = 1$. This is of course ideal and in practice a coherence time τ_c, which depends on the modes and spectral distribution of light, has to be taken into account. A source with a sufficiently narrow wavelength band, for example, has automatically high first-order coherence [37]. Thus a band-pass filter which selects a narrow wavelength band can increase first-order coherence of a light emission. Obtaining second-order coherence though is more challenging, since photons have a natural tendency to bunch, and this leads to large intensity fluctuations. Gain saturation is a nonlinear effect in lasers which restricts the intensity fluctuations and consequently reduces the second-order correlation. In a conventional laser, it is the cavity that creates feedback and makes an automatic mechanism which results in the gain saturation and thereby in second-order coherence. In a random laser however, the gain saturation can be achieved by, for instance, the amplified spontaneous emission (ASE) through stimulated emission [38]. For large gain, intensity grows till the gain medium is depleted entirely. Therefore the intensity fluctuations will be suppressed and thereby leads to second-order coherence. This is regardless of the number of scattering events in the medium.

It is known that the photon statistics of a single-mode coherent light obeys a Poisson distribution

$$P_{\mathrm{P}}(n) = \frac{\langle n\rangle^n e^{-\langle n\rangle}}{n!}, \tag{2.11}$$

where $\langle n\rangle$ is the average photon number and is written as

$$\langle n\rangle = \sum nP(n) \tag{2.12}$$

$$\tag{2.13}$$

while the photon statistics of a single-mode chaotic light satisfies Bose-Einstein (B-E) distribution [39]

$$P_{\mathrm{BE}}(n) = \frac{\langle n\rangle^n}{(1+\langle n\rangle)^{1+n}}. \tag{2.14}$$

For a multi-mode chaotic light the photon statistics converges to the Poisson distribution. Once the $P(n)$ is measured, one can calculate the normalized second-order correlation coefficient

$$G_2 = g^{(2)}(\tau = 0) = 1 + \frac{\langle (\Delta n)^2 \rangle - \langle n \rangle}{\langle n \rangle^2}, \tag{2.15}$$

where $(\Delta n)^2 = \langle n^2 \rangle - \langle n \rangle^2$. For the B-E distribution $G_2 = 2$, and for the Poissonian distribution $G_2 = 1$.

Alternatively, the shot noise power can be used as a reference. The one-sided power spectral density of the shot noise is given by

$$S_{SN} = 2h\nu\overline{P_{op}}, \tag{2.16}$$

where $\overline{P_{op}}$ is the mean optical power. Comparing the intensity noise of a light with the shot noise thus can be used to indicate whether it is coherent or not. In particular to determine if a light is incoherent (above shot noise level) or coherent (noise equal to shot noise) or squeezed (below shot noise). This is the essence of the Fano factor [40]. The properties of the above parameters are summarized in table 2.1.

Table 2.1 – Comparing the values of $|g^1(\tau)|$, $g^2(\tau)$ and photon statistics P(n) of different types of light. "P" and "B-E" stand for Poisson and Bose-Einstein distribution respectively.

Types of light	Photon statistics $P(n)$
Ideal coherent light	P
Ideal incoherent light	B-E
Single-mode laser	P
chaotic light	B-E
ASE	B-E

Based on the parameters introduced here, one can study the coherence properties of any light source. Cao and coworkers studied the photon statistics of the random laser and they observed that it is similar to that of a conventional laser [13]. They used a compressed pellet of ZnO powder as the scattering and the gain medium, and a Nd:YAG pulsed laser to optically pump the sample. Then the emitted light was collected and observed by a spectrometer-streak camera setup which operated in the photon counting mode. With this detection setup they were able to study the time evolution of the emitted light at different wavelengths (Fig. 2.5). In order to investigate the photon number distribution of a single lasing mode, only photons from an individual intensity spike (a single dark region in Fig. 2.5) are counted within a square with wavelength resolution of $\Delta\lambda$ and sampling time Δt. Hence the sampled radiation field is within frequency interval of

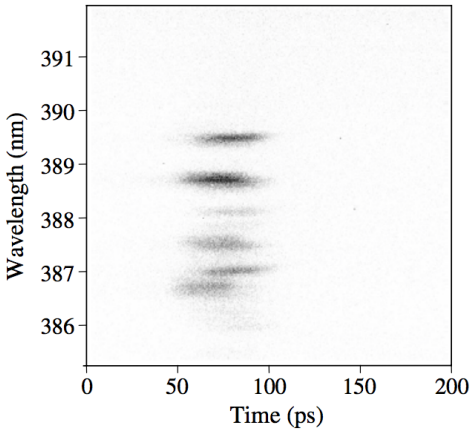

Figure 2.5 – The spectral-temporal image of the lasing from ZnO powder taken by spectrometer-streak camera. The incident pump pulse energy is 4.5 nJ. Reprinted from [13].

$\Delta\nu = c\Delta\lambda/\lambda^2$. Thus by setting the sampling time respecting $\Delta\nu\Delta t < 1$, the counting area corresponds to a single electromagnetic mode. After counting the number of photons for a large number of pulses $P(n)$ was obtained.

Then the evolution of the photon number distribution for different pumping intensities was investigated (Fig. 2.6). They observed that well above the random lasing threshold the photon statistics changes from B-E distribution to Poisson (Fig. 2.7). Next, in order to confirm the reliability of their measurements, the photon statistics of a single-mode quasi thermal light was measured and it was in agreement with the B-E distribution.

Using a similar method Zacharakis et al. studied the photon number distribution of the fluorescence from a polymer sheet of dye material (Fig. 2.8) [12]. The observed data was well fitted by a linear combination of Poisson and B-E distribution

$$P(n) = \alpha \frac{\langle n\rangle^n e^{-\langle n\rangle}}{n!} + (1-\alpha)\frac{\langle n\rangle^n}{(1+\langle n\rangle)^{1+n}}, \tag{2.17}$$

where α is defined as the coherent percentage and indicates the proportion of the Poisson contribution (as coherent part) to the B-E portion (as the incoherent part) [12].

However their observation disagreed the Cao's results, and did not confirm the coherence of random laser. Zacharakis's results and conclusion was criticized later in some other papers. For instance, Cao et. al suggested that because of incoherent feedback lasing mechanism in their dye material, the photon number distribution associated to the ASE, which has B-E photon

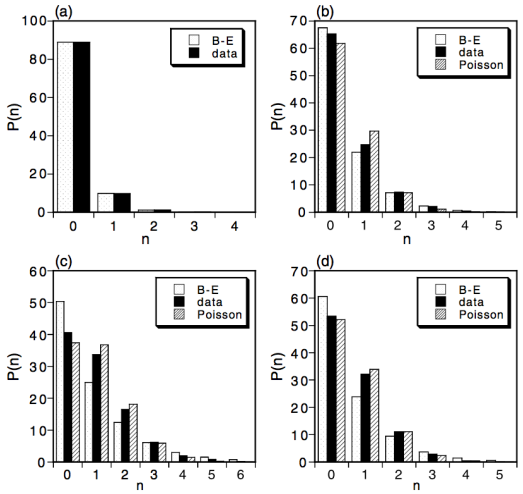

Figure 2.6 – The measured photon number distribution of random lasing from a ZnO pellet (Solid columns) and comparing to the B-E (dotted) and Poisson distribution (dashed) for the same count rate. The ratio between the incident pump intensity and threshold intensity is (a) 1.0, (b) 1.5, (c) 3.0, (d) 5.6. The saturation intensity is assumed as the amount of pump intensity at which the discrete spectral feature appears. Reprinted from [13].

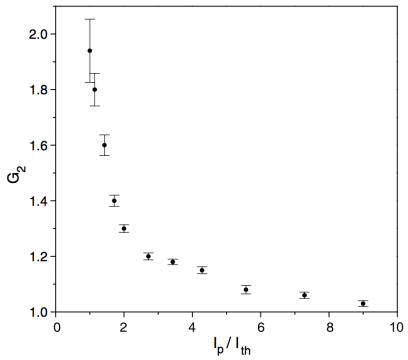

Figure 2.7 – The second-order correlation coefficient as a function of the ratio of the incident pump intensity I_p to the threshold intensity I_{th}. Reprinted from [13].

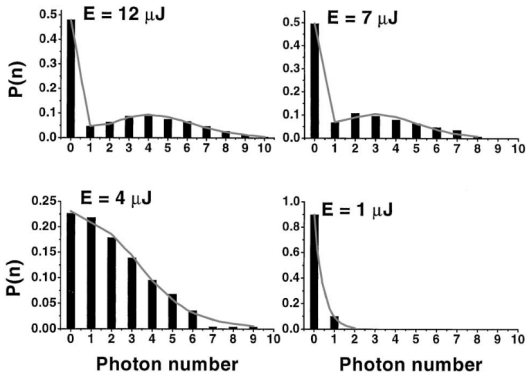

Figure 2.8 – The measured photon number distribution of a random laser emission from dye material for different excitation energy. The data was fitted (lines) by a linear combination of Poisson and B-E function. Reprinted from [12]. The coherence percentage $\alpha = 0$, 0.37, 0.49, 0.50 for the excitation energy of E= 1, 4, 7, 12 μJ respectively.

statistics [41], could be significant [13].

Based on a chaotic cavity filled with a laser dye material, Patra theoretically modeled the photon statistics and the Fano parameter of the RL [14]. He showed that in general random lasing radiation fluctuates more compared to the conventional lasers. The amount of fluctuations and photon statistics depend critically on the number of modes which contribute to the detection. Moreover this excess noise could be connected to the mode-competition i.e. indeterminacy in the number of emitted modes in the detected light. This kind of noise is due to the overlap between the possible emitting modes. If only one mode is above threshold, the emission becomes coherent, whereas the strength of the coherence decreases by adding number of modes above threshold. Thus according to the above argument, Patra suggested that the reason for difference between two observations in Refs. [13] and [12] is due to the different number of detected modes in their experiments.

By improving the detection setup to select the non-overlapping modes, photon statistics of RL radiation from a dye doped hybrid powder was studied [42]. The experiment is very similar to what has been reported in [12]. By applying spatial filtering technique, they discriminated modes with high resolution with respect to the spatial coherence size of its laser like emission. This process of limiting the detected modes was done by locating an aperture with a size close to the transport length in the material under study. They also measured the photon statistics of the RL, and they observed that above threshold, the correlation coefficient, G_2, and the coherent percentage α, approaches one at the time of maximum pump intensity and around the

wavelength of the maximum gain response.

Florescu et. al. [35] developed a theoretical model to describe photon statistics of a random laser. It was shown that the laser threshold is lowered by an increase in the strength of scattering. This leads to redistribution of the noise with respect to the Poissonian value. From this point of view the lasing with association to the larger number of scattering events shows higher level of coherence.

As mentioned above, several techniques have been used to study the temporal response of the light such as first and second-order temporal correlation functions and photon probability distribution. However sometimes the third order intensity correlation can provide some extra information. For instance, the second-order intensity correlation gives information only about the Fourier magnitude of the temporal response, while the third-order intensity correlation provides information about the Fourier phase also. Cao et al. showed theoretically and experimentally that in a passive random medium, by measuring the third-order speckle intensity correlation, it is possible to reconstruct the temporal response of that medium [43]. Propagation of a coherent light through a disordered scattering material makes interference between multiply scattered partial waves and therefore it produces fluctuations in the intensity. This phenomena is known as speckle, and its statistical properties have been well studied and explained in some optics and laser physics contexts [44, 45]. However, it is not yet clear if this technique helps to get more information about RL as well.

Spatial coherence

In general, spatial coherence properties of a RL are complicated and quite different from the conventional lasers. Initially it was stated that the RL emission has lower spatial coherence than the conventional one [46, 47, 48, 49]. This difference leads to some potential applications for RL, such as the experiments and measurements that need low spatial coherent light or implementation of speckle free experiments. For instance in the laser ranging [50] and optical coherent tomography [51] the main limit comes from the spatial cross-talk and speckle, thus in these experiments applying an intense but spatially incoherent light can be beneficial.

Recently the spatial coherence measurements of RL have been demonstrated in several works. For example Redding et al. [52] implemented a double slit experiment (Fig. 2.9a) to study the spatial coherence of RL emission. More specifically, in this experiment they studied the effect of some parameters like the scatterer concentration, i.e the strength of the scattering by changing ℓ_{sc}, the excitation volume, and the pump energy.

For quantitative study of the spatial coherence, the mutual coherence

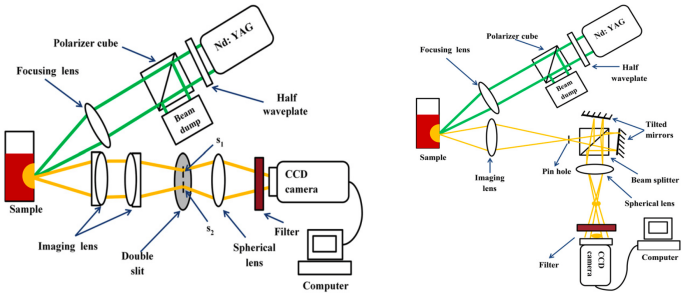

(a) (b)

Figure 2.9 – Schematic of the experimental setup for (a) spatial coherence measurement, (b) Michelson interferometry for temporal coherence measurement. Reprinted from [53].

function, $\gamma_{1,2}$, which is a complex function is defined as

$$\gamma_{1,2} = \frac{\langle E_1 E_2^* \rangle}{\sqrt{I_1 I_2}}, \tag{2.18}$$

where $I_{1,2} = |E_{1,2}|^2$ denotes the intensity due to each slit. The superposition of the intensities at the screen or the detector can be written

$$I = I_1 + I_2 + 2\sqrt{I_1 I_2}|\gamma_{1,2}|\cos(\phi), \tag{2.19}$$

where ϕ is the phase of $\gamma_{1,2}$. When $|\gamma_{1,2}|$ is zero the light is defined as spatially incoherent, and $|\gamma_{1,2}| = 1$ means coherent light. The case where $0 < |\gamma_{1,2}| < 1$ is referred to as the partially coherent light. When the intensities at each slit are equal, which is the case in this experiment, $\gamma_{1,2}$ reduces to the visibility or contrast

$$|\gamma_{1,2}| = V \equiv \frac{I_{max} - I_{min}}{I_{max} + I_{min}}, \tag{2.20}$$

where I_{max} and I_{min} are the maximum and minimum intensities of the interference fringes.

Based on this parameter, it was shown that the spatial coherence of the RL emission is enhanced by decreasing ℓ_{sc} (or in other words when the sample is denser and the scattering gets stronger). In contrast enlarging the pump area in the sample at fixed pump power leads to a reduction in coherence of the RL [52, 53].

This technique in addition to Michelson-like interferometer (Fig. 2.9b) was used to study both spatial and temporal coherence of the RL [54] and to investigate the RL threshold by studying the visibility as a function of pumping energy [53]. It was observed that when the excitation intensity goes

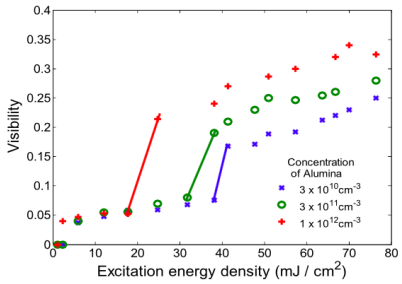

Figure 2.10 – Visibility (spatial coherence) of the emission as a function of excitation energy for three different sample concentrations measured by a setup depicted in Fig. 2.9a. An abrupt increase in the visibility shows the onset of random lasing action and represents the threshold, which is in agreement with the theoretical predictions. Reprinted from [53].

above threshold, an abrupt increase in the visibility (i.e. spatial coherence) occurs (Fig. 2.10). However comparing the spatial coherence of a RL with a conventional laser shows less coherence for the RL.

To summarize, the photon statistics and coherence properties of a random lasing emission is still a controversial topic. To extensively understand and characterize those properties, further theoretical and experimental investigation is needed. Based on the previous works, generally the spatial coherence of a RL is expected to be lower than a conventional laser. Moreover, It is enhanced by increasing the scattering strength in a medium. On the other hand the spatial coherence, e.g. visibility, shows an instantaneous increase when the pumping energy passes the threshold.

Furthermore, the second-order temporal correlation of a single mode random laser emission well above threshold shows a coherent light. This is also what is expected from standard lasers. However the observation of $G_2 = 1$ is challenging since only a single mode of random lasing emission must be selected and discriminated from the other sources of fluorescence, i.e. ASE which is incoherent. Experimentally, as the ratio of random lasing to ASE grows, due to i.e. higher pump intensity well above threshold, G_2 is expected to approach one.

Finally the photon statistics $P(n)$ of a light in general can be modeled as a partial coherent light with a combination of a Poisson distribution (corresponding to the coherent part) and a B-E distribution (corresponding to an incoherent part, i.e. chaotic light or ASE). For a RL below threshold $P(n)$ is expected to demonstrate a pure B-E distribution, whereas above the threshold, the coherent percentage α increases substantially and $P(n)$ converges to a Poisson distribution.

In this section, the random laser was defined with a focus on its coherence properties. Generally random laser can be considered as a partially coherent light and the coherence percentage is enhanced by increasing either the gain or the scattering. We showed that coherence measurements can be employed to testify a random laser emission and to investigate threshold.

2.2 Cold-atom RL

2.2.1 Advantages and disadvantages of cold atoms

A cloud of cold atoms has very different properties from the other standard sources of RL such as semiconductor powders or dye solutions. In this section we try to compare some of the advantageous and disadvantageous properties of the cold atoms with those of the other sources of RL.

First of all, cold atoms are simple and well-controlled systems. That makes it easier to develop a theoretical model. Moreover it is considered as a homogeneous system (with no impurities) and because of the very low temperature ($\sim 100\,\mu$K) the Doppler effect can be neglected. Moreover, some fundamental features of cold atoms are tunable. For example there are some techniques which allow us to manipulate the density n, mean free path ℓ_{sc}, and scattering cross-section σ.

Secondly, cold atoms do not present non-radiative fast-decaying transitions, preventing a standard four-level scheme to produce a population inversion [55]. Nevertheless there are some known mechanisms to make population inversion between different atomic states. This means that the dephasing time of the optical coherence is often in the same order of magnitude as the life time of the excited states. In contrast, in solid state samples for instance, non-radiative process (like electron-photon interactions) reduces the optical coherence time to some orders of magnitude below the population relaxation time.

Finally, using a pump-probe configuration in the cold-atom experiment makes it possible to investigate different gain mechanisms. However, contrary to most RL sources, in cold atoms amplifiers and scatterers are the same and the gain and multiple scattering are linked and controlled together. Nevertheless the frequency at which gain and scattering occur, are often different. Thus it is necessary to find an appropriate mechanism to provide both simultaneously.

Although there is no absorption in the cold atoms, the scattering from the atoms, depending on the experimental situation, could be inelastic, which is considered as a drawback for RL. Furthermore disorder configuration, i.e. the position of the atoms in a magneto-optical trap (MOT), changes for each RL realization, which makes it easy to integrate data but this averaging in each realization would be unavoidable.

2.2.2 Gain and lasing with cold atoms

As discussed in the previous sections, to generate random lasing one needs two fundamental ingredients, multiple scattering and gain. In our lab we can prepare MOT with on-resonance optical thickness of $\sim 10 - 100$ which is large enough to induce multiple scattering and radiation trapping [56]. In this section we explain how the second necessary ingredient of RL can be achieved from cold atoms. Although there are several possible gain mechanisms in cold atoms, we only employ Raman gain among them, which is experimentally easier to combine with multiple scattering.

Raman gain using Zeeman sublevels

Raman transition generally means a two-photon transition between two non-degenerate ground levels which could be either Zeeman sublevels or hyperfine states. To characterize this gain a pump-probe configuration is needed. Using a pumping field to make an upward transition to the vicinity of an atomic excited state, then a probe beam can be amplified at the frequency of the downward transition.

A first possibility is to make population inversion between the different light-shifted Zeeman sublevels m_F of a given hyperfine state F by a pump beam (Fig. 2.11a) [57, 58]. For instance, optical pumping by a π-polarized laser near a closed transition of $F = 1 \rightarrow F' = 2$, results in a symmetric population distribution. Since the $m_F = 0$ sublevel of the ground state has the largest Clebsch-Gordan coefficient C, it is the most populated and most shifted state [59] according to the light shift for a red-detuned light

$$\Delta E \sim -\frac{C^2\Omega^2}{2\Delta}, \tag{2.21}$$

where $\Omega = \Gamma I/2I_{\text{sat}}$ is the Rabi frequency, and Δ is the detuning of the pump from the excited state. To characterize this process one needs to observe the transmission spectrum by probing the atoms with a linearly polarized weak laser beam. With the polarization axis orthogonal to the pump polarization, it induces $\Delta m_F = \pm 1$ Raman transitions. For a given pump-probe detuning δ population imbalance in the Zeeman sublevels and that introduces either gain or absorption depending on the sign of the detuning. For a larger F, each pair of neighboring sublevels contributes with a relative weight depending on the population inversion. In practice however, only two components are observable; one due to the amplification at $\delta = -\delta_R$ and the other due to the absorption at $\delta = \delta_R$ when the pump beam is red detuned ($\Delta < 0$). For a blue detuned pump beam ($\Delta > 0$), that structure will be inverted. This mechanism has been also applied to produce lasing with a cold-atom cloud inside an optical cavity [60, 61]. The narrow spectrum of this kind of laser can be easily characterized by a beat-note measurement [60]. Note that

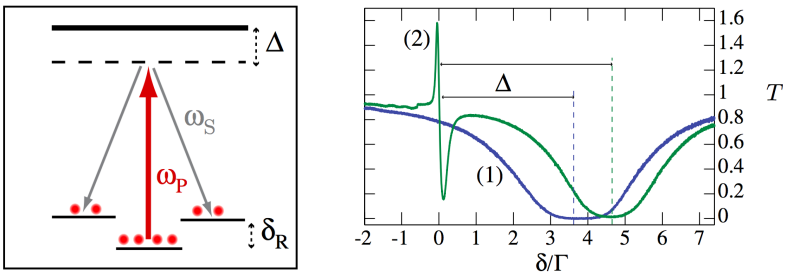

(a) (b)

Figure 2.11 – (a) Principle of the Raman mechanism due to a $F = 1 \rightarrow F' = 2$ transition. (b) Experimental transmission spectra recorded with cold ^{85}Rb near the $F = 3 \rightarrow F' = 4$ transition plotted as a function of pump-probe detuning δ. Without pumping, spectrum (1) shows only the atomic absorption. A pump beam of detuning $\Delta = 3.8\,\Gamma$ and intensity $13\,\mathrm{mW/cm^2}$, corresponding to a Rabi frequency $\Omega = 2.5\,\Gamma$, is added to obtain spectrum (2), which then exhibits a Raman resonance in the vicinity of $\delta = 0$. Moreover, the atomic absorption is shifted due to the pump-induced light shift and the absorption is reduced due to saturation. Adapted from Ref. [62].

δ_R is related to the light shift and thus it depends on the Clebsch-Gordan coefficients of each sublevels, and usually its value is small ($\delta_R \sim \Gamma$). On the other hand Δ is a few Γ. The width of the Raman resonances γ is connected to the elastic scattering, which is also smaller than Γ [58]. This leads to spectrally narrow resonances far from the main atomic absorption resonance (Fig. 2.11b). Thus this Raman gain is very sensitive to any Doppler shift. For instance the radiation pressure from the intense pump beam, induces strong enough Doppler shift which changes and destroys the Raman gain structure and would stop the laser emission after a very short time.

Raman gain using hyperfine sublevels

Two-photon transition between two hyperfine ground states can also leads to a Raman gain (Fig. 2.12). The advantage of this kind of gain is that the frequency of the pump beam is relatively far from the gain photons, for instance in the case of rubidium atoms the two hyperfine ground states $F = 2$ and $F = 3$ are separated by a few gigahertz. However since the pump laser is tuned close to an open transition in this configuration, it destroys the population inversion quickly and hence another laser is needed to recycle the ground states population distribution, and it increases somehow the complexity of the experimental setup.

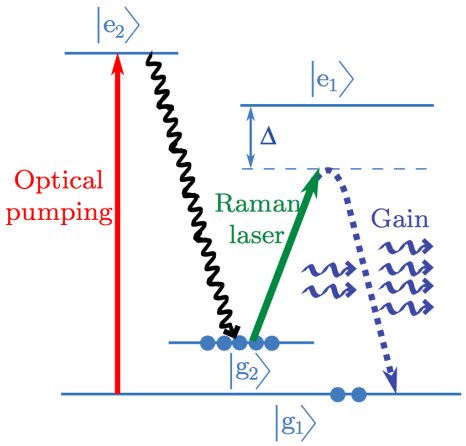

Figure 2.12 – An example of Raman gain using hyperfine states. Here the Raman laser makes two-photon transition and generates gain by inducing stimulated emission. The optical pumping laser recycles the atoms and maintains the population inversion between the hyperfine ground states $|g_1\rangle$ and $|g_2\rangle$. Reprinted from Ref. [4]

This gain mechanism has been used in different experiments on lasing with cold atoms in different regimes [63, 64, 65] as well as the cold-atom random laser experiment [4].

Other gain mechanisms

There are some other known mechanisms to generate gain such as Mollow [66] and non-degenerate four-wave mixing (NDFWM) [67] gains. These gain mechanisms have been already explained with details in Ref. [60, 68, 69, 70]. However producing RL from hyperfine Raman gain is much easier than the others because of the expected lower threshold condition.

2.2.3 Threshold of a cold-atom RL

Letokhov's threshold of a RL

As mentioned in Sec. 1.1.2, considering the Letokhov's approach to derive the threshold condition for continuous-wave (cw) operation of random lasing, by solving the diffusion equation (Eq. 2.4), a critical sphere diameter was found

$$L_{\text{eff}} > 2\pi\sqrt{\frac{\ell_{sc}\ell_g}{3}}, \tag{2.22}$$

which showed a threshold for an exponential increase in the energy density in time. Here $L_{\text{eff}} = \eta L$, where $\eta \sim 1$ is a small correction factor in the diffusive regime. For a sphere geometry

$$\eta = 1 + \frac{2\xi}{\frac{L}{\ell_{sc}} + 2\xi}, \tag{2.23}$$

where $\xi \simeq 0.71$ [71, 72]. Note that this threshold value is correct under the validity of the diffusive or multiple scattering regime, where $L \gg \ell_{sc}$. We call this condition Letokhov's threshold [55].

Threshold of a RL using the radiative transfer equation

When a medium is weakly scattering, transport of the light can be modeled by the radiative transfer equation (RTE) [73], which is valid from the ballistic regime to the diffusive one [74]. For a plane wave along z-axis propagating in the direction of $\mathbf{u}$ and for isotropic scatterers in the presence of the gain, RTE is written as

$$\frac{1}{v}\frac{\partial}{\partial t} I_\omega(z,\mu,t) + \mu \frac{\partial}{\partial z} I_\omega(z,\mu,t) = (g-\chi) I_\omega(z,\mu,t) + \frac{\chi}{2}\int_{-1}^{+1} I_\omega(z,\mu',t) d\mu', \tag{2.24}$$

where $I_\omega(z,\mu,t)$ is the specific intensity which characterizes the number of photons at frequency ω and it depends on the spatial variable z and the angular variable $\mu = cos\theta$, with θ the angle between the propagation direction $\mathbf{u}$ and the z-axis. Here v is the transport velocity of light in the medium, g is the linear gain coefficient and $\chi = 1/\ell_{sc}$. For a medium with linear gain, $g = 1/\ell_g > 0$.

In the slab geometry, it is possible to solve the RTE by a modal expansion of the equation. This expansion has asymptotic behavior at large length and time scales which converges to the modal expansion of the diffusion equation [71]. Although there is no modal expansion of RTE in 3D available, it can be directly solved [75, 76, 10] by applying the so-called Eddington approximation [77, 78]. As a result one can find a critical radius R_{cr} given by

$$\tan(qR_{cr}) = \frac{2gqR_{cr}}{2g - q^2 R_{cr}}, \tag{2.25}$$

where

$$q^2 = 3g(\chi - g) = \frac{3}{\ell_g}\left(\frac{1}{\ell_{sc}} - \frac{1}{\ell_g}\right). \tag{2.26}$$

In the diffusive regime ($\chi R_{cr} \gg 1$) and when the scattering is much more than the gain ($\chi \gg g$ so $q^2 \simeq 3\chi g$), Guerin et al. show [79] that the critical radius of a spherical medium matches with the one obtained by the diffusion equation (Eq. 2.22).

Threshold of cold-atom RL

For a cloud of cold atoms, all the characteristic lengths can be written as a function of the atomic polarizability $\alpha(\omega)$. Experimentally α is determined by the pumping parameters, detuning Δ and intensity. For example the elastic scattering cross-section is given by

$$\sigma_{sc}(\omega) = \frac{k^4}{6\pi} \times |\alpha(\omega)|^2, \tag{2.27}$$

and the extinction cross-section by

$$\sigma_{ex}(\omega) = k \times \mathbb{I}\mathrm{m}\left[\alpha(\omega)\right], \tag{2.28}$$

where $k = \omega/c$ is the wave vector [80]. Note that Eq. 2.27 is specific to the dipole scatterers, while Eq. 2.28 is generally valid for any dielectric medium. Moreover, the characteristic lengths are linked by

$$\begin{aligned} \frac{1}{\ell_{ex}} &= \frac{1}{\ell_{sc}} - \frac{1}{\ell_g} \\ \frac{1}{\ell_{ex,sc,g}} &= n\sigma_{ex,sc,g}, \end{aligned} \tag{2.29}$$

where σ_g is gain cross-section and n is the atomic density.

We can consider only resonant scatterers and thus quasi-resonant light $k = k_0 = \omega_0/c$ with ω_0 the atomic eigenfrequency. In the following a dimensionless atomic polarizability $\tilde{\alpha}$ is introduced and defined by $\alpha = \tilde{\alpha} \times \sigma_0/k_0$, which omits the dependence on ω. Here $\sigma_0 = 3\lambda^2/2\pi = 6\pi/k_0^2$ is the resonant scattering cross-section. Therefore Eq. 2.27-2.29 can be rewritten as

$$\begin{aligned} \sigma_{sc} &= \sigma_0 |\tilde{\alpha}|^2 \\ \sigma_{ex} &= \sigma_0\, \mathbb{I}\mathrm{m}[\tilde{\alpha}] \\ \sigma_g &= \sigma_0\big(|\tilde{\alpha}|^2 - \mathbb{I}\mathrm{m}[\tilde{\alpha}]\big). \end{aligned} \tag{2.30}$$

Next by using Eqs. 2.29 and 2.30 in the Letokhov's threshold given by Eq. 2.22, this results to [81]

$$n\sigma_0 L_{\text{eff}} = \eta b_{0cr} > \frac{2\pi}{\sqrt{3|\tilde{\alpha}|^2\big[|\tilde{\alpha}|^2 - \mathbb{I}\mathrm{m}(\tilde{\alpha})\big]}}, \tag{2.31}$$

where $b_0 = n\sigma_0 L$ is the on-resonance optical thickness of the atomic cloud. This threshold condition is valid in the diffusive regime, i.e. $|\tilde{\alpha}|^2 - \mathbb{I}\mathrm{m}(\tilde{\alpha}) > 0$.

Thus for a cloud of cold atoms the threshold can be expressed in terms of the on-resonance optical thickness b_0 which is an intrinsic parameter, and it is a function of complex variable of polarizability. Note that the real and

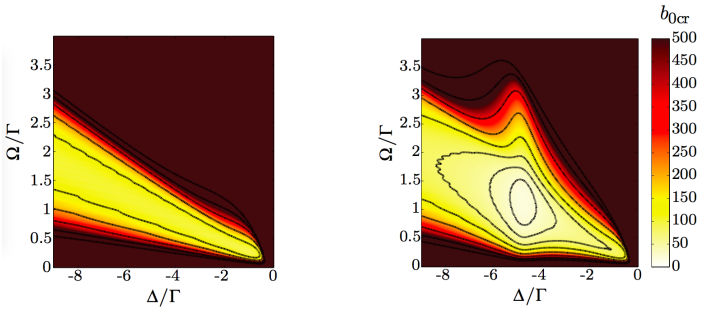

Figure 2.13 – Threshold for a RL using Raman gain between hyperfine levels, as a function of the Raman laser parameters (detuning Δ and Rabi frequency Ω). The optical pumping parameters are $\Delta_{OP} = 0$ and $\Omega_{OP} = 0.2\,\Gamma$. (a) Scheme taking four levels into account. The lowest threshold is $b_{0cr} = 92$. (b) Scheme with five levels involving supplementary scattering from the $|2\rangle \rightarrow |1'\rangle$ transition (Fig. 2.14). The lowest threshold is $b_{0cr} = 20$. Adapted from Ref. [55].

imaginary parts of α (or in other words ℓ_{sc} and ℓ_g) are related via Kramers-Kronig relation [82]

$$\begin{aligned} \mathbb{R}\mathrm{e}[\alpha(\omega)] &= \frac{1}{\pi} P \int_{-\infty}^{\infty} \frac{\mathbb{I}\mathrm{m}[\alpha(\omega')]}{\omega' - \omega} d\omega' \\ \mathbb{I}\mathrm{m}[\alpha(\omega)] &= -\frac{1}{\pi} P \int_{-\infty}^{\infty} \frac{\mathbb{R}\mathrm{e}[\alpha(\omega')]}{\omega' - \omega} d\omega', \end{aligned} \tag{2.32}$$

where P is the Cauchy principal value. This simplifies the characterization of the threshold in the experiment, as only one measurement is enough to determine $\tilde{\alpha}$. Experimentally $\tilde{\alpha}$ is characterized by recording the transmission spectrum of a weak probe beam [83]

$$T(\omega) = \exp\big(-b_0\, \mathbb{I}\mathrm{m}[\tilde{\alpha}(\omega)]\big). \tag{2.33}$$

Using Eq. 2.31, the threshold in different gain mechanisms can be characterized and compared. For more details see Ref. [68, 81, 83]. For example by solving the optical-Bloch equations (OBE) for relevant gain parameters, the critical optical thickness can be numerically simulated as a function of pumping parameters (detuning and intensity) for Raman gain between hyperfine ground states, which resulted in a minimum $b_{0cr} \sim 100$ [68], which is a significant improvement compared with the other gain mechanisms (Fig. 2.13).

We can summarize the optimum threshold conditions for different gain mechanisms in table 2.2. Since the gain frequency is detuned by several

Table 2.2 – Comparing the lowest threshold in different gain mechanisms. Considering this table, the Raman gain between the hyperfine ground states with additional scattering is the most feasible mechanism for generating cold-atom RL. In our lab we are able to make a cold-atom cloud with the optical thickness of $b_0 \sim 10 - 200$.

Gain mechanism	**Evaluation method**	b_{0cr}	**Validity of the diffusion approximation**	Ref.
Mollow gain	Analytical calculation of α	~ 300	Not valid	[81]
NDFWM	Experimental and numerical	∞	Valid	[55]
Raman gain (Zeeman sublevels)	Experimental	~ 200	Not valid	[83]
Raman gain (hyperfine states)	Numerical	~ 90	Not valid	[55]
Raman gain (hyperfine states) with additional scattering	Numerical	~ 20	Valid	[4]

atomic linewidth Γ from the transition providing scattering, it is considered as a regime with low scattering and high gain. In other words the validity of the diffusion approximation breaks down and one needs to study the RTE instead for computing the threshold. However Froufe-Pérez and coworkers showed that for a slab it leads to very similar results [81].

Combining scattering to the Raman gain

As already explained, in order to prepare an appropriate condition for random lasing we have to find a scheme in which the Raman gain and scattering are present simultaneously. Fortunately the rich atomic structure of the D_2 line of rubidium atoms allows us to combine them, as it is depicted in Fig. 2.14 for ^{85}Rb atoms (see also Fig. 3.1). Five hyperfine states are involved in this scheme. There are two ground levels as $|F = 2\rangle \equiv |2\rangle$ and $|F = 3\rangle \equiv |3\rangle$, and three excited states ($|F' = 1\rangle \equiv |1'\rangle$, $|2'\rangle$ and $|3'\rangle$).

A transition between $|3\rangle \rightarrow |2'\rangle$ contributes to the generation of the Raman gain depending to the detuning of the Raman laser from $|2'\rangle$ Δ, while $|2\rangle \rightarrow |1'\rangle$ transition contributes to the scattering of the gain photons and $|2\rangle \rightarrow |3'\rangle$ transition provides the optical pumping to control the populations in the two ground states. It is clear that when Δ is chosen equal to the separation of $|1'\rangle$ and $|2'\rangle$ the scattering will be maximum.

There are some important features in this supplementary scattering

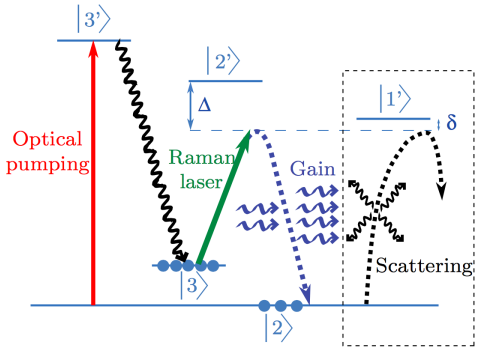

Figure 2.14 – Raman gain scheme used for random lasing in cold ^{85}Rb. Supplementary scattering is provided by the $|2\rangle \rightarrow |1'\rangle$ transition. Reprinted from Ref. [4]

scheme. Firstly $|2\rangle \rightarrow |1'\rangle$ photons do not couple to level $|3\rangle$ because of the selection rule ($\Delta F = 0, \pm 1$). So the level $|1'\rangle$ does not interact with the Raman laser and does not destroy the Raman gain. Secondly $|2\rangle \rightarrow |1'\rangle$ is a closed transition, which means that it does not interfere with the equilibrium populations in the ground states which is governed only by the composition of the optical pumping and the Raman laser. Finally the separation between $|1'\rangle$ and $|2'\rangle$ is only 29 MHz or 4.8 Γ, which is small enough to make efficient Raman gain. Note that another similar scheme to combine Raman gain and supplementary scattering is possible through $|4'\rangle$ state. However the nearest excited state in this case is separated by $\approx 20\,\Gamma$ and hence the Raman gain would be much less efficient. This is also the reason why ^{85}Rb are preferred to the ^{87}Rb atoms, in which the hyperfine excited states splitting is larger.

By solving the OBEs for the five contributing states, including a supplementary incoherent scattering term due to the $|2\rangle \rightarrow |1'\rangle$ transition, and considering the optimum parameters, a critical optical thickness $b_{0cr} \sim 20$ is obtained with $L/\ell_{sc} \sim 6$ which fulfills the diffusion approximation [4, 68]. However the Zeeman degeneracy is neglected in this model and therefore the result is not completely precise.

2.2.4 Observational results

The random lasing emission from cold ^{85}Rb atoms have been observed recently [4]. Observation of RL is a challenging issue and needs to settle down some difficulties. In this section we explain the detection system and the results which has been observed recently in our group. The Raman gain and scattering scheme is based on what is already represented in Fig. 2.14.

Experimentally a controlled compression period (see Sec. 3.4) is exerted

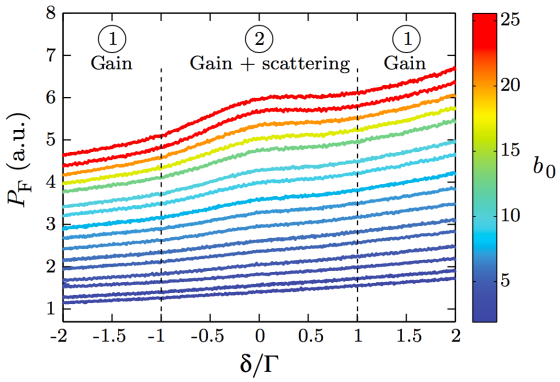

Figure 2.15 – Measurement of the total fluorescence emitted by the atomic cloud as a function of the Raman laser detuning for different on-resonance optical thickness b_0. Reprinted from Ref. [4]

on the atoms, then by time of flight technique (see Sec. 3.6.3) b_0 is varied with a constant number of atoms. Then a pair of strong counter-propagating Raman beams are applied to the atoms. An optical pumping laser is also applied with a slightly red detuning from the $|2\rangle \rightarrow |3'\rangle$ transition to recycle the atoms. The relative intensity between the Raman and optical pumping lasers determine the population distribution in the two ground states. By collecting the fluorescence of the light from the cold-atom cloud, while the frequency of the Raman laser is scanned slowly around the $|3\rangle \rightarrow |1'\rangle$ resonance ($\delta = 0$), Baudouin and coworkers observed the first evidence of random lasing in the cold atoms [4]. This procedure has been repeated for different b_0 (Fig. 2.15). In the experiment the total emitted fluorescence was collected in a small solid angle ($10^{-2} sr$), and for obtaining each curve in Fig. 2.15 the signal was averaged over many cycles (~ 4000).

Note that the detected fluorescence is the total emitted light by the atomic cloud and it contains the scattered light from two external lasers (Raman and optical pumping) as well as random lasing. The separation between the different lines is indeed experimentally very difficult because they all are at the same wavelength $\lambda = 780.24\,\text{nm}$ and differ only from a few megahertz or gigahertz. Moreover, in random lasers, there is not any privileged emission direction that allows one to spatially separate the random-laser light. In most random lasers, the separation is done either spectrally or temporally (using very short pump pulses), which is very important because the light scattered from the pump is much more intense than the random laser itself. In our system, however, the $|2\rangle \rightarrow |1'\rangle$ transition does not scatter light from the two external lasers. The random-laser line has, thus, a strength comparable to the one of the other involved trans-

itions and that is why it is possible to detect the random laser signal in the total fluorescence. It should also be stressed that in a conventional laser, the beam is well separated from the fluorescence of the gain medium, thanks to the cavity. This is not the case in our system, where both are measured together. Finally, it may be useful to have in mind that looking at the total emitted light is equivalent, due to energy conservation, to looking at the pump depletion (here the two external lasers).

In regions 1 of Fig. 2.15 where the scattering is low due to larger detuning from the $|2\rangle \rightarrow |1'\rangle$ transition, ASE makes an overall increase in the fluorescence as a function of optical thickness b_0. This is actually a signature of the collective behavior of the atoms. In this region photons from the Raman laser can perform a spontaneous Raman transition. Next, the subsequent scattered light can be amplified by the Raman gain. The efficiency of this process depends directly on b_0.

When the Raman laser is tuned close to $\delta = 0$ (region 2 of Fig. 2.15), the combination of gain and scattering gives rise to an enhanced fluorescence bump that emerges as the optical thickness b_0 is increased. Both scattering and gain, which are the fundamental ingredients of the RL, are present in this condition and thereby one can expect to have RL emission in this region if the system is above random lasing threshold. To investigate the random lasing threshold in this experiment, the supplementary fluorescence is depicted as a function of optical thickness b_0 (Fig. 2.16a). ASE effect though is removed by fitting the wings of the curves in regions 1, with adjustable slopes and curvatures, and then it is subtracted from corresponding data in region 2. The remaining signal is a bell-shaped curve, well-centered at $\delta = 0$ (Fig. 2.16b). Surprisingly, it is very well fitted by a Gaussian. We can thus use a Gaussian fit to extract its amplitude δP_{F} and width σ, as reported in Fig. 2.16b. Although the signal consists of different emission lines, a threshold of the peak amplitude is clearly visible, with a change of slope at $b_0 = 6 \pm 1$. This threshold was interpreted as the signature of random lasing occurrence in cold ^{85}Rb atoms when the Raman beams are tuned around $\delta \sim 0$ and when $b_0 > 6$. It should be stressed that varying the optical thickness in this system, acts simultaneously on the amount of gain and feedback provided by the medium. This is unusual in laser physics, where the threshold is most-commonly defined as a critical pump power. In this case, the optical-pumping intensity increases indeed the population inversion that provides gain, but simultaneously decreases the feedback, so that random lasing needs a fine tuning of the laser parameters.

The recent observation of cold-atom random lasing is in qualitative agreement with an ab initio model based on Letokhov's threshold [4]. There are, however, quantitative discrepancies. In particular, the measured threshold is lower than the predicted one. This might be due to interference and/or cooperative effects [84], which are neglected in the diffusion model. Several other ingredients are neglected and might also play a role, like the light po-

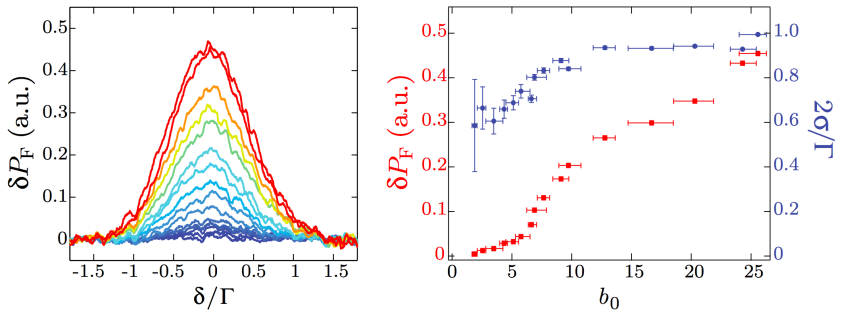

(a) (b)

Figure 2.16 – (a) Supplementary fluorescence around $\delta = 0$ for different optical thickness (same color scale as in Fig. 2.15). The raw data are the same as in Fig. 2.15 but the wings have been subtracted and the signal has been smoothed. (b) A Gaussian fit allows extraction of the amplitude (red squares) and the r.m.s. width σ (blue circles) of the curves shown in (a) as a function of the optical thickness b_0. The vertical error bars are the statistical uncertainties of the fit (not visible for the amplitude) and the horizontal error bars correspond to the fluctuations of b_0 on five shots. Adapted from Ref. [4].

larization, the Zeeman degeneracy of the involved atomic levels, the finite temperature of the cloud, and the inhomogeneous density distribution. This demonstrates the need for a more evolved modeling.

2.3 Optical coherence measurements

Although the cold-atom random laser has been observed recently, the observational evidence was indirect. As already explained in section 1.1.4, the optical coherence properties of the random laser can be used to detect random lasing emission and study the threshold in a more direct fashion. The optical coherence can also develop our knowledge about the nature of random laser light. Generally speaking, optical coherence of a light can be measured by various techniques. The degrees of first and second-order correlation, photon probability distribution, optical spectrum of light, and noise spectrum of the light intensity, provide information about the optical coherence. All these parameters are often connected. Depending on the experimental conditions and the available equipment, one of these parameters can be measured.

In this section, we briefly introduce and present some well known techniques of coherence measurement with a focus on the applications to a cold atomic sample. So far, some experiments have been implemented to inquire about the atomic physics imprinted by cold atoms on the scattered light. However, those experiments have been mainly performed in the single scattering regime.

2.3.1 Degree of first-order correlation measurement

The first-order correlation function $g^{(1)}(\tau)$ characterizes the temporal fluctuations in electric field. In optical interferometers such as Michelson and Mach-Zehnder interferometer, the interference visibility is related to $|g^{(1)}(\tau)|$. The pattern of interference fringes and therefore $|g^{(1)}(\tau)|$ depends on the nature of light incident on the interferometer. In Fig. 2.17, $|g^{(1)}(\tau)|$ is qualitatively depicted for coherent and chaotic fields. In section 1.1.4 it was mentioned that the degree of first-order spatial coherence can be investigated by a double-slit experiment. Since the fluorescence from the atoms is usually very weak, preparing an optical setup of these kind would be a main challenge.

According to the Wiener-Khinchin theorem, the degree of first-order coherence $g^{(1)}(\tau)$, is the Fourier transform of the optical spectrum $S_o(\omega)$.

$$g^{(1)}(\tau) = 2\pi \int_{-\infty}^{\infty} S_o(\omega) e^{i\omega\tau} d\omega. \tag{2.34}$$

The coherence time is then given by the inverse of the spectrum width, $\tau_c = 1/\Delta\omega$ [85]. Thus an alternative way to verify optical coherence is achievable by extracting the optical spectrum of light. The transmission of light through an appropriate high resolution Fabry-Perot cavity, for instance, can be used for spectroscopy of an unknown spectrum. Suppose that a light with an unknown spectrum, distributed at a certain frequency interval, is

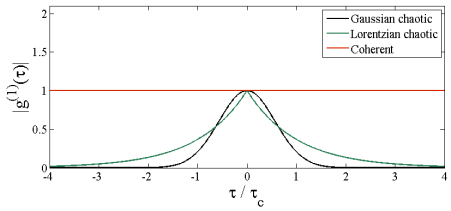

(a)

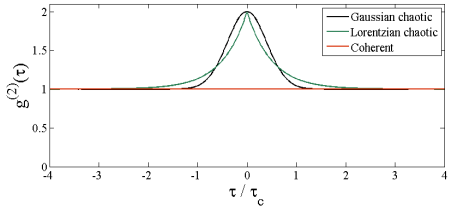

(b)

Figure 2.17 – (a) $|g^{(1)}(\tau)|$ and (b) $g^{(2)}(\tau)$ for chaotic and coherent light.

incident into a cavity. By scanning the length of the cavity, the transmission signal can be exploited to determine the optical spectrum of the incident light. However, the main challenge to successfully demonstrate spectroscopy by the Fabry-Perot is to have very narrow cavity linewidth compared to the spectrum under study. More details about the Fabry-Perot cavity are given in chapter 3. The Fabry-Perot interferometry was used to resolve the cold-atom random laser emission, but it failed due to the poor resolution of that cavity [86].

2.3.2 Intensity correlation measurement

Intensity correlation measurement (ICM) is a very popular technique for coherence measurement. ICM describes the temporal fluctuations of light intensity $I(t)$, based on the second-order correlation function $g^2(\tau)$ (Eq. 2.10). This technique was first demonstrated by Hanbury Brown and Twiss in 1956 [87] for investigation of the angular diameter of stars. This is commonly known as the HBT experiment. Nowadays, the HBT correlation measurement method is used in several scientific fields, including cold atoms [88].

The second-order correlation function was defined in Eq. 2.10. As an example in Fig. 2.17, $|g^{(1)}(\tau)|$ and $g^{(2)}(\tau)$ for coherent and chaotic lights are depicted. According to the Siegert relation for a light wave from a chaotic sample, first and second-order temporal correlation functions are related by

[36]

$$g^{(2)}(\tau) = 1 + S|g^{(1)}(\tau)|^2. \tag{2.35}$$

The factor S depends on the spatial coherence of the detected light. More specifically, $S \propto 1/N$ and N is the number of speckle grains included in the detection system. For a detector radius less than the coherent length of the scattered light S approaches unity. S decreases as the number of involved spatial coherence areas in the detection increases. According to Eq. 2.34, $g^{(2)}(\tau)$ also provides spectral information about the detected light.

It is straightforward to perform ICM for a light intensity as a function of time based on the definition of the $g^{(2)}(\tau)$ function. Bali and coworkers [17], for example, demonstrated ICM of the fluorescence of a cold atomic cloud (Fig. 2.18) by directly detecting scattered light from the atoms in the photon counting regime. Note that in the following experiments, which will be reviewed in this section, the cold atomic cloud is exposed by six counter-propagating laser beams, providing the fluorescence from the atoms. According to Fig. 2.18, a partially spatial coherence polarized fluorescence is detected by a photomultiplier tube (PMT) in a given solid angle. An amplifier and a discriminator system used for photon counting. The output is registered in the first channel of a 32-channel shift register. By each clock pulse with a period τ_{cl}, the data registered in each channel is shifted to the next one and new detected photon count is registered in channel 0. Counter A, counts and accumulates N_0 from channel 0 of the shift register which is equivalent of the detected intensity $I(t)$, while the coincidence counts N_n between first (0) and nth channels, obtained by an AND circuit, reflects the product $I(t)I(t + n\tau_{cl})$. Therefore in this experiment Eq. 2.10 can be rewritten as

$$g^{(2)}(n\tau_{cl}) = \frac{\langle I(t)I(t + n\tau_{cl})\rangle}{\langle I(t)\rangle^2} = \frac{N_n T_{det}}{N_0^2 \tau_{cl}}, \tag{2.36}$$

where T_{det} is the total duration of measurement and counting.

For a cloud of cold two-level atoms, the optical spectrum of the scattered light usually consists of two parts: a narrow (compared to the atomic linewidth) spectral peak due to the elastic Rayleigh scattering, and a broad resonance spectrum [89]. The width of the Rayleigh spectral peak is determined by Doppler broadening if the atoms are not confined in a microscopic potential well. The broad spectral feature depends on the intensity of the laser. If the driving laser has a low enough intensity, the Rayleigh contribution is dominant. For multilevel atoms, additional contributions appear in the optical spectrum [90]. For an atom at rest in zero magnetic field, the most important contribution is due to incoherent Raman scattering. Using the ICM setup depicted in Fig. 2.18, Bali and coworkers showed that in the absence of magnetic field ($B \approx 0$), the second-order correlation can be simply modeled based on the Doppler broadening of the light due to the temperature of the atomic cloud. The $S_o(\omega)$ can be described by a convo-

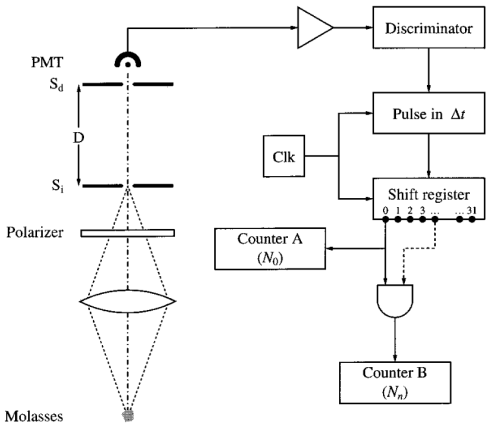

(a)

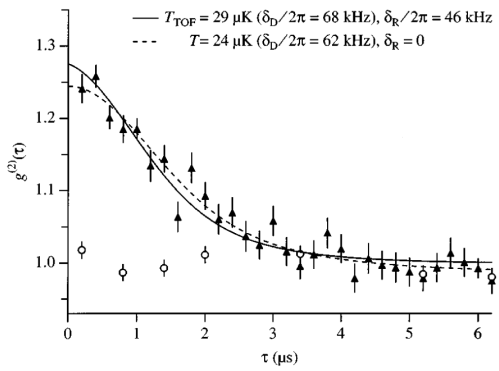

(b)

Figure 2.18 – (a) Schematic diagram of the apparatus for ICM of the scattered light from a cloud of cold atoms. The incoming fluorescence is made partially spatial coherent by a pair of pinholes, S_i and S_d, and detected by a photomultiplier tube (PMT) in a photon counting regime. The required ICMs are performed by the TTL circuitry. (b) Measurements of $g^{(2)}(\tau)$ as a function of delay time. The dashed and solid lines are fits assuming two models for the line shape. The circles are measurements of an incandescent source for calibration purposes. Reprinted from Ref. [17]

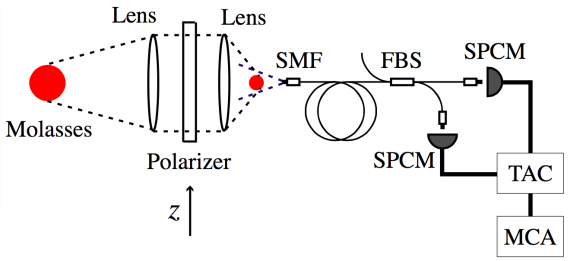

Figure 2.19 – Another scheme of ICM setup used in Ref. [91]. A single-mode fiber is directed at the reduced image of the cold-atom cloud and the mode-filtered light is led to a photon correlator. SMF: single-mode fiber, FBS: fiber beam splitter, SPCM: single photon counting module, TAC: time-to-amplitude converter, and MCA: multi-channel analyzer.

lution of Doppler broadened feature with the spectrum of the atom at rest, thus

$$|g^{(1)}(\tau)| = |g_D^{(1)}(\tau)||g_A^{(1)}(\tau)|, \tag{2.37}$$

where the inhomogeneous component $g_D^{(1)}(\tau)$ is the sum of the Doppler contributions from the laser beams traveling through the cloud along different coordinates [15]

$$g_D^{(1)}(\tau) = \sum_i a_i \exp\Big(-\alpha_i \frac{\sigma^2\tau^2}{2}\Big). \tag{2.38}$$

The parameter $\sigma = q\sqrt{k_B T/M}$ is the standard Doppler width, where q, k_B, and M are the wave number of the laser, Boltzmann constant, and the mass of the atoms respectively. Here, α_j reflects the dependence of the Doppler shift on the angle between the detection direction and the propagation direction of the jth laser beam. In the following, the homogeneous component $g_A^{(1)}(\tau)$ in Eq. 2.37 can be modeled by a coherent Rayleigh scattering contribution and an incoherent term corresponding to the Mollow triplet [89]. The temperature measured based on the above model was in agreement with another standard temperature measurement method [17]. Moreover they showed that the coherence time depends on the number of atoms in the cloud, due to the probability of multiple scattering events.

Based on the assumption of Eq. 2.37, Nakayama et al. [91] also performed a similar ICM experiment on the fluorescence of the cold atoms (Fig. 2.19). By increasing the time-averaged atom number, they performed a precise ICM and observed a strong photon bunching ($g^{(2)}(\tau = 0) \simeq 2$) and a rapid damped oscillation (Fig. 2.20). The oscillation structure in $g^{(2)}(\tau)$ can be described by the interference between the central coherent component and the incoherent side contribution of the Mollow triplet [91]. A similar modulation was observed and reported in Refs. [92, 93].

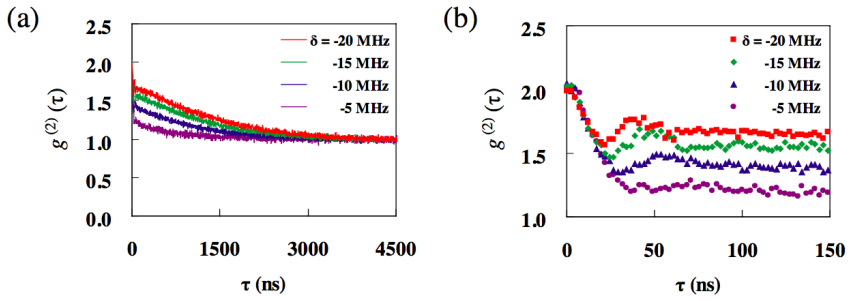

Figure 2.20 – Measurements of the second-order intensity correlation as a function of delay time for various detuning of the MOT beam. (a) Long-time decay of the correlation function which corresponds to the temperature of the cloud. (b) Short-time decay. The short decay time is determined by the lifetime of the atomic excited state. Adapted from Ref. [91].

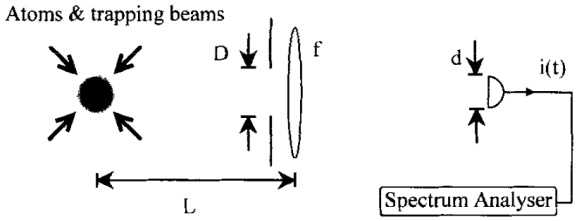

Figure 2.21 – Schematic diagram of the optical setup to measure the power spectrum. Reprinted from Ref. [16].

An alternative method of ICM is to study the power spectrum of a detected signal, i.e. by a spectrum analyzer. Jurczak and coworkers [16], used this method to investigate the correlation of fluorescence from cold atoms (Fig. 2.21). Similarly they assumed that the light emitted from N independent radiators (cold atoms) at a certain temperature results in a broad Doppler spectral feature. In the experiment they observed a narrow peak, which was interpreted as an evidence of confinement of the atoms into potential wells [15]. This is known as Lamb-Dicke effect and has a Gaussian form. The observed spectrum therefore contains one narrow peak, one broad pedestal corresponding to the Doppler effect, and finally a convolution of the two peaks. Using this model, Jurczak et al. fitted the experimental data and extracted the temperature of the cloud (Fig. 2.22). The measured temperature in this method was consistent with the result from another standard temperature measurement technique.

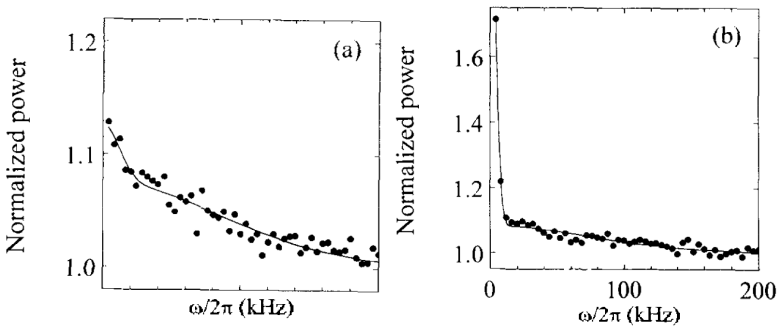

Figure 2.22 – Two power spectra of scattered light from a cold-atom cloud, normalized to the shot noise level for two different cloud temperatures. These spectra contains a narrow and a broad Doppler contributions. (a) $v_{rms} = \sqrt{k_B T/m} = 5\ cm/s$ and (b) $v_{rms} = 3.5\ cm/s$. Adapted from Ref. [16].

2.3.3 Homodyne and heterodyne detections

The direct detection of a light contains information about the intensity as well as the intensity noise of that source. In the case of a low intensity signal, the interesting noise under study can be smaller than the quantum noise limit (QNL). For a single mode field a combination of two detectors with a beamsplitter can be used to discriminate between a classical modulation and the quantum noise contribution. Furthermore, adding a reference beam to the signal, referred as local oscillator, one performs a homodyne detection system (Fig. 2.23). In order to explain the mechanism, firstly, let

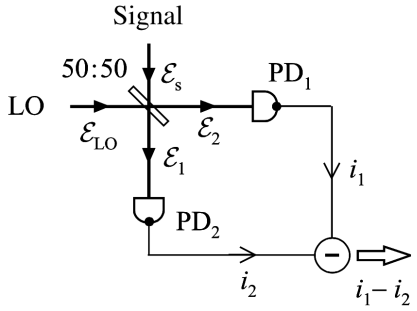

Figure 2.23 – Schematic diagram of the homodyne detection.

us represent the amplitude of two beams

$$\begin{aligned} \mathcal{E}_s(t) &= \mathcal{E}_s + \delta\mathcal{E}_s(t) \\ \mathcal{E}_{LO}(t) &= \Big[\mathcal{E}_{LO} + \delta\mathcal{E}_{LO}(t)\Big]e^{i\phi_{LO}}, \end{aligned} \tag{2.39}$$

where $\mathcal{E}_s(t)$ and $\mathcal{E}_{LO}(t)$ are respectively the incident signal and the local oscillator electric fields, and $\delta\mathcal{E}(t) = \delta X(t) + i\delta Y(t)$ is the relevant quadrature electric field. Here ϕ_{LO} represents the relative phase between local oscillator and main signal. Considering the case of an intense local oscillator and a weak input signal ($\mathcal{E}_{LO}^2 \gg \mathcal{E}_s^2$), we can assume that the detected intensities at the two detectors are approximately the same and only correspond to the local oscillator intensity

$$|\mathcal{E}_{D1}|^2 \approx |\mathcal{E}_{D2}|^2 \approx \frac{1}{2}|\mathcal{E}_{LO}|^2. \tag{2.40}$$

Under the above assumption one can drop all the terms related to $\mathcal{E}_s$ compared to $\mathcal{E}_{LO}$. The signal at the two detectors can be described, taking into account the π radian phase shift for one of the reflected beams in a single beamsplitter [85], as following

$$\begin{aligned} \mathcal{E}_{D1}(t) &= \sqrt{\frac{1}{2}}\big(\mathcal{E}_{LO}(t) + \mathcal{E}_s(t)\big) \\ \mathcal{E}_{D2}(t) &= \sqrt{\frac{1}{2}}\big(\mathcal{E}_{LO}(t) - \mathcal{E}_s(t)\big), \end{aligned} \tag{2.41}$$

The photo-currents from the two detectors then are proportional to $|\mathcal{E}_{D1}|^2$ and $|\mathcal{E}_{D2}|^2$

$$|\mathcal{E}_{D1}|^2 = \frac{1}{2}\big(|\mathcal{E}_{LO}(t)|^2 + \mathcal{E}_{LO}(t)\mathcal{E}_s^*(t) + \mathcal{E}_{LO}^*(t)\mathcal{E}_s(t) + |\mathcal{E}_s(t)|^2\big), \tag{2.42}$$

which can be approximated as

$$|\mathcal{E}_{D1}|^2 = \frac{1}{2}\Big[|\mathcal{E}_{LO}|^2 + 2\mathcal{E}_{LO}\delta X_{LO}(t) + 2\mathcal{E}_{LO}\big(\delta X_s(t)\cos\phi_{LO} - \delta Y_s(t)\sin\phi_{LO}\big)\Big], \tag{2.43}$$

by neglecting terms such as $\mathcal{E}_{LO}\mathcal{E}_s^*$ compared to $|\mathcal{E}_{LO}|^2$ and $\mathcal{E}_s\delta X^*$ or $\mathcal{E}_s\delta Y^*$ compared to $\mathcal{E}_{LO}\delta X^*$ or $\mathcal{E}_{LO}\delta Y^*$. Moreover all higher terms in δX and δY have been ignored. A similar equation can be written for the detected signal at the second detector. Now based on the Eq. 2.43, the difference current $i_-(t)$ from the two detectors is estimated by

$$i_-(t) \approx 2\mathcal{E}_{LO}\big(\delta X_s(t)\cos\phi_{LO} - \delta Y_s(t)\sin\phi_{LO}\big). \tag{2.44}$$

This is a remarkable result. Firstly, the output signal scales only with the amplitude of the local oscillator, and the noise associated with the local oscillator is suppressed. Secondly the power of the input beam has no influence,

as long as it is small compared to the power of the local oscillator. Finally, the noise of the input beam is now amplified and can be above the QNL, which makes it easier to investigate, and the result would not be affected [85]. The variance of the difference current $i_-(t)$ can be also evaluated

$$\Delta i_-^2 \approx 4|\mathcal{E}_{LO}|^2\big(\delta X_s^2 \cos^2\phi_{LO} + \delta Y_s^2 \sin^2\phi_{LO}\big). \tag{2.45}$$

This technique is phase sensitive. In case that the relative phase ϕ_{LO} is not preserved in time, the fluctuations in the two quadrature components are not distinguishable.

If a local oscillator has the same frequency as the input signal, the detection is called balanced homodyne, and if there is a frequency difference Δf between them, the frequency spectrum of the input signal would be shifted by Δf. This technique is commonly called optical heterodyne detection. The main advantage of heterodyne detection is that due to beating, one can avoid the low frequency noises, such as the flicker and electronic noises. A frequent application of the heterodyne detection is the laser linewidth measurement by detecting beat-note signal between two lasers of different frequency.

Based on the heterodyne technique Westbrook et al. [15] studied the effect of spatial confinements of cold atoms in potential wells (Fig. 2.24). A pair of laser beams makes an optical standing wave and provides potential wells for the atoms. The efficiency of the localization of atoms and the depth of the potential wells can be controlled by the detuning of the laser beams. They observed a very narrow feature in the spectrum of the fluorescence (Fig. 2.24b). Similarly Yoon and coworkers [94] used a heterodyne detection in the photon counting regime to study a similar effect.

2.3.4 Noise in the forward direction

So far, all the methods explained here study the fluorescence of a sample. However a very convenient method could be to monitor the fluctuations of a beam transmitting through a cloud of cold atoms. This can be done by probing the intensity noise of the transmitted light by a photo-detector. The privilege of this method is that the optical setup is very simple. Also the signal is usually stronger than the fluorescence and depends on the incident intensity, as long as it is less than the saturation intensity for the atoms. Although the photo-detector is not directly sensitive to the phase and frequency of the incident light, atoms likely convert the phase or frequency fluctuations into amplitude noise. The conversion depends on the intrinsic and essential frequency noise of the laser, as well as some physical parameters of the atoms. More details are given in chapter 4.

Based on this method, Florez and coworkers [95] studied the intensity correlation of the transmitted laser beams through the cold atoms under the condition of electromagnetically induced transparency (EIT). In order

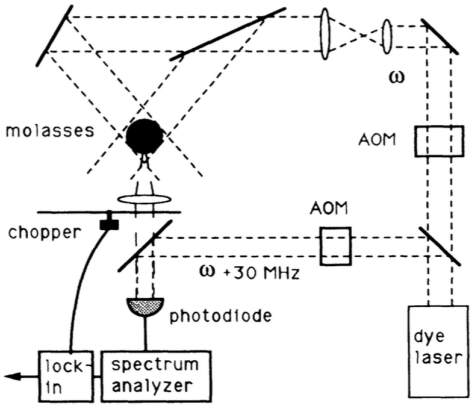

(a)

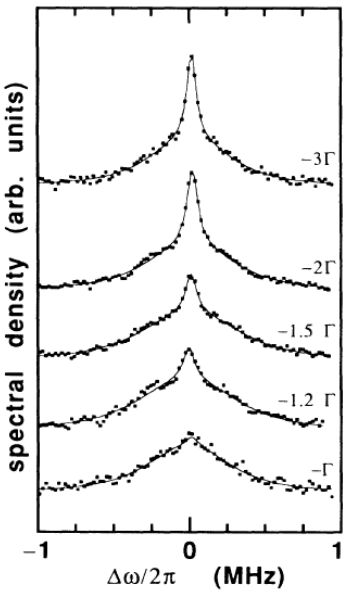

(b)

Figure 2.24 – (a) Schematic diagram of the heterodyne detection used in Ref. [15]. (b) Heterodyne spectra with a resolution bandwidth of 30 kHz at different detuning. The relative vertical scale between the spectra is arbitrary. Reprinted from Ref. [15]. Similar to Fig. 2.22 they referred the narrow part of the spectra to the spatial confinement of the atoms in potential wells.

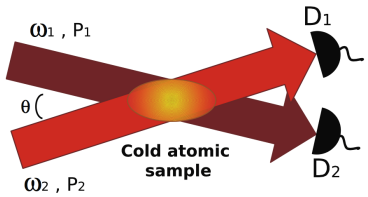

Figure 2.25 – Schematic diagram of the transmission detection used in Ref. [95] to investigate the EIT effect by performing cross-correlation between two detectors.

to prepare a proper condition of EIT, they used two laser beams at two different frequencies transmitted through the atoms, and a cross correlation of the two transmitted beams was carried out to extract the spectroscopic features of the EIT line (Fig. 2.25). This technique is also very popular in noise spectroscopy [96].

2.3.5 Photon counting statistics

As it was already discussed in section 1.1.4, the photon distribution can describe whether a light is a coherent (i.e. Poisson distribution) or a chaotic source (i.e. B-E distribution). In general, one can consider light as a partially coherent source which has both Poisson and B-E contributions with different weight (Fig. 2.26). It was explained in section 1.2.4 that the RL emission from cold atoms contains ASE as well. Since the ASE has B-E photon statistics [41], this technique can be applied to study the proportion of RL emission among the total fluorescence from the cold-atom sample (Eq. 2.17). Furthermore, one can monitor this coherent percentage while the optical thickness of the sample is changing. This is a practical method to investigate the threshold conditions (similarly to the experiments done in Refs. [13, 12]).

Suppose that a PMT or an avalanche photodiode (APD) with high quantum efficiency is connected to an electronic counter. It counts and registers the number of detected photons within a certain time interval which is set by the user, with an average count rate of $\mathcal{R}$. Now, by choosing a time segment smaller than the coherence time of the emitted light, we can extract the photon probability distribution.

2.3.6 Coherence measurement of cold-atom RL

To this end, we reviewed several known techniques and methods for optical coherence measurements. These techniques are usually equivalent, and based on the physics we want to study and the experimental situations one of those methods can be chosen and implemented. Now in this section,

Table 2.3 – Summarizing different known techniques for studying the noise properties of the light from the cold atoms. FP: Fabry-Perot cavity, ICM: intensity correlation measurement, SNR: signal to noise ratio, and LO: local oscillator.

Technique	**Related function**	**Advantages/ Disadvantages**	**Schematic diagram**	Ref.
		Fluorescence		
FP	$S_o(\omega)$	Needs a cavity linewidth narrower than the expected emitted spectrum		[86]
ICM (P.C.)	$g^{(2)}(\tau)$	Simple optical setup For the RL: Long integration time		[17] [91] [93]
Noise spectrum	$S_i(\omega)$	For the RL: Long integration time	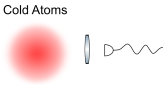	[16]
Photon statistics	$P(n)$	Only gives $g^{(2)}(0)$ For the RL: Long integration time		
Balanced homodyne detection	$g^{(1)}(\tau)$ $S_o(\omega)$	Enhanced SNR Independent from signal power Phase lock needed between LO and signal	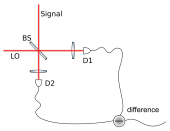	
Heterodyne detection	$g^{(1)}(\tau)$ $S_o(\omega)$	Enhanced SNR Avoiding low frequency technical noises Phase lock needed between LO and signal	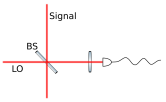	[15]
		Transmission		
Transmission Noise	$S_o(\omega)$	Enhanced SNR Simple optical setup Not appropriate to RL	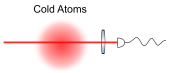	[95]

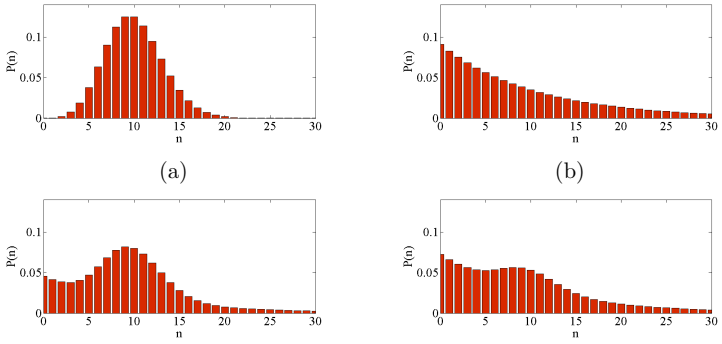

Figure 2.26 – Photon probability distribution with $\bar{n} = 10$ for a (a) coherent, (b) chaotic, (c) partially coherent with coherence percentage $\alpha = 50\%$, and (d) partially coherent light with $\alpha = 20\%$.

physical conditions which are in our areas of concern, will be described. As a long term goal, the verification of the random laser emission, by investigating the optical coherence of the fluorescence of a cold-atom cloud, is our main interest. However, this fluorescence might be a mixture of single and multiple scattered photons in the presence of the gain. Moreover the trivial fluctuations and noise of the repumper and the Raman lasers can affect the final results. Thus in order to reduce the complexity of such system, it would be better to start with the characterization of the lasers being used on the experiment. Parameters like linewidth, intensity and frequency noise of the lasers ought to be carefully investigated in the first step. Next, the coherence properties of light in a single scattering regime has to be characterized. In the past two decades, some experiments have been implemented under this circumstances which help to develop a comprehensive model for a single scattered light through the cold atoms. Then, we need to characterize the light multiply scattered. To our knowledge, this has not been reported yet in the cold-atom community. However there are already some models which were developed for a strongly multiple scattering regime. Diffusive wave spectroscopy, for instance, has been developed to study the dynamics and motions of suspended particles based on the diffusion of light. Similarly it can be applied to moving atoms in a cloud. Next, the effect of adding the gain will be taken into account. Finally by changing optical thickness of the atomic cloud we can investigate the RL threshold. In the final stage, all the fundamental conditions for random lasing are fulfilled. In this strategy, we might be able to observe an evidence of the cold-atom random lasing threshold in the coherence properties of the fluorescence of light from MOT.

2.4 Conclusion

In this chapter, we introduced a new exotic type of laser. Random lasers work on the same principles as conventional lasers, but here the modes are determined by multiple scattering and not by a laser cavity. Therefore a random laser is a mirrorless laser but not modeless. Moreover, we saw that the optical coherence of random lasers is predicted as a coherent emission above threshold and it exhibits Poissonnian photon statistics, just like a conventional laser. This kind of laser has been observed in many different materials, including a cloud of cold rubidium atoms. However it is very difficult to spatially and spectrally resolve this cold-atom random laser, since there is no privileged direction for the emission and the frequency of scattered light are very close to the emission frequency. Coherence measurement though is a powerful tool for verifying random laser. It can help to study the coherent nature of random lasing emission, as well as the threshold conditions. Thus a brief overview of some practical techniques for performing coherence measurements in our cold-atom experiment were presented. Also in order to understand the results of a coherence measurement of a random laser and avoid complexity of such experiment, we proposed to study the coherence properties of light in different regimes and conditions, approaching the required situation for random laser emission. These conditions could contain light scattered in a single scattering regime, then multiple scattering, next we have to consider the effect of combining gain to this system, and finally threshold conditions have to be fulfilled. Thus it would be easier to understand the transition from one regime to another.

Chapter 3

Cold-atom ^{85}Rb setup at INLN

In this chapter we will explain the experimental setup of cold atoms stressing new features and techniques in our experiment. The basics of the experiment has already been explained in Ref. [70]. Therefore in this chapter we give more details about the present optical setup of the cooling and repumping beams and the items which have been upgraded. Also we present some technical information about controlling and running the experiment. Furthermore, we explain the techniques used for characterization of our cold atomic cloud. Historically this cold-atom ^{85}Rb setup at INLN has been used for observation and investigation of different phenomena such as the coherent back-scattering (CBS) [97, 98], radiation trapping [56], optomechanical instabilities [99], the gain mechanisms [69], scaling laws for large magneto-optical trap [70, 100], and the cold-atom random laser [4, 68, 86].

3.1 The laser system

In order to implement a Magneto-Optical Trap (MOT), at least two lasers are needed, one to cool down the atoms and the other to re-pump and maintain atomic population in the proper ground state.

In our experiment however, two lasers are employed to make the cooling process. First a Distributed Bragg Reflector (DBR) laser diode (Yokogawa YL78XN), with relatively low intensity and frequency noise, is used as a master laser. This laser has a nominal optical power of about 5 mW and a linewidth of 2 MHz and it is locked via the saturated absorption spectroscopy on the cross-over (CO_{23}) $F = 2 \rightarrow F' = 3/F = 2 \rightarrow F' = 2$ transitions of the ^{87}Rb. Next, we have a Distributed Feedback (DFB) laser diode as our cooling laser. This laser diode provides approximately 30 mW. Its frequency is locked and stabilized by the offset lock technique using the master laser as the frequency reference and providing about 1 GHz offset. The principles of this locking technique are explained in the next section. The number of captured atoms in a large MOT scales as the sixth power of the cooling beam waist size at a given optical power, $N \propto w^6$ [102]. On the other hand by enlarging the trapping beams and keeping the intensity near saturation, the optical power has to be increased as the square of the waist size, $P \propto w^2$. Thus in order to trap a large number of atoms we need more optical

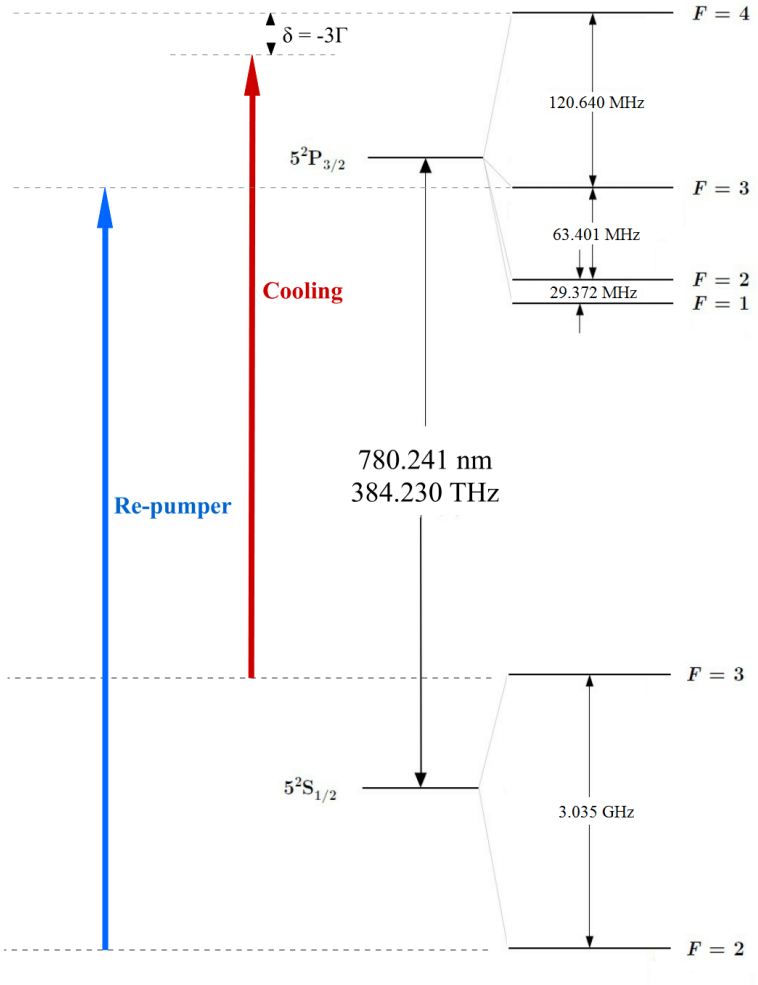

Figure 3.1 – Atomic hyperfine structure of the D2 line of ^{85}Rb and the transitions used for trapping and re-pumping the atoms (Ref.[101]). The cooling laser is tuned to $F = 3 \rightarrow F' = 4$ atomic transitions with a slightly red detuning ($\delta = -3\,\Gamma$) while the re-pumper laser is tuned to $F = 2 \rightarrow F' = 3$. Level spacing are not drawn to scale.

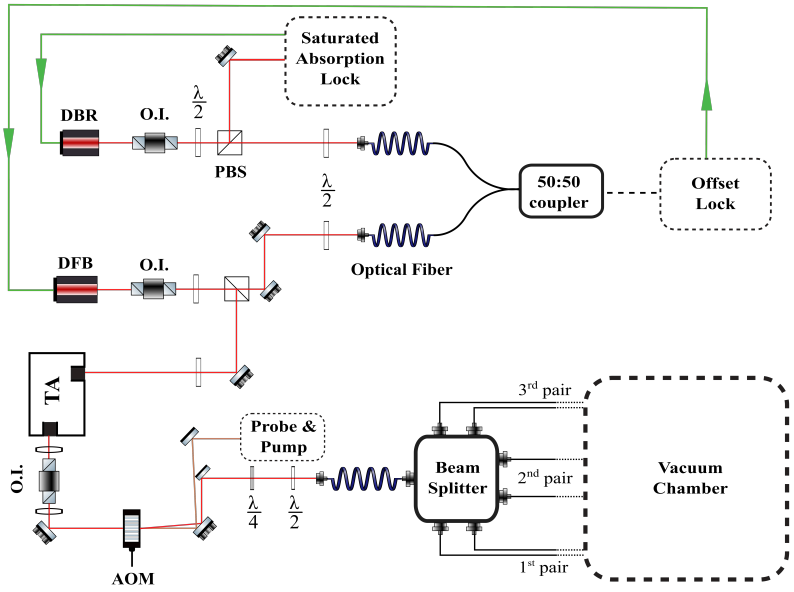

Figure 3.2 – An overview of the optical setup of the cooling beams. O.I. stands for optical isolator, $\lambda/2$ is half-wave plate, $\lambda/4$ is quarter-wave plate, PBS is polarized beam splitter, AOM is acousto-optical modulator, and TA is tapered amplifier. Green lines indicate the feedback lock signals.

power, so a tapered amplifier (TA, model: TEC-400) [103] is exploited for amplification up to $1W$.

In addition, to make the re-pumping process another DFB laser diode is used with 80 mW optical power and linewidth of about $2-3$ MHz. This laser is locked to the CO_{23} ($F=2 \rightarrow F'=3/F=2 \rightarrow F'=2$) of the ^{85}Rb transitions again by the saturated absorption technique. Its frequency is shifted by two AOMs in single-pass (switch on and off, $\omega_{AOM}=-105$ MHz) and double-pass (frequency scan, $\omega_{AOM}=+75.67$ MHz) configurations to reach the $F=2 \rightarrow F'=3$ transition. The schematic of the optical setup is depicted in Fig. 3.2 and 3.3.

3.2 Offset lock

3.2.1 Offset lock vs AOM frequency shifting

The first step in preparing and manipulating of the cold atoms is to control the frequency of the lasers in the experiment. In the old version of this cold-atom setup, conventional saturated absorption locking has been employed

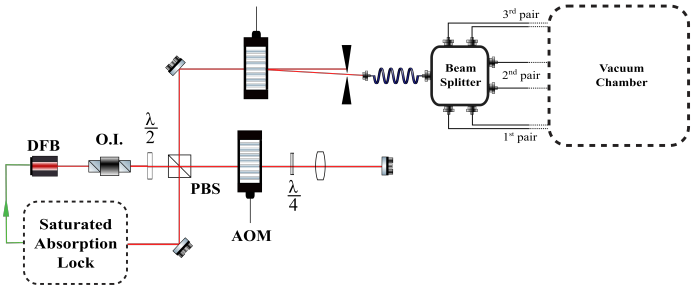

Figure 3.3 – Schematic optical setup of the re-pumping beams. Two AOMs are used in this setup. The upper AOM switches on and off (single pass configuration), and the bottom one is being used to scan the frequency of the laser without misaligning the beam (double pass configuration). Green line indicates the feedback lock signal.

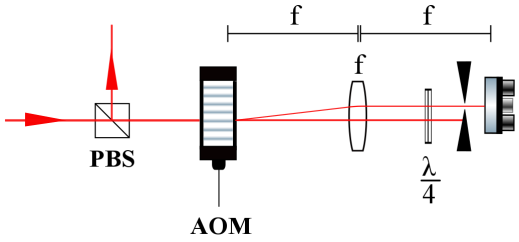

Figure 3.4 – Schematic configuration of the double-pass AOM. This configuration is suitable for scanning the incident beam over a frequency range which is limited by the frequency dependent diffraction efficiency of the AOMs.

for laser frequency stabilization. The saturated absorption locking fixes the frequency of a laser based on an atomic transition, but then in order to vary or scan the frequency during the experiment we need to use an acousto-optical modulator (AOM) in the double pass scheme (Fig. 3.4). Since the efficiency of the AOM depends on the frequency shift, the main limitation of this locking technique is the range of frequency shift it can support. This means that during a frequency scan, the diffraction efficiency and therefore the power of the diffracted beam change. In Fig. 3.5 we compared the optical power variation of a double-pass AOM with the power variation in our offset lock, while the frequency of the laser is scanned. Moreover there would be some losses of the optical power each time the beam passes through the AOMs.

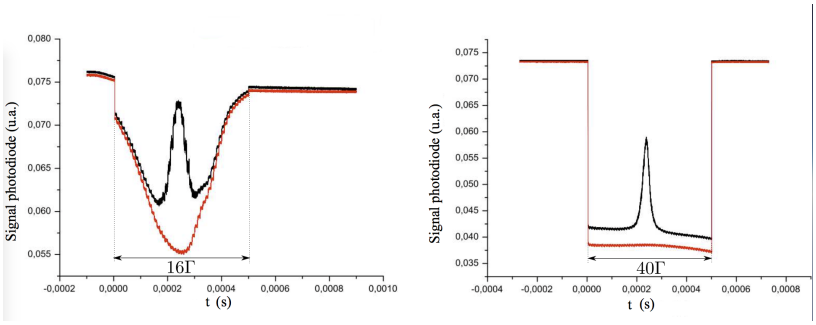

Figure 3.5 – Comparison of the intensity dependence of the probe beam while its frequency is being scanned by an AOM (left) and by the offset lock-in (right). The red line corresponds to the incident probe intensity and the black one corresponds to the transmission of that probe beam through the atoms. Note that the detector gain factor is negative and the range of frequency scan is much larger in the right figure. The flat part at the top of each figure corresponds to the background detection signal when the probe laser beam is switched off. It is clear that the output intensity of the AOM changes a lot during the scan, while on the contrary it is quite stable when the offset lock is used [86].

As it is mentioned in chapter 1, in order to perform a random laser, the frequency of a pump beam has to be tuned to the $F = 3 \rightarrow F' = 1$ transition to provide the Raman gain. In our cold-atom setup the pump beam is taken from the same laser which provides also the cooling beams (see Fig. 3.2). Therefore during the experiment the frequency of this laser has to be shifted frequently in a range of approximately 200 MHz. This large frequency span is very difficult to achieve through the AOMs without changing the optical power. By contrast, in the offset lock system, a large frequency scan with no power dependence is very easy to obtain (Fig. 3.6).

Furthermore to realize the cold-atom random laser, the frequency of the Raman beam has to be swept over a range of approximately 20 MHz (see Sec. 1.2.4). It is critical to preserve the power of Raman laser while its frequency is being scanned, otherwise one needs to renormalize the gain parameter. On the other hand the gain has a nonlinear response to the Raman laser power, and renormalization would be very difficult. Hence to avoid this complexity, it is important to keep a constant intensity for the Raman beam during the frequency scan.

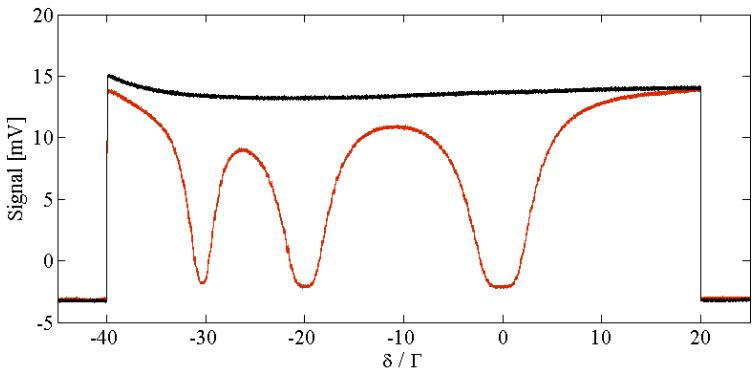

Figure 3.6 – Hyperfine structure of ^{85}Rb $5^2P_{3/2}$ level. The frequency of the transmitted probe beam was scanned by the offset lock-in in a range of $[-40\,\Gamma : 20\,\Gamma]$ during $8ms$. $\Gamma = 6.06\,\text{MHz}$ is the natural atomic linewidth of the rubidium atoms. This range of frequency sweep is much beyond the AOMs working range.

3.2.2 Beat-note profiles

When two laser beams with different frequencies but same polarization are superimposed on a photo-detector, the optical intensity measurement shows a signal at the difference between the optical frequencies, which is known as beat-note. It can be modeled as follows

$$\begin{aligned} E_1(t) &= E_m cos([\omega_m + \Delta\omega_m(t)]t) \\ E_2(t) &= E_s cos([\omega_s + \Delta\omega_s(t)]t), \end{aligned} \tag{3.1}$$

where $E_1(t)$ and $E_2(t)$ are the electric field of the master and slave lasers with mean optical frequency $\omega_m/2\pi$ and $\omega_s/2\pi$ respectively and $\Delta\omega(t)$ is a random frequency fluctuation of each laser and characterizes the linewidth of the laser. Thus the intensity at the detector would be

$$\begin{aligned} I(t) \propto\ & \frac{E_m^2 + E_s^2}{2} \\ & + E_m E_s cos([\omega_m + \Delta\omega_m(t) + \omega_s + \Delta\omega_s(t)]t) \\ & + E_m E_s cos([\omega_m + \Delta\omega_m(t) - \omega_s - \Delta\omega_s(t)]t). \end{aligned} \tag{3.2}$$

The first term in Eq. 3.2 is the DC intensity component, the last term is the beat component between two lasers, and the rest are high frequency components which are filtered out in the photo-detection process. Obviously to observe a beat-note signal, the optical frequency difference between two lasers must be within the bandwidth of the photo-detector. The Fourier

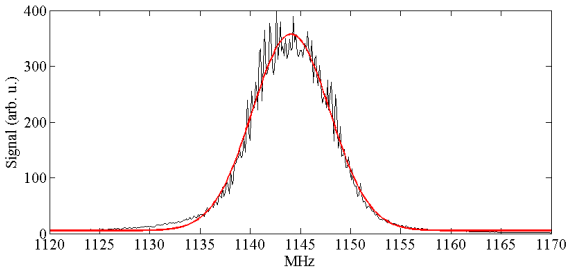

Figure 3.7 – A beat-note profile between our DFB and DBR lasers. Applying a Gaussian fit gives a width (FWHM) of 9.3 MHz for this beat-note profile.

transform of the detected optical intensity gives a δ-function at $|\omega_m - \omega_s|$ if $\Delta\omega_m$ and $\Delta\omega_s$ are infinitely small. However for a real laser, $\Delta\omega$ has a distribution with a certain width. In this case, the beat-note has a distribution and width which depends on the shape and the width of each $\Delta\omega$. As it is shown in the Fig. 3.8, there are two lasers superposed on a fast photodiode. The beat-note profile is the convolution of the two laser lineshapes. In the case of two Gaussian laser optical spectrum, it results in a Gaussian beat-note profile and its width is the quadratic sum of the two laser linewidths

$$\Delta\nu_{\mathrm{BN}} = \sqrt{\Delta\nu_{\mathrm{DBR}}^2 + \Delta\nu_{\mathrm{DFB}}^2}, \tag{3.3}$$

where $\Delta\nu_{\mathrm{DBR}}$ and $\Delta\nu_{\mathrm{DFB}}$ correspondingly are the linewidth of our master and slave lasers. If the laser line shapes are supposed to be Lorentzian, then the width of the beat-note will be

$$\Delta\nu_{\mathrm{BN}} = \Delta\nu_{\mathrm{DBR}} + \Delta\nu_{\mathrm{DFB}}. \tag{3.4}$$

Finally if one of the lasers is supposed to have a Gaussian line shape and the other has a Lorentzian, that gives a Voigt profile for the beat-note. In an interesting case, if one of the lasers is much narrower than the other one, the beat-note width is approximately the same as the linewidth of the broad laser. In the Fig. 3.7 a beat-note profile between our master and slave lasers is represented.

3.2.3 Electronics

In order to understand how this locking technique operates, it is useful to discuss the electronic ingredients. The frequency offset locking diagram is depicted in Fig. 3.8 [104]. The beat-note of the master and slave lasers is detected by a fiber coupled fast photo-diode (PD model: Thorlabs SV2-FC, bandwidth 2 GHz) and amplified by two consecutive very low noise amplifiers (ZX60-3018-G-S+). As mentioned before, the

frequency of the master laser is stabilized and locked to the ^{87}Rb CO_{23} ($F = 2 \rightarrow F' = 3/F = 2 \rightarrow F' = 2$) transition. The measured beat-note frequency (ω_{BN}) corresponds to the frequency difference between master and slave lasers (which is about 1 GHz). Thus the drift in the beat-note frequency is due to the changes in the frequency of slave laser. Using a radio frequency (RF) mixer (ZFM-11-S+) the output signal is mixed with the RF signal of a VCO (ZX95-1300-S+). The frequency of VCO (ω_{VCO}) is controlled via a computer and a high-speed voltage output card (National Instruments, model PCI6723) by setting the VCO input voltage level between 0 V and 20 V (Fig. 3.9). In the mixer, ω_{BN} is mixed and therefore it makes both frequency sum ($\omega_+ = \omega_{\mathrm{BN}} + \omega_{\mathrm{VCO}}$) and frequency difference ($\omega_- = |\omega_{\mathrm{BN}} - \omega_{\mathrm{VCO}}|$). Then by applying a low pass filter with frequency cut-off at 550 MHz (BLP-550+) the frequency sum can be eliminated and only the frequency difference is selected (of course this selection depends on the values of the ω_{BN} and ω_{VCO}). Next, the signal at ω_- is equally split (ZFSC-2-11+) into two outputs, one passes through a high-pass filter with frequency cut-off at 300 MHz (BHP-300+) and the other passes through a low-pass filter with frequency cut-off at 250 MHz (BLP-250+). Both signals are then detected by two RF power detectors (ZX47-LN-S+) and subtracted to produce the error signal. As it is depicted by a dotted box in Fig. 3.8, the combination of both low-pass and high-pass filters performs a radio frequency (RF) filter. This RF filter can be characterized by ω_{filter} which corresponds to the input modulation frequency that produces null signal at the output of subtractor (I). Finally this error signal is fed into a PI controller (Proportional Integrator) to generate the feedback signal which controls and stabilizes the frequency of the slave laser by keeping the output of subtractor I around zero. This feedback signal is sent to the current supply and is added to the current which feeds the slave laser diode. By changing the input voltage to the VCO we can vary the frequency of our laser. Therefore ω_{VCO} needs to be calibrated as a function of input voltage (Fig. 3.9).

This lock loops is stable and keeps the lock for a couple of days. Moreover the working frequency range of this lock system, without losing the lock, is approximately 500 MHz.

3.2.4 Speed of frequency scan

Since the frequency of the cooling beams as well as probe and pump beams are controlled by the offset lock, one important parameter is how fast it can change the frequency from one value to another. In other words what is the maximum speed of frequency scan in closed loop. In order to characterize this parameter, an instantaneous jump of the target frequency is applied to the laser while it is locked. Consequently the error signal of the servo shows a jump and then it goes back to zero with an exponential time constant

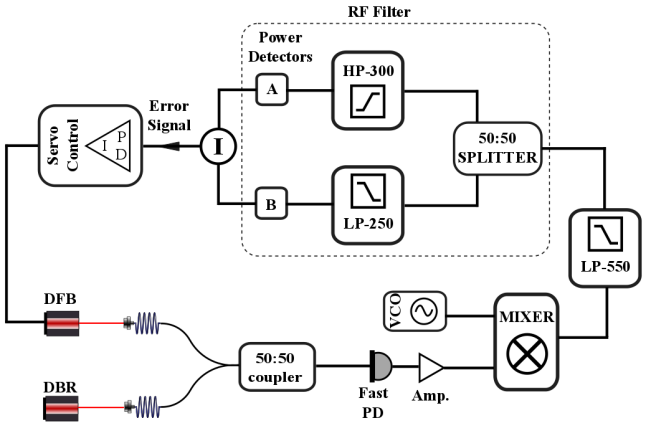

(a)

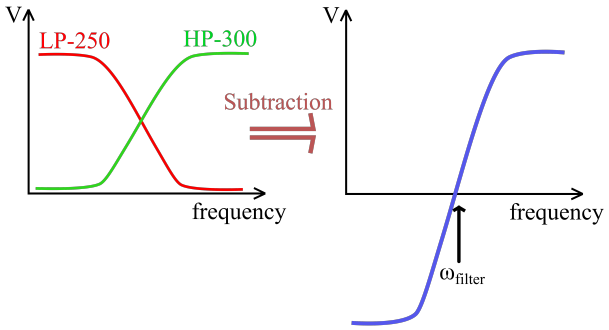

(b)

Figure 3.8 – (a) The offset lock-in scheme. Details about each electronic element and how it works are given in the text. (b) A schematic diagram of the output voltage of the two high-pass and low-pass RF filters and the result of the subtractor as the error signal.

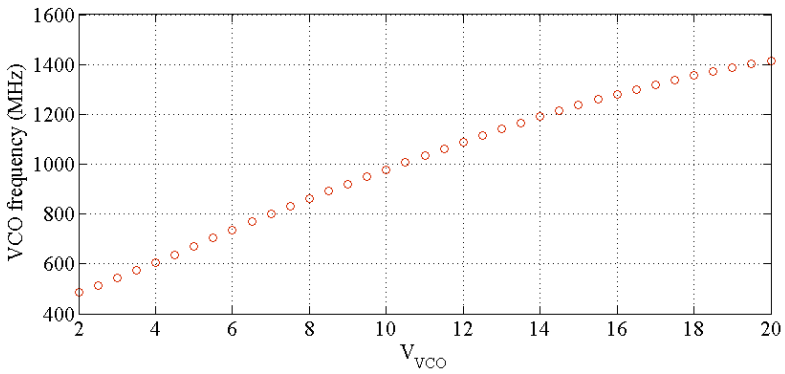

Figure 3.9 – The calibration of the VCO which controls the offset lock. The feeding voltage of this VCO varies between 1 and 20 V, which corresponds to a range of [487 : 1416] MHz frequency in the output signal.

of approximately 50 μs. The required time to reach the target frequency represents the speed of lock. According to Fig. 3.10 a 500 μs time delay in our servo system ensures proper frequency for the laser by offset lock in the range of -7 to $7\,\Gamma$. Note that this speed depends on the electronic gain parameters of the Proportional-Integral controller (PI). Although the offset lock provides a large range of frequency scan without variation in the laser power, as a drawback it is slower compared to the saturated absorption lock.

3.2.5 Adjusting the offset frequency

For our MOT experiment, to trap the ^{85}Rb isotope, the DFB laser used for cooling atoms has to be tuned and locked to the atomic transition of $F = 3 \rightarrow F' = 4$ albeit with a small red detuning ($\delta_{MOT} \approx -3\,\Gamma$). Since the master laser is locked to the CO_{23} ($F = 2 \rightarrow F' = 3/F = 2 \rightarrow F' = 2$) transition of ^{87}Rb isotope, an offset of 1259.8 MHz is needed to adjust the right frequency for the trapping beams, as it is also indicated in the Fig. 3.12 [101]

$$\frac{\omega^{85}_{34'}}{2\pi} = \frac{\omega^{87}_{CO_{2,3}}}{2\pi} + 1259.813(7)\ \text{MHz}. \tag{3.5}$$

On the other hand, the beat-note frequency of master and cooling lasers, once they are locked, is determined by

$$\omega_{\text{BN}} = \omega_{\text{VCO}} + \omega_{\text{filter}}, \tag{3.6}$$

where ω_{filter} is the crossover frequency of the output of subtractor in Fig. 3.8. We characterized the $\omega_{\text{filter}} = 253$ MHz (Fig. 3.11) which is determined

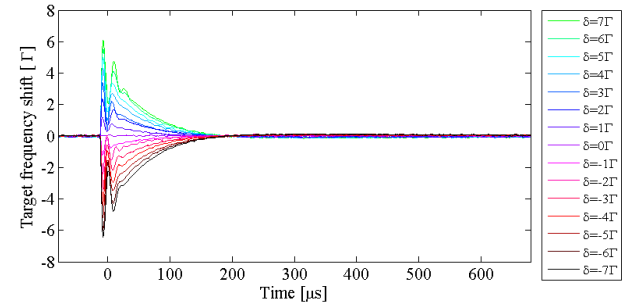

(a)

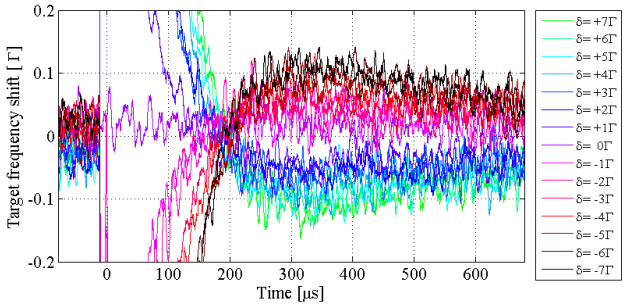

(b)

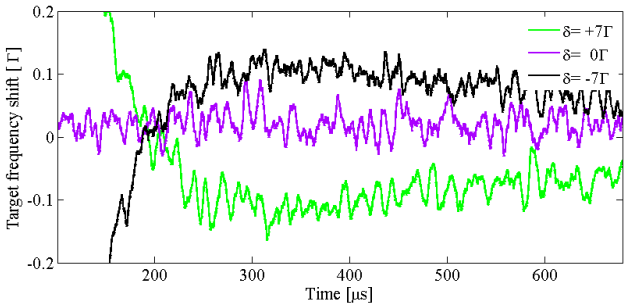

(c)

Figure 3.10 – (a) Time evolution of the error signal in the offset lock after an instantaneous jump of the target frequency at $t = 0$. Consequently the error signal goes back to zero ($\pm 0.1\,\Gamma$) at $t \approx 500\,\mu$s, which represents the speed of our offset lock in the range of $[-7\,\Gamma : 7\,\Gamma]$. (b) and (c) Zoom on the error signals.

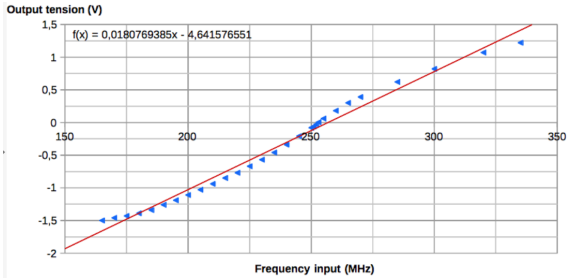

Figure 3.11 – Calibration of the RF filter in the offset lock. The vertical axis represents the output voltage of the subtractor. The input frequency of 253 MHz returns zero output voltage .

by the high and low pass filters. Fig. 3.11 is obtained by injecting a RF signal with a certain frequency to the RF filter (dotted box in Fig. 3.8), and recording the voltage of the signal at the output of the subtractor I. In order to switch the trapping beams on and off, we use an AOM (Acousto-Optical Modulator) in a single-pass configuration (Fig. 3.2). The frequency of this AOM is set at 100 MHz, and the first order diffraction beam is selected which leads to $\omega_{AOM} = +100\,\text{MHz}$. As a consequence,

$$\begin{cases} \omega_{\text{VCO}} = 907\,\text{MHz} \rightarrow \delta_{MOT} = 0 \\ \omega_{\text{VCO}} = 889\,\text{MHz} \rightarrow \delta_{MOT} = -3\,\Gamma. \end{cases} \tag{3.7}$$

3.3 Fibered setup for 6 beams MOT

For cooling the atoms we need six mutually perpendicular beams intersecting at the center of our vacuum chamber. Previously dividing the cooling and re-pumper beams had been done by polarizing beam-splitter (PBS) in free space. After upgrading our setup, we are using a polarization-maintaining (PM) optical fiber for the cooling and re-pumping beams (Fig. 3.13). One of the advantages of this new set-up is the stability of the alignment of the MOT and re-pumper beams at the MOT position. Therefore we spend less time on realignment of the six beams. Moreover the number of optical elements is reduced by replacing them with the optical fibers. This reduces the complexity of the setup as well. The two beams (MOT and re-pumper) have been overlapped and adapted to the spatial mode of the optical fiber (Fig. 3.14). We used an inverse injection to the output of the optical fiber and we looked at the spatial mode of the out-coming light. Next, by means of a telescope, we adapted the spatial profile of the MOT and re-pumper beams to that out-coming spatial mode. Then injection into the fiber has been optimized. The injection efficiency for the MOT beam is about 40% and

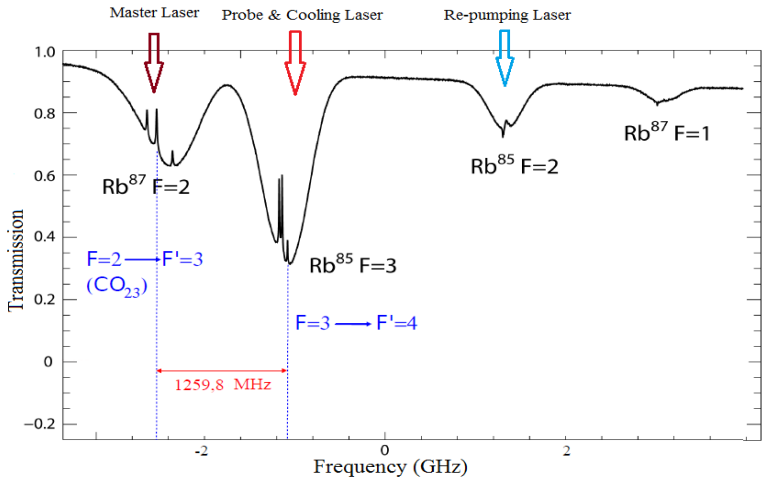

Figure 3.12 – D2 transition saturated absorption spectrum of the rubidium vapor. The frequency of master laser is indicated and the frequency shift that is needed for the cycling cooling transition of ^{85}Rb MOT [105].

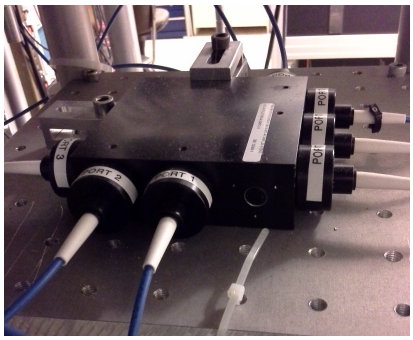

Figure 3.13 – Image of our one to six fiber beam splitter.

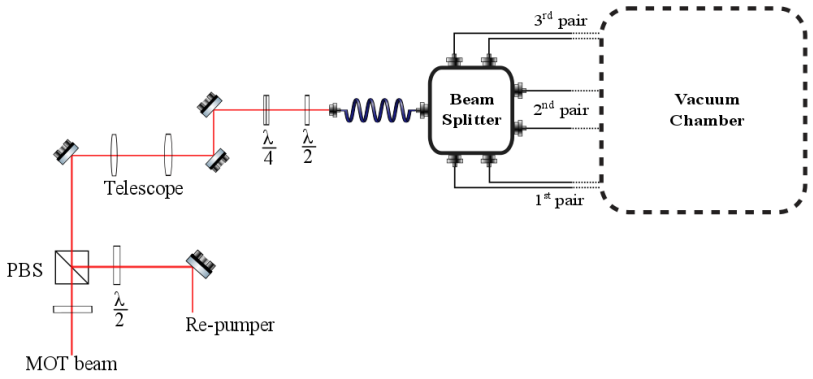

Figure 3.14 – Combination of the cooling and re-pumper beam for the injection into the optical fiber. Note that, because of the polarized beam splitter (PBS), the polarization of the MOT beam and the re-pumper is perpendicular at the fiber injection.

for the re-pumping beam is about 60%. Here the efficiency is relatively low because of the poor spatial profile of the beam at the output of the tapered amplifier. Moreover we make the beams linearly polarized and for the cooling beams we set the polarization on the optical axis of the fiber to have a stable and linear polarization at the output. The polarization of re-pumper beam is perpendicular to the cooling laser due to the PBS used to overlap the two beams before fiber injection (Fig. 3.14). At the fiber injection the MOT beam and the re-pumper have perpendicular polarizations.

Previously dividing the cooling and re-pumper beams had been done by polarizer beam-splitters (PBS). Now in order to provide six perpendicular trapping beams, a fibered beam-splitter from OZ optics [106] (Fig. 3.13) is employed. This beam-splitter equally splits ($\approx \pm 10\%$) the incident beam into six and preserves the polarization. At the output of each fiber, the polarization is readjusted by a quarter-wave-plate to make appropriate circular polarization (σ^+ and σ^-) for the trapping beams. The cooling and repumping beams are collimated by using large lenses (100 mm diameter and 300 mm focal length) at each fiber output, which results in collimated 30 mm waist size for each beam (Fig. 3.15). In order to balance the optical power of counter-propagating pairs of beams along x, y and z directions we paired up the fibers with closest match. So we have (11.73, 12.29 mW) along x, (12.79, 14.21 mW) along y, and (10.84, 10.86 mW) along z-axis.

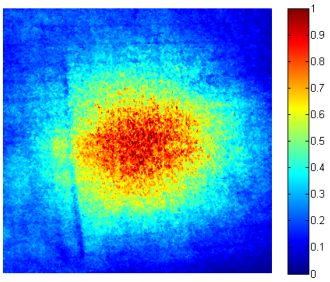

(a)

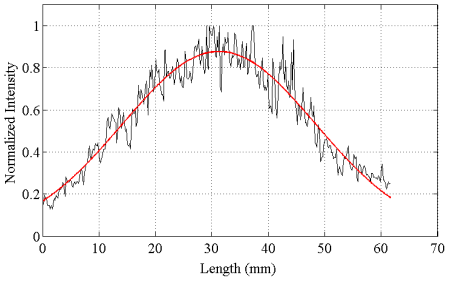

(b)

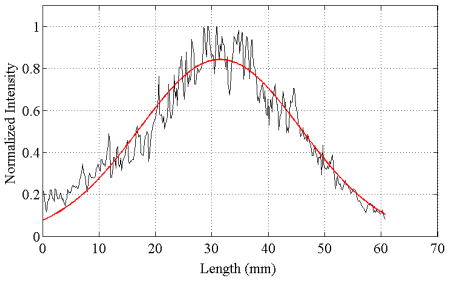

(c)

Figure 3.15 – (a) The intensity profile of a trapping beam just before propagating through the vacuum chamber. The beam was intercepted by a white paper and the image of it was taken by a camera. Calibration of this camera gives 0.173 mm for each pixel size of the image and this image contains 360×360 pixels. (b) One dimensional spatial profile of the beam along x-axis and (c) y-axis and their Gaussian fits, which show a waist size (width at $1/e^2$) of ≈ 29 mm and ≈ 34 mm respectively.

3.4 Dark MOT

Trapping atoms in a MOT basically leads to a dilute atomic cloud with an atom density of typically a few 10^{10} atoms/cm^3 and a size of $\sim 1\,$cm. The optical thickness b_0 of such a cloud would be around a few 10s. This steady-state density is a consequence of the balance between the trapping force, i.e. spring constant, and the repulsive force due to the effective atom-atom repulsive interactions due to multiple scattering. For many experiments and measurements, it is important to increase the density and b_0. In a standard MOT atom number density n is limited mainly for two reasons. First, absorption of the trapping beams and shadow effect. This means that the trapping beams can not penetrate a dense cloud and thus the cooling and trapping process is less efficient. Second, the repulsive interaction between atoms, which is related to the scattering of the trapping light, forces the atoms apart through the radiation pressure processes and thereby both size and temperature of the cloud increases [107]. A number of methods have been proposed to overcome this constraint. In compressed MOT (CMOT) for example, an immediate increase in the gradient magnetic field $\bigtriangledown B$ can enhance the density by almost one order of magnitude, but at the cost of heating up the cloud [108, 109]. In dark MOT (DMOT) on the other hand, atoms in the trap are allowed to dissipate into an atomic state which does not couple to the trapping light, in our case $|F = 2\rangle$. The atom-atom interaction thus decreases and density increases.

DMOT compression can be carried out in two different regimes of spatial dark spot by masking the center of re-pumper beams [110, 111] and dynamical DMOT by attenuating the re-pumper intensity, typically by a factor of 100, for a short time, typically tens of milliseconds, after the loading of the MOT [112, 109].

In our cold-atom experiment a dynamical dark MOT is applied (with experimental parameters mentioned in time unit) to compress MOT and to enhance the density up to $10^{12}\,$atoms.cm^{-3} and optical thickness b_0 up to ~ 150. In Fig. 3.16 an absorption image of a small MOT is depicted before and after compression by a DMOT process. Attenuation of the re-pumper intensity is done by changing the amplitude of modulation produced by a VCO and fed into an AOM. The calibration of the first-order diffracted intensity of that AOM as a function of the VCO modulation amplitude is demonstrated in Fig. 3.17. This amplitude is controlled by an interface card which is connected to a computer. Therefore with this calibration we can adjust the intensity of the re-pumper to a certain portion and certain interval at a desired time. By measuring the optical thickness b_0 and density n corresponding to different values of re-pumper intensity and DMOT interval, an optimum situation can be chosen (Fig. 3.18). In our experiment we reduce I_{rep} to 2% of its initial intensity within 35 ms (see the DMOT time sequence in Fig. 3.21).

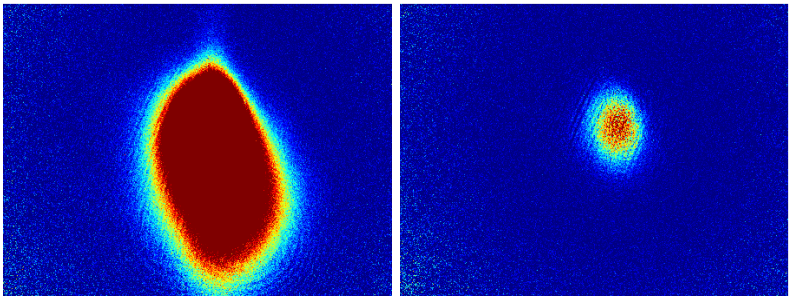

(a) (b)

Figure 3.16 – Absorption image of (a) a standard MOT realization ($\delta_{img} = 0\,\Gamma$, $b_0 \approx 5$) and (b) after applying the dark MOT compression to it ($\delta_{img} = -2\,\Gamma$, $b_0 = 22$). Please note that in order to fit the image of MOT into the frame, a short loading time was used. In practice we are able to produce bigger and optically thicker MOT and dark MOT (up to $b_0 = 150$). The size of standard MOT compressed from 2.9 mm to 0.9 mm for dark MOT.

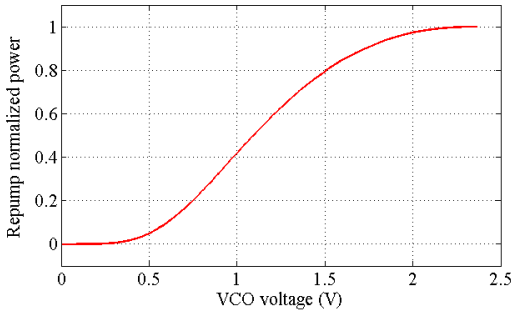

Figure 3.17 – Calibration of an AOM by changing the voltage input of the VCO which feeds that AOM, in order to vary the intensity of the diffracted beam. The voltage controls the amplitude of the VCO modulation and hence it changes the efficiency of the diffraction in the AOM. This calibration has been normalized to the maximum intensity of the diffracted beam.

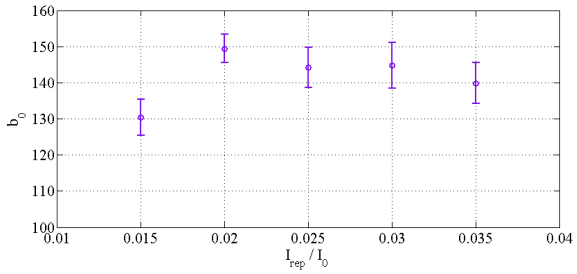

(a)

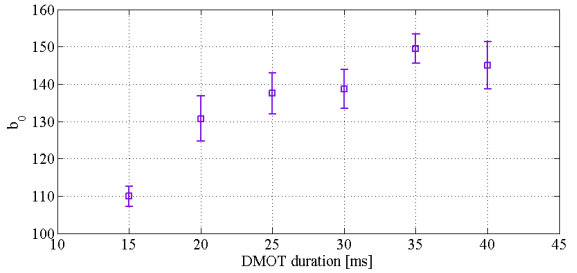

(b)

Figure 3.18 – Optimizing the re-pumper intensity and DMOT duration in order to have maximum optical thickness. (a) b_0 as a function of the reduced re-pumper intensity during 35 ms. (b) b_0 as a function of DMOT duration with a reduced re-pumper intensity to 2% of its initial value. The total initial re-pumper intensity was $\approx$ 5 mW. Each point is the average of 10 realizations and the errorbars are the standard deviation of them.

3.5 Optical molasses

The Doppler cooling process due to the radiation pressure in the absence of magnetic field is known as optical molasses because of the viscous nature of this process. This phenomena for the first time was experimentally observed at Bell laboratories [113]. Indeed that was a revolutionary step towards cold and ultra cold-atom experiments.

It is known that the temperature of the atoms depends strongly on the detuning of the cooling beams in this phase. A larger red detuning leads to a lower temperature. However there is a lower limit to the minimum temperature which one can reach by this technique [114, 115, 116]. In our experiment we use this time period basically to vary the temperature. First the MOT is loaded in the trap, then dark MOT is applied to compress the MOT, and finally the magnetic gradient is switched off to perform the optical molasses phase. In fact the spatial confinement of the MOT is suppressed when switching the magnetic gradient off. The detuning of the cooling beams changes to a desired value (δ_{Mol}) which depends on the target temperature.

In the laboratory, there are sources such as computer displays, electronics, vacuum pump, wires and the earth which generate unwanted magnetic fields. Optical molasses are very sensitive to stray magnetic fields. If there is a magnetic field at the position of the MOT, during the molasses period, the cloud starts to move in a way which depends on the direction of that magnetic field. By installing three pairs of coils in Helmholtz configuration and adjusting the current in each coil we can compensate stray magnetic fields along different directions. Therefore an application of the optical molasses is to adjust those bias magnetic fields in a configuration that the atomic cloud expands almost homogeneously at its position during the molasses period.

3.6 The characterization of MOT

In this section some common experimental methods will be introduced for measuring different parameters in order to characterize the MOT.

3.6.1 Transmission spectra

The aim of the transmission spectra method is mainly to measure the optical thickness. In this method a weak probe beam (typically around $I_{sat}/10$ with $I_{sat} = 1.67mW.cm^{-2}$) is transmitted through the MOT while the frequency of that probe is scanned through the atomic resonance. The normalized transmission, T, is defined as the ratio between the transmitted intensity and the incident intensity ($T = I_T/I_I$) and is a function of the probe detuning. For a non-saturating probe beam, the transmission can be written as

$$T(\delta) = \frac{I_T}{I_I} = e^{-b(\delta)}. \tag{3.8}$$

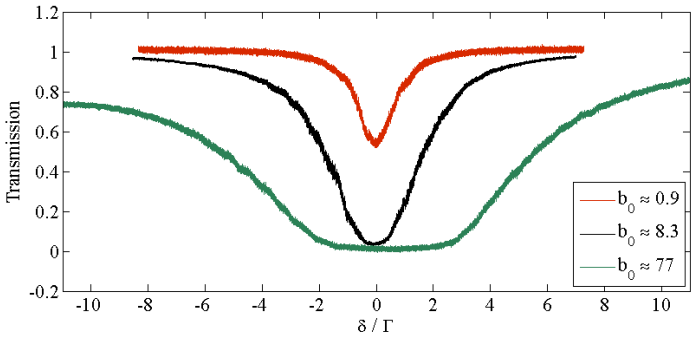

Figure 3.19 – Experimental transmission curves for three different $b_0 = 0.9, 8.3, 77$.

$b(\delta)$ is known as optical depth or optical thickness, and for a two-level system it is a Lorentzian function of the detuning

$$b(\delta) = \frac{b_0}{1 + 4\frac{\delta^2}{\Gamma^2}}, \tag{3.9}$$

where b_0 is the on-resonance optical thickness, and $\Gamma = 6.06\,\text{MHz}$ is the natural linewidth of the rubidium atoms. Considering Eq. 3.8 one can fit the measured $T(\delta)$ spectrum and extract the value of b_0, one of the characteristic parameters of the MOT. With a large cloud of cold atoms, the on-resonance optical thickness b_0 is large and practically nothing is transmitted at line center. Then, the full width at half-maximum (FWHM) of the transmission spectra is approximately proportional to $\sqrt{b_0}$ (Fig. 3.19).

A useful and interesting situation is to study the transmission of a probe beam through an optically thin sample ($b_0 \ll 1$). First of all one can easily check if the frequency of the laser is well calibrated with the atomic resonance in the transmission curve. This is very important for the experiment because we use the detuning of the laser from the atomic resonance to calculate and measure quantities such as the number of atoms. Thus any discrepancy in the actual detuning and frequency calibration of the laser leads to errors in our measurements.

We can also use optical thickness spectra to quantify the laser linewidth. Taking the probe laser spectrum $\mathcal{S}(\nu)$ into account, the transmission is given by

$$T(\delta) = \int_{-\infty}^{\infty} \mathcal{S}(\nu) \exp \frac{b_0}{1 + 4(\frac{\delta+\nu}{\Gamma})^2} d\nu. \tag{3.10}$$

The transmission spectrum therefore is a result of the convolution between $\exp(-b(\delta))$ and the laser spectrum $\mathcal{S}(\nu)$. Thus by deconvolution of the

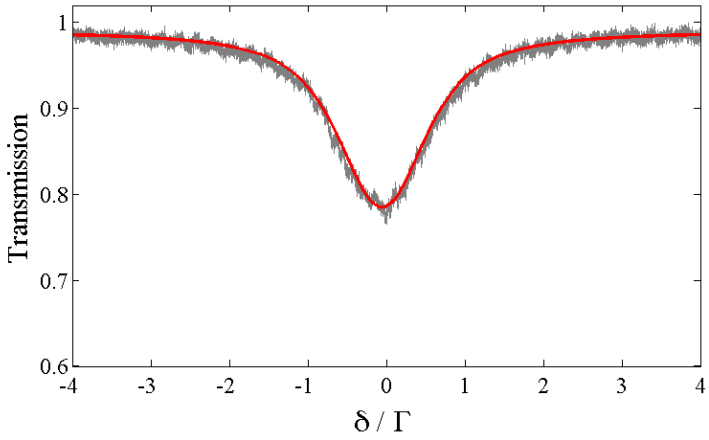

Figure 3.20 – Measured transmission (light gray) of a probe through a MOT with small optical thickness, $b_0 = 0.27$. Applying a convolution fit based on Eq. 3.10 we estimated 3.6 MHz for the probe laser linewidth.

transmission spectrum one can estimate the laser linewidth. Applying this method we verified a laser linewidth of 3.63 MHz (Fig. 3.20). In a special case of very small optical thickness ($b_0 \ll 1$), $\exp(-b(\delta))$ is expanded to the lowest order and replacing in Eq. 3.10 leads to

$$T(\delta) = ((1 - b) * \mathcal{S})\,(\delta), \tag{3.11}$$

where $*$ means the convolution operation. Assuming a Gaussian optical spectrum for the laser, Eq. 3.11 results in a Voigt spectrum.

3.6.2 Absorption imaging

Absorption imaging is an alternative technique to characterize the number of atoms N_{at} in the MOT, the size of the cloud σ, and the optical thickness b. In this method, a weak and large waist size ($\approx$ 10 mm) laser beam is employed as the probe beam. The transmission of this probe beam depends on its relative frequency to the atomic resonance, as well as on the number density of the atoms. The transmission of light through a medium follows the Beer-Lambert law

$$I_T(x, y, z) = I_I(x, y, z)\ exp\Big(- \sigma(\delta) \int_{-\infty}^{z} n(x, y, z')dz'\Big), \tag{3.12}$$

where $n(x, y, z')$ is the atom number density, z' is the direction of light propagation, and $\sigma(\delta)$ is scattering cross-section and defined as

$$\sigma(\delta) = g_f \frac{3\lambda^2/2\pi}{1 + 4\frac{\delta^2}{\Gamma^2}}, \tag{3.13}$$

and $\sigma_0 = g_f 3\lambda^2/2\pi$ accounts for on-resonant atomic scattering cross-section and g_f represents the degeneracy of the atomic levels. For $F = 3 \rightarrow F' = 4$ transition, assuming all the atoms are in a statistical mixture of the Zeeman states, one can write [117]

$$g_f = \frac{1}{3}\frac{2F' + 1}{(2F + 1)} = \frac{3}{7}. \tag{3.14}$$

Considering Eq. 3.8, the optical thickness can be written as

$$b(\delta) = \sigma(\delta) \int_{-\infty}^{z} n(x, y, z')dz'. \tag{3.15}$$

The atomic cloud is supposed to have a Gaussian spatial distribution with r.m.s. sizes σ_x, σ_y, and σ_z along each dimension. So the total number of atoms N_{at} is

$$N_{at} = (2\pi)^{3/2}\sigma_x\sigma_y\sigma_z n_0 \tag{3.16}$$

where n_0 is the peak of atom number density and in view of the Eq. 3.15 is given (Ref. [14])

$$n_0 = \frac{b_0}{\sqrt{2\pi}\sigma_z\sigma_0} \tag{3.17}$$

Now Eq. 3.16 can be written as

$$N_{at} = (2\pi)\frac{\sigma_x\sigma_y b_0}{\sigma_0} \tag{3.18}$$

Another way to measure the total number of atoms is to measure first the atom number density profile

$$\int_{-\infty}^{z} n(x, y, z')dz' = -\frac{1}{\sigma(\delta)} ln\Big(\frac{I(x, y, z)}{I_I(x, y, z)}\Big) \tag{3.19}$$

and then by integration of Eq. 3.19 over all the CCD pixels, the total number of atoms in the MOT is computed

$$N_{at} = -\frac{A}{\sigma(\delta)} \sum_{i,j} ln\Big[\frac{(I_T)_{ij}}{(I_I)_{ij}}\Big], \tag{3.20}$$

where A is the apparent area of each pixel. Pixels area depends on the optical magnification (M) and is measured with calibration of the CCD by

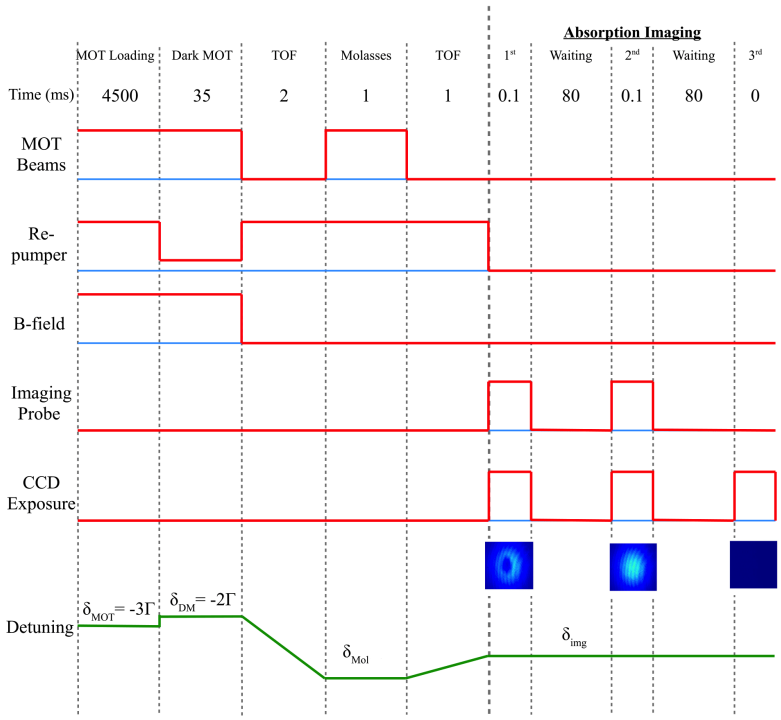

Figure 3.21 – Time sequence of a typical absorption imaging process. In this sequence, first the MOT is loaded, then compressed to achieve higher optical thickness, then by applying molasses phase, the temperature is modified, and finally the absorption image is taken.

capturing an image of a ruler and taking the real pixel size (4.4 μm) into account.We measured ($M \approx 2.6$) and the image pixel size of 11.4 μm.

Experimentally an absorption image is obtained by recording the shadow of a MOT on a CCD camera (Pointgray model gras-20S4M-C) when a laser beam is transmitted through it. Next it is compared to the image of the incident beam when the atomic cloud disappeared completely. Finally a dark image is subtracted from both images to get rid of any offset. The exposure time is typically 100 μs to avoid any changes in the MOT properties during the first image capture. The typical time sequence of the absorption imaging is demonstrated in Fig. 3.21. The image processing and its analysis are being done by a Matlab routine, which provides us with a real time analysis and calculation of all the MOT parameters from each image. The calibration of apparent pixel size and the detuning δ of the imaging probe are given to this routine as the input values for computations of all the desired parameters. Therefore the precision of this technique depends on the calibration of the CCD pixel size and also depends on how accurate the real frequency of the probe has been adjusted. Any defect in these input parameters causes error in the computations. This emphasizes the importance of calibration of the laser frequency. By applying a Gaussian fit to the image and extracting Gaussian width (σ_x and σ_y), the size of the cloud is measured. Also the center of the image of MOT, where the transmission is minimum, measures $b(\delta)$ and consequently b_0 considering Eq. 3.9. Now from Eq. 3.18 and then Eq. 3.16 we obtain N_{at} and n_0. This Matlab routine also calculates N_{at} from Eq. 3.20.

3.6.3 Time of flight

By switching off the MOT, atoms in the cloud start to make a ballistic flight and as a consequence the cloud expands due to its temperature while falling due to gravity. This process is known as time of flight (TOF). This experimental phase is usually employed before taking data to ensure that all the components of the trap switch completely off (specially the magnetic gradient field decays to zero with 2% error (which in our experiment is equivalent to $\pm 0.5 Gauss$) in a certain time as it is shown in the Fig. 3.24). Moreover preparing the right frequency for the probe beam, which is done by the offset lock just as for the trapping beams, takes few hundred microseconds (Fig. 3.10). In our configuration a TOF of $1ms$ usually guarantees an appropriate situation.

Another important application of the TOF is to measure the temperature of the cloud of cold atoms as explained in the following section.

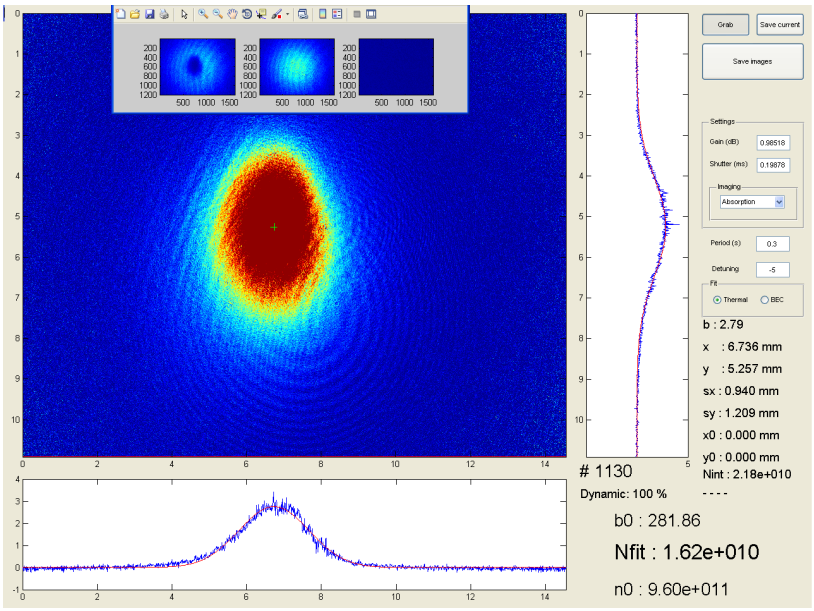

Figure 3.22 – A sample of absorption image of the MOT and the Matlab routine which is used to measure size, optical thickness, total number of atoms and atom number density.

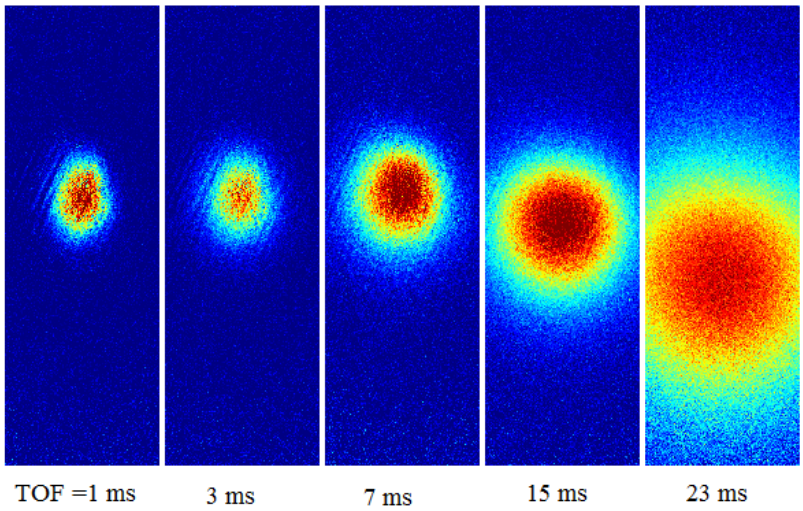

Figure 3.23 – Absorption images of dark MOT taken after different TOF durations. δ_{img} was chosen to keep $b(\delta) \simeq 1$, ($\delta_{img} = -3, -2.5, -1.8, -1, -0.3\,\Gamma$ from left to right respectively). From this time-lapse one can estimate the gravity of Earth g.

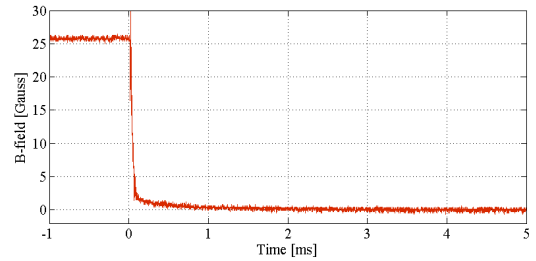

(a)

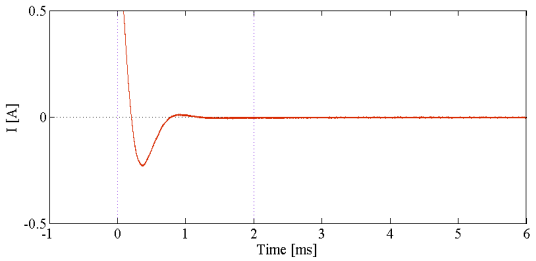

(b)

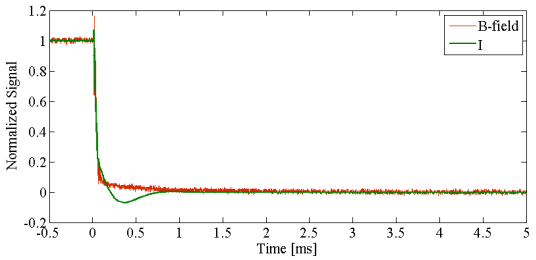

(c)

Figure 3.24 – Decay of the magnetic field measured by a Gauss-meter (a) and the current in the coils (b) after switching off the magnetic gradient. The normalized decay signals of both magnetic field and the current are compared (c). It is realized from the figure that an approximately $2ms$ delay time is needed for the I and B-field to get to zero with 2% error.

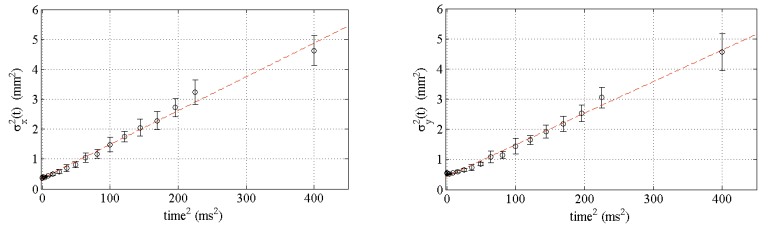

(a) (b)

Figure 3.25 – Time of flight measurements of a dark MOT with $N_{at} \approx 10^{10}$ and $b_0 \approx 100$, (a) in the x-dimension and (b) in the y-dimension. The slope of each plot is a measure of $\frac{k_B T}{m}$. Considering $\frac{k_B}{m} = 97.9188 \frac{\mathrm{m}^2}{\mathrm{s}^2 \mathrm{K}}$ the above plots show a temperature of about $110\,\mu$K for the MOT.

3.6.4 Temperature measurement

The equation of motion of the particles during TOF can be written as

$$\vec{r}(t) = \vec{r}(0) + \vec{v}(0)t - \frac{1}{2} g t^2 \vec{e_z}, \tag{3.21}$$

where g is the gravitational acceleration along $\vec{e_z}$. The last term in Eq. 3.21 can be ignored in very short TOF. By averaging over the atomic distribution the square of this equation of motion one obtains

$$< r(t)^2 >=< r(0)^2 > + < v^2 > t^2 + 2 < \vec{r}(0).\vec{v}(0) > t. \tag{3.22}$$

Assuming that there is no correlation between the velocity and initial position of particles, the term $r(\vec{t}).v(\vec{t})$ averages to zero. Regarding the spatial Gaussian density profile of the MOT, the r.m.s. size ($\sigma(t)$) of the cloud can be taken and also $< v^2 >= \frac{k_B T}{M}$, we obtain

$$\sigma(t) = \sqrt{\frac{kT}{m} t^2 + \sigma_{ini}^2}. \tag{3.23}$$

Thus, in the time of flight (TOF) experiment, by taking several pictures at different TOF and measuring the cloud size, one can estimate the temperature (Fig. 3.25).

3.6.5 Controlling optical thickness

Decreasing b_0 is very straightforward. The maximum b_0 is obtained by compressing the MOT, and then by applying a TOF period the cloud expands whereas the temperature does not change. Although there are some losses of the rubidium atoms in the MOT due to the residual gases collision, it is

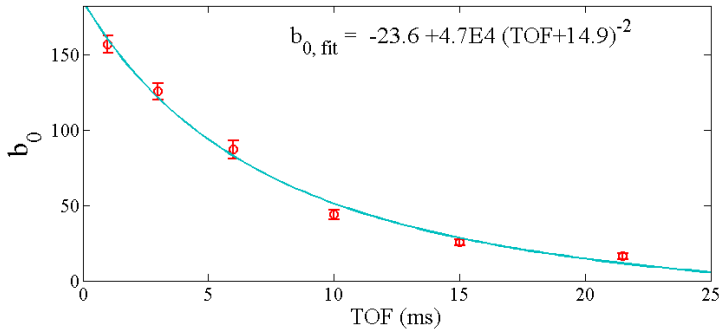

Figure 3.26 – b_0 as a function of TOF duration. The errors correspond to the statistical variations in the measured optical thicknesses. A fit, based on the relation $b_0 \propto N/\sigma^2(t)$, is applied (blue line) to estimate the optical thickness at different TOF.

usually negligible during the TOF. Therefore by increasing the TOF duration, b_0 decreases (in our experiment we are able to change it from almost 160 to 10 (Fig. 3.26)) while the other parameters, such as the atom number and the temperature, are reasonably unchanged, except, of course, the size and the density of the cloud.

3.7 Vacuum pressure

The MOT is loaded from the background room-temperature ^{85}Rb atoms in a cubic silica cell with a size of 10 cm [118]. However to realize a MOT, a very low pressure environment is needed. This low pressure is achieved in our experiment by an ultra high vacuum (UHV) ionic pump (Varian, 20 Liter/sec) which provides a vacuum of 10^{-8} mbar in the cell. Indeed the vacuum pressure P_{vac} plays an important role in realization and improvement of the MOT.

The MOT is basically loaded at a certain rate, $\mathcal{L}$ (atoms/sec), which is in principle proportional to the partial pressure of Rb-atoms, P_{Rb}. On the other hand collisions between the background room-temperature gases (including both rubidium atoms and residual gases) and trapped atoms is one of the loss factors. The impact of a room-temperature atom can transfer enough energy to a cold trapped Rb atom such that the atom escapes from the trap. This loss rate is represented by γ and is proportional to the total vacuum pressure, including both partial pressure of residual gas, P_{res}, and P_{Rb} ($\gamma \propto P_{Rb} + P_{res}$). Another loss factor is the collision between trapped atoms, which is known as cold collision. This type of loss accounts for two-

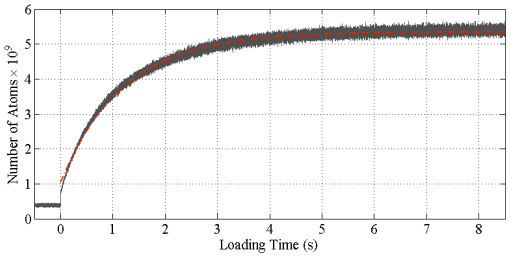

Figure 3.27 – Fluorescence signal representing the loading of a MOT. The detuning of the cooling beam is $\delta_{MOT} = -3\,\Gamma$. An exponential fit (Eq. 3.25) gives $\gamma^{-1} = 1.2\,\mathrm{s}$ (red dashed line).

body losses, i.e. light assisted collisions between cold atoms. Theoretically, the time evolution of the total number of trapped atoms, N, is written as [119]

$$\frac{dN}{dt} = \mathcal{L} - \gamma.N - \beta. \int n^2(r,t) d^3r, \tag{3.24}$$

where $\mathcal{L}$ is the loading rate, $n(r,t)$ is the atomic density, γ is the loss rate due to the room-temperature collisions, and the quadratic term $\beta.n^2$ describes losses due to the cold collisions. In our experiment, the typical atomic density of MOT (without any compression) is about $\sim 10^{10} cm^{-3}$ and $\beta = 2.10^{-12} cm^3.s^{-1}$ [120]. Therefore $\beta.n \ll \gamma$, or in other words the cold collision is negligible compared to the background gas loss rate. A general solution of Eq. 3.24 in this regime is given by

$$N(t) = N_\infty (1 - e^{-\gamma t}) \tag{3.25}$$

with boundary conditions of $N(t=0) = 0$ and $N_\infty = \mathcal{L}/\gamma$. In a limit that $P_{res} \ll P_{Rb}$, the stationary state number of atoms, N_∞ is independent from the background gas pressure. However γ depends on the pressure. Therefore the time constant of loading of a MOT, γ, can be employed in this regime as a criterion for estimation of P_{Rb} in the vacuum cell. This can be done by collecting the fluorescence of the MOT on a photo-detector while it is loaded (Fig. 3.27). When the loading time, $1/\gamma$, is too long one can open the valve of the Rb reservoir, for instance, to increase P_{Rb}. This valve connects a small reservoir of Rb metal, to the vacuum chamber (see Fig. 3.28.) Therefore by opening it, the Rb pressure increases in the vacuum chamber.

One possibility is to study P_{Rb} by using transmission measurements. Considering Eq. 3.12, and assuming that Rb pressure, Rb atom density and ambient temperature are stationary and homogeneous, transmission of

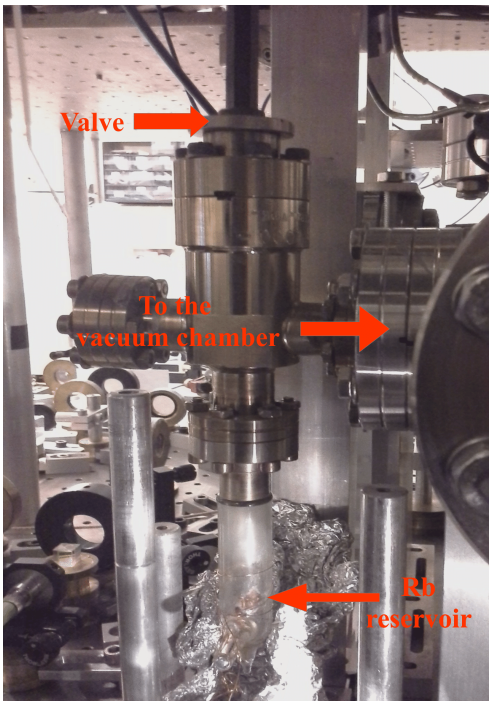

Figure 3.28 – The image of the valve which connects the Rb reservoir to the vacuum chamber.

a laser beam through the vacuum cell and a reference cell is written as

$$T_{cell} = exp(-n_{cell}\sigma(\delta)L_{cell}) \qquad (3.26)$$
$$T_{ref} = exp(-n_{ref}\sigma(\delta)L_{ref})$$

The estimated Rb pressure P_{ref} in a reference Rb cell was given in Ref. [101] and is about 2.66×10^{-7} mbar at the lab temperature ($\sim 22°$C). Since at low pressure the ideal gas law is applicable, one can calculate the pressure as a linear function of atomic density and temperature Θ.

$$P = nR\Theta \qquad (3.27)$$

where R is the universal gas constant, $R = 8.314 J.K^{-1}.mol^{-1}$. Taking the transmission spectra from both reference cell and vacuum chamber simultaneously and using Eqs. 3.26 and 3.27 leads us to

$$P_{cell} = \frac{ln(T_{cell})}{ln(T_{ref})}\frac{L_{ref}}{L_{cell}}P_{ref} \qquad (3.28)$$

Regarding $L_{ref} = 45$ mm and $L_{cell} = 100$ mm, Fig. 3.29 shows $P_{Rb} \sim 10^{-7}$ mbar in the vacuum cell which is relatively high for making a MOT. When I started my PhD, the ionic pump had just been replaced. However after replacement, the pressure in the vacuum chamber did not decrease enough and the quality of the MOT was not satisfactory. However this result raises an interesting idea, since we have already obtained a MOT in this pressure, almost the same as P_{ref}: is it possible to get rid of vacuum pumps and demonstrate MOT in a standard spectroscopy cell, which could decrease the size and complexity of the experiment a lot? As a result the beginning of my job was to find and solve this vacuum pressure problem. Finally it turned out that the polarity of the power supply of the ionic pump was reversed. So after applying the correct polarity, the vacuum pressure dropped to almost 10^{-8} mbar, and as a consequence the loading time of the MOT increased and the loss rate due to the background collisions decreased. Therefore the MOT got bigger in size and number of atoms and also the maximum optical thickness increased. In the Table 3.1 the quality of the MOT before and after changing the polarity of the power supply of the ionic pump is summarized.

3.8 Conclusion

As a conclusion we can perform MOT at INLN with approximately 10^{10} atoms of ^{85}Rb and a size of ~ 1 mm after a short compression period. The frequency of the cooling laser is stabilized by an offset lock-in. This lock provides us with a very large frequency scanning range (~ 500 MHz), which

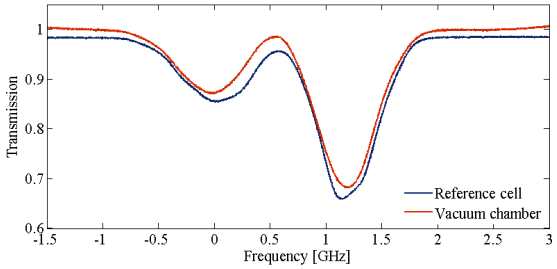

(a)

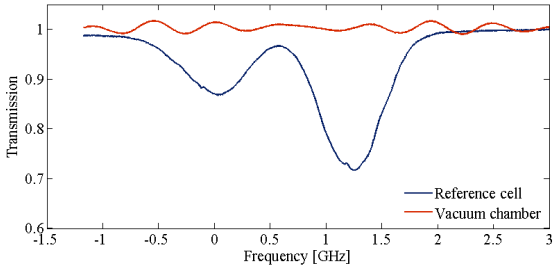

(b)

Figure 3.29 – Rubidium transmission spectra from a reference cell and the vacuum chamber. Eq. 3.28, (a) shows a pressure of $\approx 10^{-7}$ mbar, while after reducing the pressure to 10^{-8} mbar in (b) the absorption signal in the vacuum cell was not strong enough so that we could not use Eq. 3.28 to estimate pressure.

Table 3.1 – Comparing different MOT properties before and after solving the problem in the performance of the ionic pump. After solving this problem we achieved lower vacuum pressure (10^{-8} mbar).

Vacuum pressure	$\sim 10^{-7}$ **mbar**	$\sim 10^{-8}$ **mbar**
max b_0	20	150
Loading time	~ 60 ms	~ 1 s
Temperature	$\sim 40\,\mu$K	$\sim 120\,\mu$K
MOT size	0.2 mm	0.8 mm
Number of trapped atoms	$10^7 - 10^8$	$10^9 - 10^{10}$
Atomic density	$\sim 10^{12}$ cm^{-3}	$\sim 10^{12}$ cm^{-3}

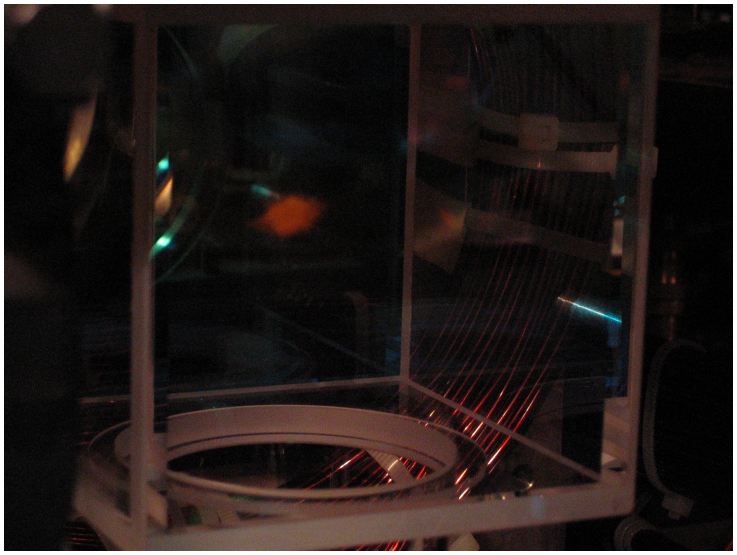

Figure 3.30 – A snapshot of the standard MOT produced in the vacuum chamber (with a length 10 cm) in our experiment.

is very advantageous for the random laser experiment. For our future experiments it will be critical to be able to control and vary the physical parameters of the MOT individually in a skillful manner. For instance by TOF technique, we can manipulate the optical thickness of the MOT in the range of $\sim 10-100$ while N_{at} and temperature are kept constant. The temperature of the MOT can be also managed between $150-500\,\mu$K. Finally the reproducibility of the MOT properties over several weeks is satisfactory.

Chapter 4

Noise Spectroscopy Of Cold Atoms

Table 4.1 – Table of notation used in the following chapter.

δ	Laser detuning from the atomic resonance
Γ	Natural linewidth of the rubidium atom $\Gamma = 6.06\,\mathrm{MHz}$
ν	Optical frequency
ν_{L}	Laser frequency
$\Delta\nu_{\mathrm{L}}$	Laser linewidth
$\Delta\nu_{BN}$	Beat-note linewidth
$\Delta\nu_c$	Fabry-Perot cavity linewidth
$\Delta\nu_{FSR}$	Free spectral range
$\mathcal{F}$	Cavity finesse
f_{n}	Fourier frequency
$S_{SN}(f_{\mathrm{n}})$	Shot noise power spectral density (PSD)
$G(f_{\mathrm{n}})$	Photodiode gain curve
S_P	Laser intensity noise PSD
RIN	Relative intensity noise PSD
S_E	Optical spectrum
$S_{\nu_{\mathrm{L}}}$	Laser frequency noise PSD
S_ϕ	Laser phase noise PSD
S_T	Transmission noise PSD
S_{ν_T}	Converted frequency noise to intensity noise due to the frequency discriminator
I_i	Incident intensity
I_T	Transmitted intensity
T_c	Fabry-Perot cavity transmission
T_a	Atomic transmission
D	$dT_a/d\delta$
ϕ_{m}	Phase shift
α_{m}	Electric field absorption

Measuring the light fluctuations and correlations after their interaction with cold atomic samples may provide information on the atomic sample such as motion [16, 121, 122] and could be used to characterize more subtle effects due to interference effects in multiple scattering [123]. Such measurements could in particular be implemented to study the difference between light scattered in passive cold atomic clouds and light emitted by cold atom random lasers [4], thus providing a direct signature of this phenomenon.

However, in this kind of experiments, the intrinsic noise of the involved lasers may contribute and even mask the fluctuations under study. One particular problem is the frequency or phase noise of the laser, which is converted to intensity noise through the atomic resonance in a nontrivial way.

In this chapter, we study this conversion in detail, by addressing a particular configuration, in which intensity noise measurements are performed on a laser beam transmitted through a sample of laser-cooled atoms. This transmission geometry is relevant to investigate different properties, such as the reduction of the noise below the shot-noise level (squeezing) [124, 125], the extra noise due to the atomic internal structure via Raman scattering [126], or two-photon optical nonlinearity [127]. This configuration also allows us to use a simple model of light-atom interaction, in which the atomic cloud is described by a complex index of refraction.

This study in the forward direction might become interesting to investigate different properties, such as cooperative effects [128] or the influence of the atoms via their motion [129] or via quantum effects due to saturation or atomic internal structure [126] or the spin squeezing in a quantum nondemolition measurements [130]. But, before turning to these more involved regimes, one first needs to have a precise description of the noise features in the simplest model where the atomic cloud can be described by an index of refraction and thus by a mean field approach. The interaction of the laser intrinsic noise with the atoms gives rise to the noise spectroscopy. In this technique, one can resolve the atomic spectra without scanning the laser frequency.

4.1 Laser characterizations

Characterizing laser noise is a vital issue in many experiments. High precision optical measurements, e.g. in frequency metrology, or in high resolution spectroscopy or interferometry, require low laser intensity and phase noise [131, 132, 133]. In optical fiber communication systems also, one main limitation in the data transmission rate comes from the noise of lasers and amplifiers [134]. In our experiment, the transmitted light through cold atoms contains some information imprinted by the atoms and at the same time infected by the intrinsic noises of the incident laser. Thus in order to dis-

tinguish those interesting atomic information, it is first important to characterize carefully the laser noise. Generally noise in a continuous wave laser can be classified as

- amplitude/intensity noise, which is usually low for a laser working far above its threshold
- frequency noise,
- phase noise, which limits the laser temporal coherence.

Generally a laser electric field is described by

$$E(t) = E_0(t)e^{i[\omega_L t+\phi(t)]}, \tag{4.1}$$

where $E_0(t)$ and $\phi(t)$ are time-dependent amplitude and phase of the electric field. The instantaneous frequency of the laser is given by

$$\omega(t) = \omega_L + \frac{d\phi}{dt} = \omega_L + \Delta\omega(t). \tag{4.2}$$

In this picture ω_L would be constant and $d\phi/dt$ or $\Delta\omega(t)$ is associated to the frequency noise. Therefore the frequency and phase noises are related. In addition, two types of origins are considered for the laser noise

- **quantum noise**, in particular associated with the spontaneous emission in the gain medium and the gain saturation.
- **technical or classical noise**, arising for instance from temperature fluctuations, electronic noise of the laser driver, the mechanical noises of the laser cavity.

In this section, by using some standard and common techniques, we characterize the noise of a DFB laser which is amplified by a tapered amplifier. The laser is frequency locked by an offset lock system. We also report the effect of some technical sources of noise on the line shape and the frequency noise of our laser. To fully characterize the linewidth of our DFB laser by the beat-note measurements, two frequency locked extended cavity lasers also were used. More details about these lasers will be given in Sec. 4.1.2.

4.1.1 Laser amplitude/intensity noise

The intensity noise of a laser is measured by directly shining that laser to a photodiode. The power spectral density (PSD) of the output photocurrent then can give the intensity fluctuations. However to obtain intensity noise, one needs first to characterize the response or the gain curve of the detection system (Fig. 4.1).

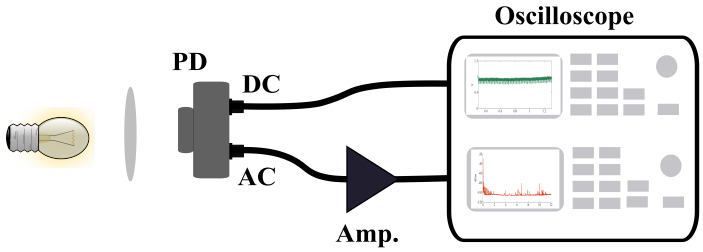

Figure 4.1 – Schematic of the gain curve measurement.

Detection gain curve

For this measurement we used a home-made trans-impedance photodiode. This type of photodiode has two outputs. One has a very low bandwidth which can record a DC signal. After calibration of this output channel, we used it as a powermeter. The second output corresponds to a band-pass filter which is convenient for noise measurements and is referred as the AC output. A low noise amplifier (Minicircuit model:ZFL-500ln, +30 dBm) is also used on this photodiode output to enhance the final signal. Then the PSD of this amplified AC signal is observed by an oscilloscope working in the fast Fourier transform (FFT) mode. The gain curve of the detection system (AC output with amplifier) was taken by shining a white noise source at the detector. The white noise is flat and frequency independent. We used a battery powered incandescent light bulb, which is supposed to be shot-noise limited, to produce white noise. The PSD of the amplified AC output S_{white} was recorded after 100 cycles of averaging. The incident optical power P_{opt} was taken also thanks to the DC calibration of the photodiode. In order to check that our measurements are not limited by the electronic noise, the PSD of background is recorded with the same number of averages. According to the incident optical power, one can calculate the expected 1-sided shot-noise PSD

$$S_{SN} = 2\frac{hc}{\lambda}\eta \times \overline{P}_{opt}, \tag{4.3}$$

where h is the Planck's constant, λ is the average wavelength of the detected light due to the detector working range, and η is the quantum efficiency of the detector. S_{SN} is independent on the Fourier frequency and is a constant number. Now the gain curve $G(f_{\mathrm{n}})$ [$\mathrm{V}^2.\mathrm{W}^{-2}$] is given by

$$G(f_{\mathrm{n}}) = \frac{S_{white}}{S_{SN}}. \tag{4.4}$$

Our detector gain curve $G(f_{\mathrm{n}})$ is depicted in Fig. 4.2. From the gain curve we measured a low frequency cutoff at 10 kHz and a high frequency cutoff

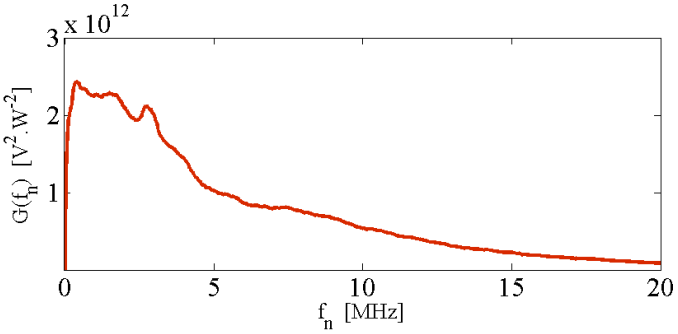

Figure 4.2 – The gain curve recorded at the AC output of a trans-impedance photodiode accompanied by an amplifier.

of 6 MHz for the AC output of our trans-impedance photodiode with the amplifier.

Oscilloscope and unit conversion

The FFT function in the oscilloscopes usually represents the power spectrum of the electric signal in a logarithmic scale with a dBm unit. This unit is converted to watt by the following equation

$$P_{el}\ [\text{watt}]\ = 10^{\frac{P_{el}\ [\text{dBm}]\ -30}{10}}. \tag{4.5}$$

The detected light on a photodiode generates a voltage signal $U(f_\text{n})$ based on its gain curve.

$$U(f_\text{n}) = P_{opt}(f_\text{n}) \times \sqrt{G(f_\text{n})}. \tag{4.6}$$

This voltage signal in the oscilloscope then converted to electrical power depends on the loading impedance $\mathcal{R} = 50\,\Omega$ and the impedance coupling of the oscilloscope $\mathcal{C}$ as follows $P_{el}[\text{watt}] = \frac{U^2(f_\text{n})}{\mathcal{C}\mathcal{R}}$. For coupling of $50\,\Omega$, $\mathcal{C} = 1$ and for coupling of $1\,M\Omega$, $\mathcal{C} = 1/4$. Finally the oscilloscope FFT represents the one-sided optical power spectrum given by

$$P^2_{opt}(f_\text{n})[W^2] = \frac{\mathcal{C}\mathcal{R}}{2G(f_\text{n})} \times 10^{\frac{P_{el}\ [\text{dBm}]\ +30}{10}}. \tag{4.7}$$

Therefore with this conversion we get data in the meaningful optical power unit. Note that to get PSD, one needs to divide Eq. 4.7 by the frequency resolution of the oscilloscope *df* in [Hz].

Intensity noise measurements

The intensity fluctuation measurements are ultimately limited by the shot noise. In this case, the PSD is flat (frequency independent) and proportional

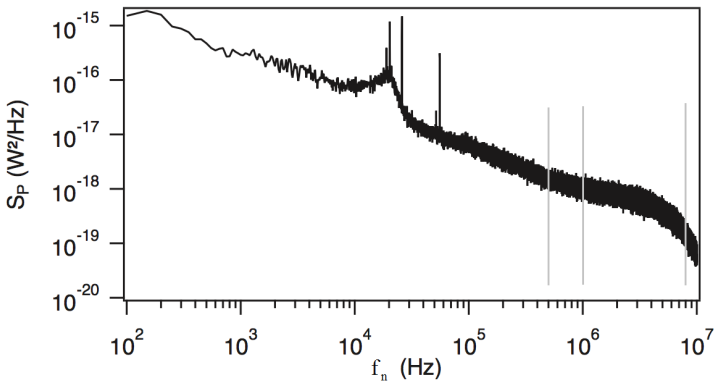

Figure 4.3 – Typical intensity noise S_P of the DFB laser as a function of Fourier frequency $f_{\rm n}$, obtained with a mean laser power of 80μW. The gray vertical lines indicate specific frequencies which is used to extract the noise power as a function of optical power in Fig. 4.4.

to the mean laser power $\overline{P}$ (Eq. 4.3). That means the shot noise scales linearly with the optical power. On the other hand, when the intensity noise is dominated by technical noises, e.g. electronic noise, the PSD is proportional to the square of the mean laser power

$$\begin{aligned} S_{P,\text{ shot noise}}(f_{\rm n}) &\propto \overline{P} \\ S_{P,\text{ classical noise}}(f_{\rm n}) &\propto \overline{P}^2. \end{aligned} \tag{4.8}$$

Thus, measuring $S_P(f_{\rm n})$ at a certain frequency as a function of $\overline{P}$ allows to extract some of the noise features (Fig. 4.3).

The intensity fluctuations PSD of the DFB laser as a function of the mean power is plotted in Fig. 4.4 for different Fourier frequencies [1]. The mean power has been varied by adding some neutral density (ND) filters. Data are well fitted by a square law indicating a classical noise. The PSD corresponding to the shot noise limitation, given by Eq. 4.3, is also added.

The intensity fluctuations in general could be due to the combination of both classical and shot noise. In a range of very low optical power, classical noise vanishes and the shot noise is dominant. By contrast, as the optical power increases, the classical noise grows faster and becomes dominant (Fig. 4.5). This figure shows clearly that even for a laser intensity dominated by classical noise, reducing the optical power can end up to a regime in which the intensity noise might be dominated by the shot noise.

[1] The background is removed from the detected signal as follows : $S_P = S_{P,\text{detected}} - S_{P,\text{background}}$. $S_{P,\text{detected}}$ corresponds to the signal detected when the laser is on, while $S_{P,\text{background}}$ corresponds to the measured signal with no incident light on the detector.

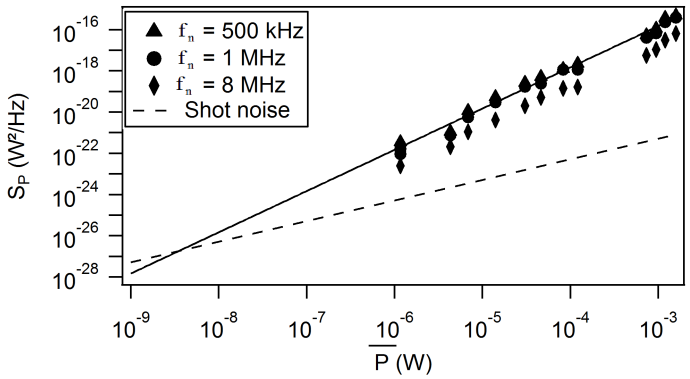

Figure 4.4 – Power spectral density S_P of the DFB laser intensity fluctuations as a function of the mean power at different frequencies. The data are well fitted by a square law (solid line with $f_{\mathrm{n}} = 1\,\mathrm{MHz}$) corresponding to a classical noise. The dashed line corresponds to the shot noise level calculated by Eq. 4.3.

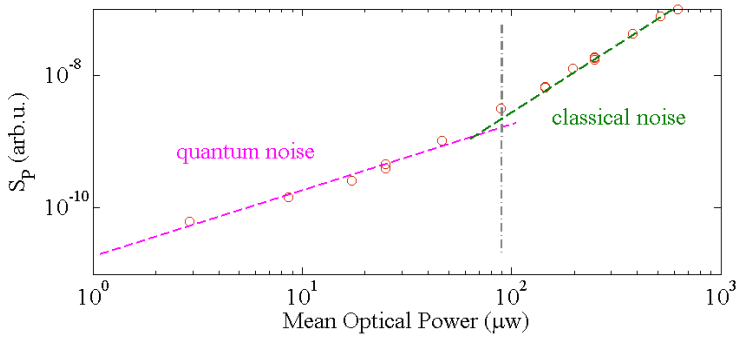

Figure 4.5 – The intensity fluctuations of a laser diode as a function of the mean incident optical power at $f_{\mathrm{n}} = 400\,\mathrm{kHz}$. The noise power scaled linearly up to $\sim 100\mu\mathrm{W}$ which describes the shot noise limited domain, while above this power, noise power is scaled quadratically which shows classical noise domain.

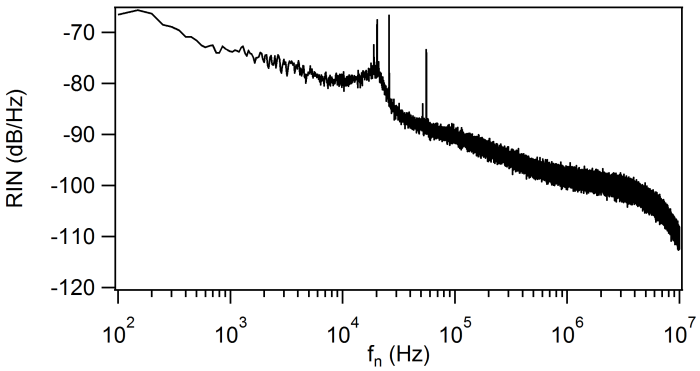

Figure 4.6 – Relative intensity noise for the DFB laser diode. The mean power is about 80μW.

Intensity noise is usually expressed as relative intensity noise (RIN)

$$\text{RIN [dB/Hz]} = 10\log\Big(\frac{S_P(f_\text{n})[\text{W}^2/\text{Hz}]}{\overline{P}^2[\text{W}^2]}\Big). \tag{4.9}$$

With this definition, the RIN will be constant for classical noise. For quantum noise, the RIN depends on the beam power and in particular it increases when $\overline{P}$ decreases. The RIN of the DFB laser diode is plotted in Fig. 4.6. The mean power in this measurement is about 80μW.

As a conclusion, the intensity noise of the lasers in our experiment were characterized. For the power used in our experiments (typically a few μW), the DFB is limited by the classical noise. In the following, intensity noise does not limit the other characterization measurements such as the beat-note and the frequency noise measurements.

4.1.2 Laser optical spectrum

Using the beat-note measurement, we can characterize the laser optical spectrum and its linewidth. The schematic of the measurement is depicted in Fig. 4.7. In this measurement two lasers are injected into an optical fiber and combined by a 50:50 fibered coupler. The signal is collected then by a 9.5 GHz bandwidth photodiode (Thorlabs PDA8GS) which is connected to a spectrum analyzer. Depending on the running frequency of each laser, the beat-note signal appears at the difference frequency of the two lasers on the spectrum analyzer.

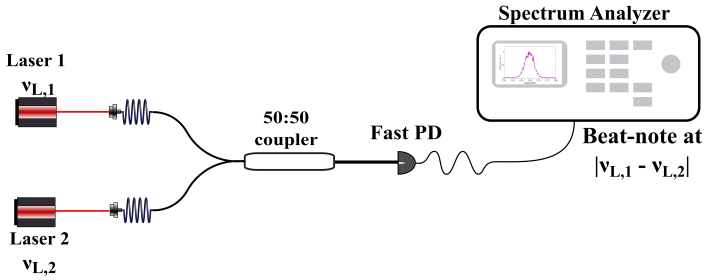

Figure 4.7 – Beat-note setup to measure laser line shapes. Two lasers are injected into a 50:50 fiber coupler. The beat-note signal is detected by a fast photodiode (PD). The signal is finally analyzed with a spectrum analyzer.

Laser line shape

The laser line shape corresponds to the shape of the power spectral density (PSD) of the laser electric field $S_E(\nu)$. To measure it, we use the beat-note technique. The basics of this technique were already explained in Sec. 3.2.2. The electric field of each laser can be described by

$$\begin{aligned} E_1(t) &= E_{0,1}e^{i2\pi\nu_{\mathrm{L},1}t} \\ E_2(t) &= E_{0,2}(t)e^{i\left[2\pi\nu_{\mathrm{L},2}t+\phi(t)\right]}, \end{aligned} \tag{4.10}$$

where $\phi(t)$ is a time dependent relative phase between the two lasers. The first laser is supposed to be perfect here, or at least with a very narrow line and with a very low intensity and frequency noises compared to the second laser. Therefore the intensity detected by the photodiode (PD) can be written as

$$\begin{aligned} I_{\mathrm{BN}}(t) &= |E_1 + E_2|^2 \\ &= |E_{0,1}|^2 + |E_{0,2}|^2 + \\ &\quad +2E_{0,1}E_{0,2}(t)\cos\left[2\pi\big(\nu_{\mathrm{L},2} - \nu_{\mathrm{L},1}\big)t + \phi(t)\right]. \end{aligned} \tag{4.11}$$

The two first terms in Eq. 4.11 correspond to the DC component. Thus the PSD of I_{BN} represents the line shape of the laser 2, shifted to the frequency $|\nu_{\mathrm{L},2} - \nu_{\mathrm{L},1}|$. However, in reality, the first laser has a finite spectrum which should be taken into account. Thus the beat-note signal would be a result of the convolution of the two laser line shapes. In a particular case, if one of the lasers has much narrower spectrum than the other one (reference laser), the beat-note signal can be approximated as the line shape of the broader laser.

A typical beat-note is shown in Fig. 4.8. The TOPTICA laser in this figure has a very narrow line compared to the DFB, and the TOPTICA

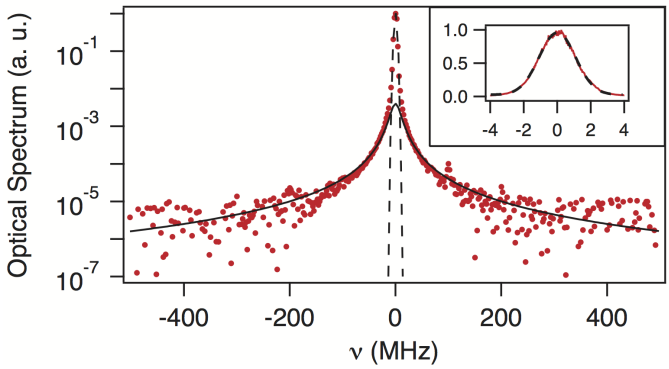

Figure 4.8 – Beat-note signal PSD between the DFB laser and the TOPTICA laser. The center of the spectrum has been shifted to the origin. Since the TOPTICA laser has a much smaller linewidth than the DFB laser one, it can be treated as a reference laser and the PSD mainly corresponds to the optical spectrum of the DFB laser. The central part can be fitted by a Gaussian (dashed line) with a FWHM $\Delta\nu_{\mathrm{BN}} \simeq 3\,\mathrm{MHz}$, and the wings are well fitted by a Lorentzian (solid line). Inset: zoom on the Gaussian part of the optical spectrum. Red curve: beat-note signal PSD. Dashed curve: Gaussian fit.

is taken as the reference laser. Therefore the beat-note spectrum reflects the optical spectrum of the DFB. The PSD peak has been shifted to the origin and it consists of two parts. A central part which can be fitted by a Gaussian, superimposed on large wings with a Lorentzian shape and with a relative amplitude of approximately 10^{-3}. The Lorentzian fit gives a full width at half maximum (FWHM) of 20 MHz.

Laser linewidth

The laser linewidth $\Delta\nu_{\mathrm{L}}$ corresponds to the FWHM of the laser electric field spectrum. As mentioned before, the beat-note profile is a convolution of the two lasers optical spectra. The Gaussian part can be estimated as the main optical spectrum which is responsible of the laser linewidth. This approximation is valid as the amplitude of the Gaussian part is typically 10^3 times larger than the Lorentzian. The convolution of two Gaussian will be also a Gaussian and the FWHM of the beat-note is given by

$$\Delta\nu_{\mathrm{BN}} = \sqrt{\Delta\nu_{\mathrm{L},1}^2 + \Delta\nu_{\mathrm{L},2}^2}, \tag{4.12}$$

where $\Delta\nu_{\mathrm{BN}}$ is the FWHM of the beat-note profile extracted by a Gaussian fit, $\Delta\nu_{\mathrm{L,i}}$ is the FWHM of the lasers optical spectrum. If a reference laser is

used with a negligible linewidth, then the beat-note FWHM directly gives the linewidth of the second laser. For instance in Fig. 4.8, the TOPTICA laser was considered as a reference laser. Therefore a linewidth of $\Delta\nu_{\mathrm{L}} \simeq 3\,\mathrm{MHz}$ is estimated for the DFB from a Gaussian fit.

Nevertheless if the linewidth of the reference laser is unknown the above approximation could be not valid. An alternative method to measure the laser linewidth by the beat-note technique is to use at least three different lasers. In this way we can characterize the linewidth of all the three lasers. We used three lasers as explained in the following:

- A distributed-feedback (DFB) laser amplified by a master oscillator power amplifier (MOPA). The laser frequency is locked to an atomic transition using a master/slave configuration with an offset locking scheme. The master is locked to the ^{87}Rb crossover of the $F = 2 \rightarrow F' = 2, 3$ transition thanks to a saturated absorption spectroscopy method, the error signal being obtained by modulating the laser current. The DFB laser frequency is shifted to the closest ^{85}Rb hyperfine transition thanks to the offset lock.

- A home-made external-cavity diode laser (ECDL) provided by SYRTE. This laser diode is locked to the ^{85}Rb crossover of the $F = 3 \rightarrow F' = 3, 4$ transition. The error signal is obtained by modulating the longitudinal magnetic field applied on the saturated absorption cell.

- A commercial external-cavity diode laser from the TOPTICA company. It is locked to the ^{85}Rb crossover of the $F = 3 \rightarrow F' = 3, 4$ transition with the same modulating scheme used for the SYRTE laser diode.

Now, there are three different combinations to make the beat-note, first DFB and TOPTICA, then DFB and SYRTE, and finally SYRTE and TOPTICA (Fig. 4.9). Thus from the beat-note experiment we can measure three FWHM values for three different combinations. Considering Eq. 4.12, we would have then three equations with three unknown linewidths. The results are summarized in table 4.2. The beat-note for each pair of lasers was recorded after 100 averaging on the spectrum analyzer with a sweep time of 0.5 s. Then by applying a Gaussian fit, the linewidth of the beat-note is calculated. This procedure is repeated several times in order to calculate the statistical uncertainty which is given at 1σ. Therefore the uncertainties in table 4.2 have been obtained with a statistical analysis of different beat-note signals recorded in the same conditions.

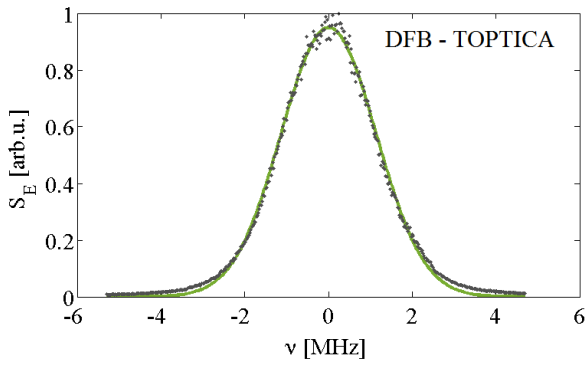

(a)

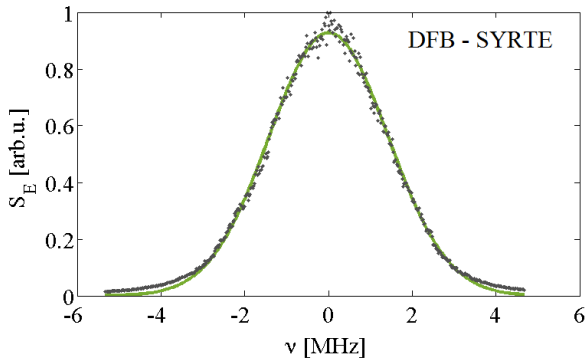

(b)

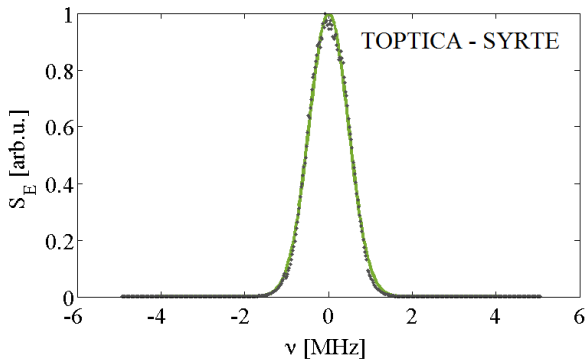

(c)

Figure 4.9 – The central parts of the beat-note PSD profiles for the (a) DFB and Toptica, (b) DFB and SYRTE and (c) SYRTE and Toptica laser diodes and their Gaussian fits. All the beat-notes were shifted to the origin. The fits give FWHM $= 0.49\,\Gamma$, $= 0.52\,\Gamma$, and $= 0.18\,\Gamma$ respectively. Each beat-note are recorded after 100 averaging. The resolution bandwidth (RBW) and video bandwidth (VBW) were set on 1 kHz and the spectrum analyzer span was 10 MHz.

Table 4.2 – Beat-note and deduced laser linewidth, compared to the expected values. The uncertainties are statistical errors taken at 1σ.

Beat-note linewidth	TOPTICA - DFB	$3.0(\pm 0.2)$ MHz
	TOPTICA - SYRTE	$1.11(\pm 0.03)$ MHz
	SYRTE - DFB	$3.16(\pm 0.13)$ MHz
Measured laser linewidth	TOPTICA	$0.2(+1.5/-0.2)$ MHz
	SYRTE	$1.1(\pm 0.3)$ MHz
	SYRTE + low-pass filter	$\simeq 0.8$ MHz
	DFB	$3.0(\pm 0.2)$ MHz
Expected laser linewidth	TOPTICA	< 500 kHz (from the datasheet)
	SYRTE	a few 100 kHz [135]
	DFB	3 MHz [136]

Effect of electronic noise on the linewidth

As discussed in the beginning of this section, the technical noise can affect the laser optical spectrum, and broaden its linewidth. These technical noise sources usually can be reduced by some efforts. For instance the electronic noise of the laser driver is directly fed into the diode and converted to intensity and frequency fluctuations. Adding a low pass RC filter to the output of the driver can reduce and cut a part of the electronic noise out. Consequently the lock-in bandwidth would be limited by the frequency cutoff of the filter. In Fig. 4.10 the effect of a RC filter on reducing the linewidth of the laser is demonstrated. In this measurement, beat-note between a DFB and a distributed Bragg reflector (DBR), with expected linewidth of ≈ 2 MHz, lasers was observed. Then by applying a low-pass RC filter with a cutoff frequency at $f_c = 2.7$ kHz to the current supply of the DFB laser diode. The beat-note was observed again and showed a narrower linewidth. This means a cheap and simple RC filter can improve the linewidth of a laser by reducing the electronic noise in the current which is fed into the laser diode. However that filter can cut or weaken the feedback signal of the lock. Thus the frequency lock of the laser would be more fragile.

Another device which can induce noise and broaden the laser optical spectrum is the AOM. In our experiment, the amplitude and the frequency of AOMs are controlled by homemade voltage-controlled oscillators (VCO). The electronic noise in VCOs output can affect the performance of the

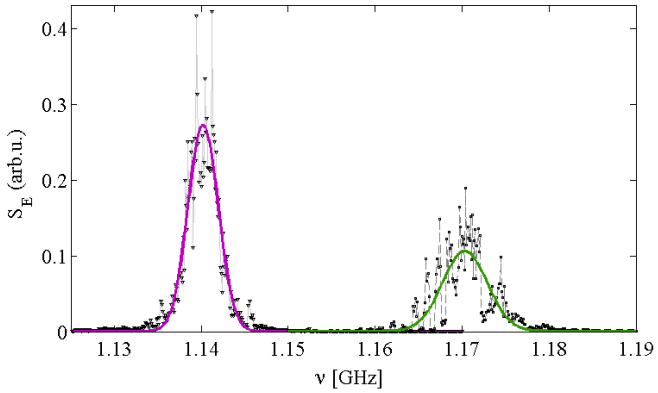

Figure 4.10 – The beat-note signals between a DFB and a DBR lasers frequency locked, with (triangle marks) and without (square marks) a low-pass RC filter at the output of the laser driver with a cutoff frequency at $f_c = 2.7\,\text{kHz}$. Gaussian fits (purple and green respectively) were applied to measure the linewidth. The RC filter reduces the electronic noise in the current driver and narrows down the beat-note linewidth from 6 to 4 MHz.

AOMs, and thus affect the laser linewidth. On the other hand synthesizers are known as the most precise function generator and can be employed for controlling AOMs. The schematic of this measurement is depicted in Fig. 4.11a. In Fig. 4.12 the effect of the electronic noises in an AOM on the laser optical spectrum is depicted. Although the measurement confirms a broadening associated to the VCO electronic noise, for the DFB laser with 3 MHz linewidth this broadening is negligible. However this effect has to be taken into account when a narrow linewidth laser, such as TOPTICA, is being used.

Similarly, one can expect that the tapered amplifier also induces noise to the laser electric field. The setup is depicted in Fig. 4.11b. However our investigation did not show any noticeable effect on the beat-note profile (Fig. 4.13).

4.1.3 Laser frequency noise

To better characterize frequency and phase fluctuations in a laser, the PSD of frequency noise is measured. The frequency noise is noise of the instantaneous frequency of an oscillating signal. The instantaneous frequency is defined as

$$\nu_{\text{L}}(t) = \frac{1}{2\pi}\left[\frac{d\phi}{dt} + \omega_{\text{L}}\right], \tag{4.13}$$

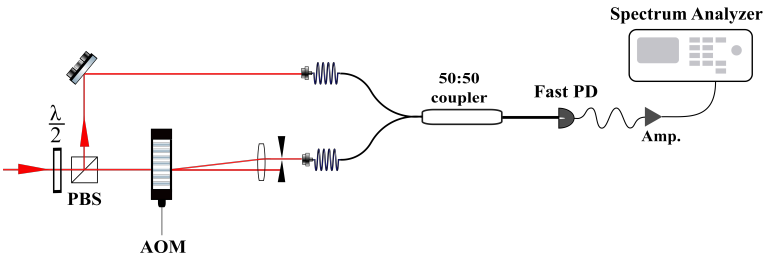

(a)

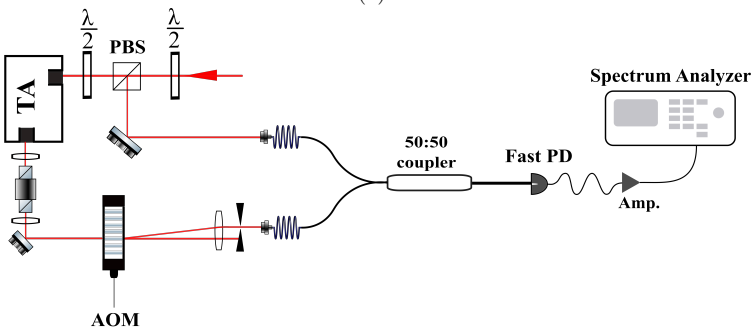

(b)

Figure 4.11 – Schematic beat-note measurement setup to study the effect of electronic noise of (a) the AOM drivers and (b) the tapered amplifier (TA). To study the broadening due to the amplifier, we used synthesizer to drive the AOM, then the beat-note taken by the setup (a) is compared with the one taken by the setup (b) (Fig. 4.13).

where ϕ is a phase in the electric field (Eq. 4.1). The PSDs of both frequency and phase noises are linked by

$$S_{\nu_\mathrm{L}}(f_\mathrm{n}) = f_\mathrm{n}^2 S_\phi(f_\mathrm{n}), \tag{4.14}$$

where $S_{\nu_\mathrm{L}}(f_\mathrm{n})$ and $S_\phi(f_\mathrm{n})$ are the PSDs of frequency and phase fluctuations respectively, and f_n is the Fourier frequency. Eq. 4.14 means that a random walk phase noise ($S_\phi = h'_{-2} f_\mathrm{n}^{-2}$) is equivalent to a white frequency noise ($S_{\nu_\mathrm{L}} = h_0$), where h'_{-2} and h_0 are constants. Usually the frequency noise PSD (FNPSD) can be composed of different noise component [137]

$$S_{\nu_\mathrm{L}}(f_\mathrm{n}) = \sum_{\alpha=-2}^{+2} h_\alpha f_\mathrm{n}^\alpha. \tag{4.15}$$

In table 4.3, the noise is categorized based on its PSD behavior as a function of the frequency. These different categories can be associated with some well-known technical and electronic noises. For instance, the electronic thermal

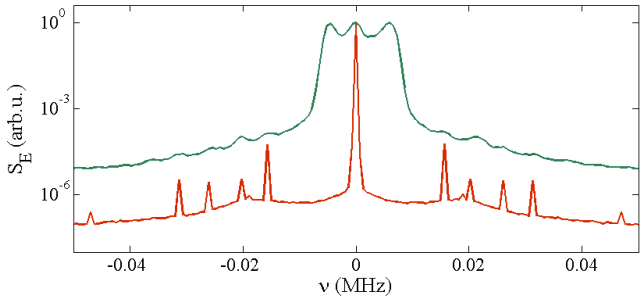

Figure 4.12 – The effect of the electronic noise in the driver of an AOM on the beat-note linewidth of the DFB laser. In this measurement, the self beat-note profiles of the DFB laser with one beam which is diffracted by an AOM controlled by a homemade VCO (blue line) and by a Rohde & Schwarz synthesizer (red line) were recorded. The scheme of the measurement is illustrated in Fig. 4.11a. The beat-notes were shifted to the origin. The video bandwidth (VBW) and the resolution bandwidth (RBW) were set at 30 Hz with a span of 100 kHz on the spectrum analyzer and the beat-notes were recorded after 300 samples averaging.

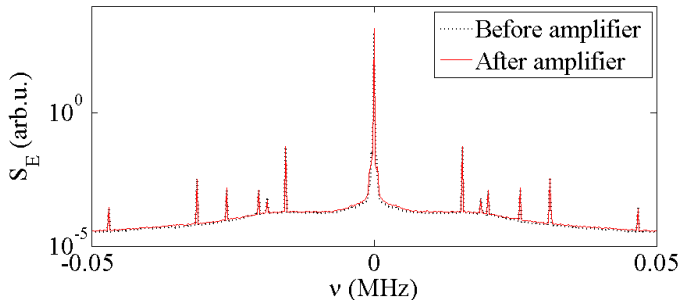

Figure 4.13 – The effect of the tapered amplifier on the beat-note linewidth of the DFB laser. In this measurement, the self beat-note profiles of the DFB laser without (dashed black line) and with (solid red line) a tapered amplifier were recorded. An AOM driven by a synthesizer was used to make 100 MHz frequency shift in the beat-note. The basis of the measurement was presented in Fig. 4.11b. Both curves are almost the same and thus there is no broadening due to the amplifier. The VBW and RBW were set at 10 Hz with a span of 100 kHz on the spectrum analyzer and the beat-notes were recorded after 100 samples averaging.

noise (JohnsonNyquist noise) is generated due to the thermal agitation of the charge carriers at equilibrium. It has a flat FNPSD and nearly frequency independent similar to the shot noise. Thus, if the PSD, or part of it, contains a flat white noise, it can correspond to these types of noises. Another example is the electronic flicker noise with a $1/f_{\rm n}$ PSD. It occurs almost in all the electronic devices.

Table 4.3 – Different frequency noise component, classified based on their frequency functionality.

Name of Noise	α	$\mathbf{S}_{\nu_{\rm L}}(\mathbf{f}_{\rm n})$
White phase	2	$h_2 f_{\rm n}^2$
Flicker phase	1	$h_1 f_{\rm n}$
White frequency	0	h_0
Flicker frequency	-1	$h_{-1} f_{\rm n}^{-1}$
Random walk frequency	-2	$h_{-2} f_{\rm n}^{-2}$

Frequency noise to intensity noise conversion

In order to measure frequency noise, one needs to transform the frequency fluctuations to intensity one, which is measurable on a photodetector (Fig. 4.14). By using a linear frequency discriminator or a filter, the intensity at the output $I_T(\nu_{\rm L})$ would depend on the incident light frequency $I_i(\nu_{\rm L})$

$$I_T(\nu_{\rm L}) = I_i(\nu_{\rm L}) T(\nu_{\rm L}), \tag{4.16}$$

where $T(\nu)$ is the frequency response of the filter. Now in the presence of frequency noise, the output intensity can be expanded as

$$\begin{aligned} I_T(\nu_{\rm L}) &= {\rm DC} + \delta I_T(\nu_{\rm L}) \\ &= I_i(\nu_{\rm L}) T(\nu_{\rm L}) + \delta\nu_{\rm L} \Big[T \frac{\partial I_i}{\partial \nu}\Big|_{\nu=\nu_{\rm L}} + I_i \frac{\partial T}{\partial \nu}\Big|_{\nu=\nu_{\rm L}} \Big]. \end{aligned} \tag{4.17}$$

The first term in rhs. of Eq. 4.17 is a DC component, the second term represent the intensity fluctuations of the incident light, and the last term describes the fluctuations in the output intensity corresponding to the frequency fluctuations. Assuming negligible intensity fluctuations, the frequency noise can then be described by

$$\delta\nu_{\rm L}^2 = \frac{\delta I_T^2(\nu_{\rm L})}{I_i^2 \left| \frac{dT}{d\nu} \right|^2_{\nu=\nu_{\rm L}}}. \tag{4.18}$$

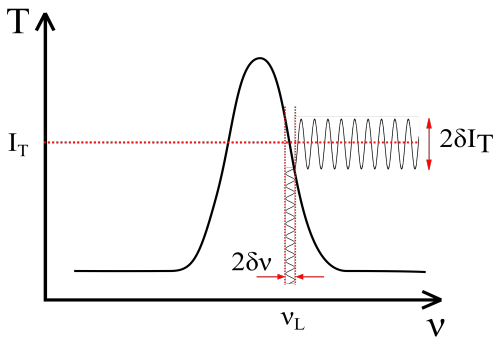

Figure 4.14 – Schematic diagram for frequency to intensity conversion using an optical frequency discriminator.

Eq. 4.18 can be equivalently written in terms of frequency and transmitted intensity noise PSDs normalized by the incident laser intensity

$$S_{\nu_\mathrm{L}} = \frac{S_T}{\left|\frac{dT}{d\nu}\right|^2_{\nu=\nu_\mathrm{L}}}, \tag{4.19}$$

where $S_{\nu_\mathrm{L}} \propto \delta\nu_\mathrm{L}^2$ and $S_T \propto \delta I_T^2(\nu_\mathrm{L})/I_i^2$. As a result, by measuring the power of intensity fluctuations and using the derivative of the filter response one can extract the frequency noise.

Frequency noise measurement using a Fabry-Perot cavity

We used a confocal Fabry-Perot cavity as frequency discriminator as shown in Fig. 4.16b. The transmission function of the incident light from a Fabry-Perot cavity depends on the length of the cavity L_c as well as on the laser frequency ν_L

$$T_c(\nu_\mathrm{L}) \quad = \quad \frac{1}{1+\frac{4\mathcal{F}^2}{\pi^2}\sin^2\left(\frac{4\pi(\nu_\mathrm{L}-\nu_0)L_c}{c}\right)}, \tag{4.20}$$

where ν_0 is the cavity resonance, $\mathcal{F} = \Delta\nu_{FSR}/\Delta\nu_c$ is the finesse of the cavity, $\Delta\nu_{FSR} = c/4L_c$ is the free spectral range which is the frequency interval between two consecutive transmission resonances, and finally $\Delta\nu_c$ is the cavity linewidth which is deduced by a Lorentzian fit of a cavity resonance. Close to the cavity resonance $T_c(\nu_\mathrm{L})$ can be approximated by

$$T_c(\nu_\mathrm{L}) \simeq \frac{1}{1+4\left(\frac{\nu_\mathrm{L}-\nu_0}{\Delta\nu_c}\right)^2} \tag{4.21}$$

and thus

$$\frac{dT_c(\nu_{\mathrm{L}})}{d\nu_{\mathrm{L}}} = \frac{8\frac{\nu_{\mathrm{L}}-\nu_0}{\Delta\nu_c^2}}{\left[1+4\left(\frac{\nu_{\mathrm{L}}-\nu_0}{\Delta\nu_c}\right)^2\right]^2}. \tag{4.22}$$

Now replacing this equation into Eq. 4.19, one can measure the frequency noise of a laser. However Eq. 4.19 is valid only if the laser linewidth is much smaller than the cavity linewidth $\Delta\nu_c$ (to respect linear filtering assumption).

A typical Fabry-Perot transmission is shown in Fig. 4.15b. To perform this measurement, the frequency of the incident laser into the Fabry-Perot cavity is scanned and the output light is detected by a photodiode (Fig. 4.16a).

A triangular voltage modulation, supplied by a function generator, is fed to the laser driver to scan the laser frequency linearly. The amplitude of the voltage determines the frequency range of the scan. The calibration of the voltage amplitude versus the frequency shift can be done using the saturated spectroscopy of that laser. The frequency difference between two certain atomic resonances is known [101]. The process is demonstrated in Fig. 4.15a. From the transmission signal in Fig. 4.15b we measured a free spectral range $\Delta\nu_{FSR} = 980\,\mathrm{MHz}$ which corresponds to the cavity length of $L_c \simeq 13\,\mathrm{cm}$. A Lorentzian fit applied to one of the transmission peaks gives a cavity linewidth of $\Delta\nu_c = 73\,\mathrm{MHz}$ as shown in Fig. 4.16b. Therefore the finesse would be $\mathcal{F} = \Delta\nu_{FSR}/\Delta\nu_c = 13$. We have also checked that the background and the intensity noises do not limit the measurements. Given the value, at most 3 MHz, of the linewidth of the lasers, the value $\Delta\nu_c = 73\,\mathrm{MHz}$ is large enough to fulfill the condition, recalled above, of linear frequency to intensity conversion.

For frequency noise measurement, experimentally, the cavity resonance frequency is adjusted via the cavity length in order to set the transmission signal to be at half of the resonance. This condition corresponds to the best frequency to intensity conversion with $|dT_c/d\nu_{\mathrm{L}}| = 1/\Delta\nu_c$ at maximum.

The frequency noise is plotted in Fig. 4.17 for the DFB laser and for the TOPTICA laser diode. The frequency noise power spectral density FNPSD of the DFB laser is higher than the one obtained with the TOPTICA laser, which was expected considering each laser linewidth. The DFB FNPSD mainly exhibits a flicker noise ($1/f_{\mathrm{n}}$ noise). The TOPTICA also shows a $1/f_{\mathrm{n}}$ noise up to 1 MHz.

We can also calculate the frequency noise standard deviation using the following equation

$$\sigma_{\nu_{\mathrm{L}}} = \sqrt{\int S_{\nu_{\mathrm{L}}} df_{\mathrm{n}}}. \tag{4.23}$$

The results are listed in table 4.4

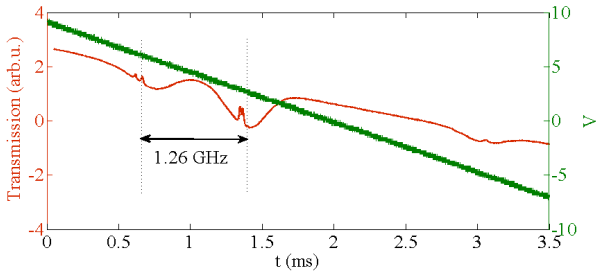

(a)

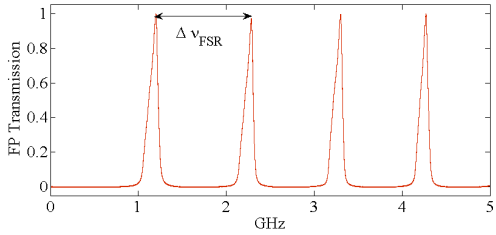

(b)

Figure 4.15 – (a) The transmission spectra of the rubidium atoms (red curve) while the frequency of the laser was scanned by a triangular voltage (green curve) produced by a function generator and injected into the laser driver. By changing the amplitude of the voltage signal we can change the range of frequency scan. In the atomic spectrum, ^{87}Rb $F = 2 \rightarrow F' = 2, 3$ and ^{85}Rb $F = 3 \rightarrow F' = 4$ transitions with a frequency distance of 1.26 GHz are marked which corresponds to a conversion of 1.19 V.GHz^{-1}. (b) Transmission of the Fabry-Perot cavity by scanning the frequency of the laser via a triangular voltage. The transmission is plotted as a function of laser frequency scan thanks to the previous conversion factor. The space between two consecutive transmission peaks is the free spectral range of the cavity ($\Delta\nu_{FSR} = 980$ MHz). Applying a Lorentzian fit also to one of the peaks gives a cavity linewidth of $\Delta\nu_c = 73$ MHz and thus the finesse is $\mathcal{F} = 13$.

Table 4.4 – Frequency noise standard deviation σ_{ν_L} for the TOPTICA and the DFB lasers calculated by Eq. 4.23.

Laser	σ_{ν_L}
TOPTICA	365 kHz
DFB	3 MHz

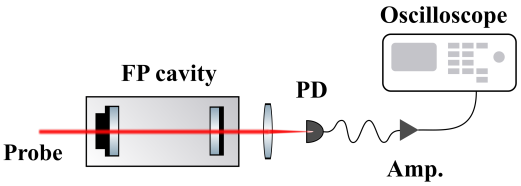

(a)

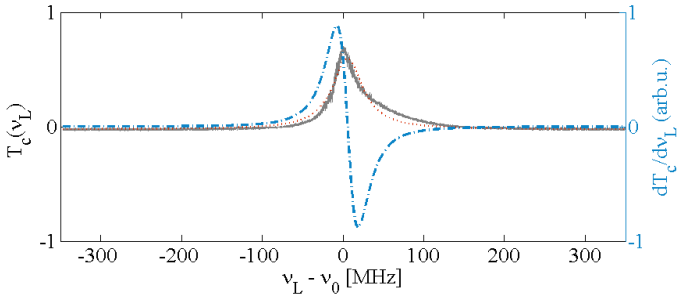

(b)

Figure 4.16 – (a) Schematic of the frequency noise power spectral density (FNPSD) measurement using a Fabry-Perot cavity as a frequency discriminator. (b) A typical intensity transmission from a Fabry-Perot cavity(gray line). A Lorentzian fit can be applied to this experimental curve to measure the cavity linewidth $\Delta\nu_c$ (red dotted line). The derivative $dT_c/d\nu_L$ (blue dashed line) is also demonstrated to show the optimum frequency to intensity noise conversion, occurring at half maximum of the transmission where $|dT_c/d\nu_L|$ is maximum.

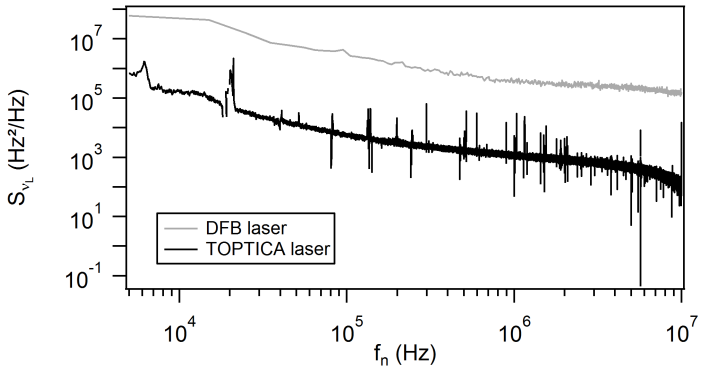

Figure 4.17 – Frequency noise PSD for the DFB and the TOPTICA lasers.

4.1.4 Relation between optical spectrum and frequency noise

The optical spectrum $S_E(\nu)$, which describes the line-shape, can be recovered from $S_{\nu_L}(f_n)$ [138]

$$S_E(\nu) = 2\int_{-\infty}^{\infty} E_0^2 e^{i2\pi(\nu_L-\nu)\tau} \exp\Big(-2\int_0^{\infty} S_{\nu_L}(f_n)\frac{\sin^2(\pi f_n \tau)}{f_n^2} df_n\Big) d\tau. \tag{4.24}$$

This general formula, most often cannot be integrated analytically, except for a simple and trivial case of white noise ($S_{\nu_L}(f_n) = h_0$ with h_0 given in Hz^2/Hz). Regarding

$$\int_0^{\infty} \frac{\sin^2 x}{x^2} dx = \frac{\pi}{2}, \tag{4.25}$$

Eq. 4.24 becomes

$$S_E(\nu) = 2\int_{-\infty}^{\infty} E_0^2 e^{i2\pi(\nu_L-\nu)\tau} \exp\left(-\pi^2 h_0 \tau\right) d\tau. \tag{4.26}$$

This is the Fourier transform of an exponential decay with a time constant of $1/\pi^2 h_0$ which leads to a Lorentzian optical spectrum with FWHM$= \pi h_0$.

In any real noise measurement, there is a finite bandwidth B, which has to be taken into account. It is interesting to calculate the optical spectrum $S_E(\nu)$ in the presence of a frequency cutoff. In particular if we approximate $S_{\nu_L}(f_n)$ with a rectangular function, Eq. 4.24 thus becomes

$$S_E(\nu) = 2\int_{-\infty}^{\infty} E_0^2 e^{i2\pi(\nu_L-\nu)\tau} \exp\Big(-2\pi h_0 \tau \int_0^{B\pi\tau} \frac{\sin^2(x)}{x^2} dx\Big) d\tau. \tag{4.27}$$

Here we consider two limiting cases:

- $B \gg h_0$
  in this case, the integral $\int_0^{B\pi\tau} \sin^2(x)/x^2 dx$ can be approximated by its asymptotic value, $\pi/2$. Therefore Eq. 4.27 changing again to the Fourier transform of a decaying exponent which leads to a Lorentzian optical spectrum

  $$S_E(\nu) \approx \frac{E_0^2 h_0}{(\frac{\pi h_0}{2})^2 + (\nu_L - \nu)^2}, \tag{4.28}$$

  with a FWHM linewidth

  $$\Delta\nu_L = \pi h_0. \tag{4.29}$$

- $B \ll h_0$
  in this case the exponential is significant for only small x. So $\sin^2(x)$

can be expanded which yields to $\int_0^{B\pi\tau} \sin^2(x)/x^2 dx = B\pi\tau$. Therefore Eq. 4.27 becomes

$$S_E(\nu) = 2\int_{-\infty}^{\infty} E_0^2 e^{i2\pi(\nu_L-\nu)\tau} \exp\left(-2\pi^2 B h_0 \tau^2\right) d\tau, \tag{4.30}$$

which is the Fourier transform of a Gaussian function. Thus the laser optical spectrum would be

$$S_E(\nu) \approx E_0^2 \sqrt{\frac{2}{\pi h_0 B}} \times e^{-\frac{(\nu_L-\nu)^2}{2h_0 B}}, \tag{4.31}$$

with a FWHM linewidth of

$$\Delta\nu_L = \sqrt{8 h_0 B \ln 2}. \tag{4.32}$$

For more complicated cases, Eq. 4.24 ought to be solved numerically.

A simpler approach to connect the FNPSD to the optical spectrum has been reported in references [139, 140]. This simple geometrical approximation is applicable to any arbitrary FNPSD. The basis of this approach lies on a universal β-separation line, defined as

$$S_\beta(f_n) = \frac{8\ln 2}{\pi^2} f_n. \tag{4.33}$$

Since the first theoretical study [139], this approach has been applied in many experimental setups [141, 142, 143, 144] and further refined [145, 146]. The β-line divide geometrically the FNPSD in two regions:

- $S_{\nu_L}(f_n) > S_\beta(f_n)$: in this region frequency noise contributes to the Gaussian part of the optical spectrum. Therefore this region also determines the linewidth.
- $S_{\nu_L}(f_n) < S_\beta(f_n)$: frequency noise contributes to the Lorentzian wings in the optical spectrum.

A good approximation of the laser linewidth, corresponding to the FWHM of the laser line shape, is then given by

$$\Delta\nu_L = \sqrt{8\ln(2) A}, \tag{4.34}$$

where A is the surface below $S_{\nu_L}(f_n)$ for the region where $S_{\nu_L}(f_n)$ is above the β-line

$$A = \int_{1/T_{osc}}^{\infty} H\big(S_{\nu_L}(f_n) - S_\beta(f_n)\big) S_{\nu_L}(f_n) df_n, \tag{4.35}$$

with T_{osc} the time window of the oscilloscope and H the Heaviside step function. A is demonstrated in Fig. 4.18 for the DFB and the TOPTICA lasers.

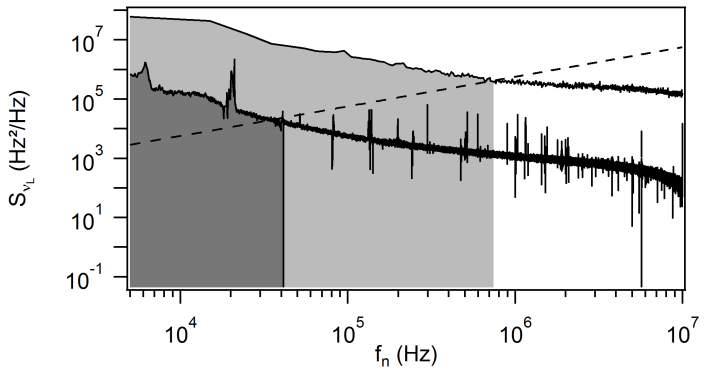

Figure 4.18 – FNPSD for the DFB and the TOPTICA lasers and geometrical approach with the β-line to estimate the laser linewidth. Dark grey area: area which contributes to the TOPTICA laser linewidth. Light grey area: area which contributes to the DFB laser linewidth.

Applying this approach, we obtain a linewidth of 3.4 ± 0.4 MHz for the DFB laser. The 10 % relative uncertainty takes into account the maximum typical error introduced by the β-line approach [145], which is again a simple method to approximate the laser linewidth. The laser linewidth is compatible with the one obtained with the beat-note measurement. The calculated linewidth are listed and compared with the results of the beat-note measurement in table 4.5.

Table 4.5 – Laser linewidth measured by the β-line approach and compared with the values from the beat-note measurements.

Laser	**Linewidth $\Delta\nu_L$**	
	β-line approximation	Beat-note measurement
TOPTICA	$0.85(\pm 0.08)$ MHz	$0.2(+1.5/-0.2)$ MHz
DFB	$3.4(\pm 0.4)$ MHz	$3.0(\pm 0.2)$ MHz

4.1.5 Frequency noise measurement using an atomic resonance

As explained in Sec. 4.1.3, to measure FNPSD one needs to convert frequency fluctuations to measurable intensity fluctuations. This conversion can be done by any frequency discriminator. In previous section we used a Fabry-Perot cavity. However the result corresponds to the convolution of the laser and the cavity resonant frequency noises. While the cavity fre-

quency noise is negligible for noisy lasers, it can become significant when the measurements are performed with narrow lasers. One solution is to use ultra stable cavities [147]. Alternatively, one can also use a molecular or an atomic transition as the frequency discriminator. This has been first reported in [148] and then extensively studied theoretically [149, 150, 151] as well as experimentally, either to measure the laser properties [152, 153], to extract atomic characteristics [154, 155] or to study the light-matter interaction [156, 157, 158, 159].

Another method is to use an atomic transition as the frequency discriminator. The experimental setup is shown in Fig. 4.19a. The measurement technique, analogous to the Fabry-Perot experiment, concerns the intensity fluctuations of a weak probe after transmission through a cloud of cold atoms. The atomic cloud is obtained by loading a magneto-optical trap (MOT) with ^{85}Rb atoms. A compression is applied to increase the atomic density. The maximum number of atoms is $N \simeq 10^{10}$ with a temperature $T \simeq 100\,\mu$K and a cloud rms radius of $R \simeq 1\,$mm.

The probe beam is the one characterized in the previous sections, delivered by the DFB laser amplified by the tapered amplifier and frequency locked close to the $F = 3 \rightarrow F' = 4$ hyperfine transition of the D2 line of ^{85}Rb. A doublepass AOM is used to change the laser detuning $\delta = (\nu_{\mathrm{L}} - \nu_0)$ from this transition. The parameter ν_{L} corresponds to the laser frequency, and ν_0 to the atomic transition frequency. The laser beam inside the atomic cloud is linearly polarized and its waist is about $300\,\mu$m. The intensity is adjusted to have a saturation parameter lower than 0.1. In order to align the beam path with the center of the atomic cloud, we apply the probe beam after a fixed $t_{TOF} = 4\,$ms time of flight (TOF).

The laser beam after propagation through the atomic cloud is collected by the same homemade trans-impedance photodiode as the one used for the measurements with the Fabry-Perot cavity. As for the measurements done with the Fabry-Perot cavity, the intensity noise PSD is normalized by the frequency response of the detection system. The probe beam is applied during $t_p = 1.2\,$ms but we fix the oscilloscope time window to $t_{osc} = 100\,\mu$s, $t_{pause} = 200\,\mu$s after the beginning of the probe pulse. To increase the signal to noise ratio, data are integrated over 100 cycles. We also record for each cycle the power of the probe beam without atoms I_0, which is needed for intensity to frequency noise conversion. This measurement is done by applying a second probe pulse after having removed all the atoms by shining the MOT beams at resonance during $t_{push} = 6\,$ms. The time sequence is sketched in Fig. 4.19b. The duration t_i includes the loading and compression stages. The optical thickness is varied by changing the total number of atoms through the MOT loading time.

Recalling Eq. 3.8, one can replace it to the Fabry-Perot transmission

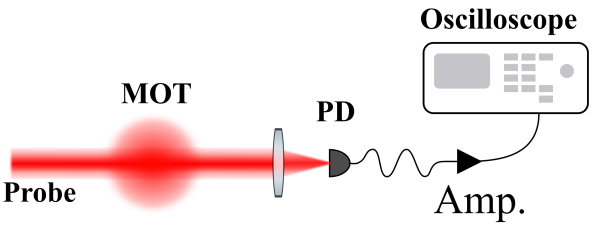

(a)

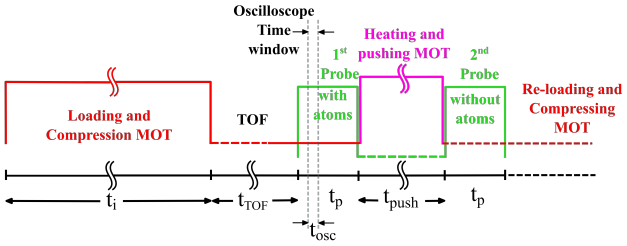

(b)

Figure 4.19 – (a) Schematic of the FNPSD measurement with the atomic transition. PD: photodiode, Amp: low noise amplifier. (b) Experimental time sequence. Typically 10^{10} atoms are loaded in the MOT and compressed to achieve high density during t_i. Then the trapping system switches off and atoms are released. Two probe pulses are applied during $t_p = 1.2\,\text{ms}$, after a time of flight of $t_{TOF} = 4\,\text{ms}$. The first pulse provides the transmission through the atomic cloud, and the second one allows us to measure the incident intensity without atoms in order to calculate the normalized transmission for each cycle. The atoms are removed by applying the MOT beams at resonance during $t_{push} = 6\,\text{ms}$ between the two probe pulses. For the PSD measurements the time window of the oscilloscope is set $t_{pause} = 200\,\mu\text{s}$ after the beginning of the first probe within $t_{osc} = 100\,\mu\text{s}$.

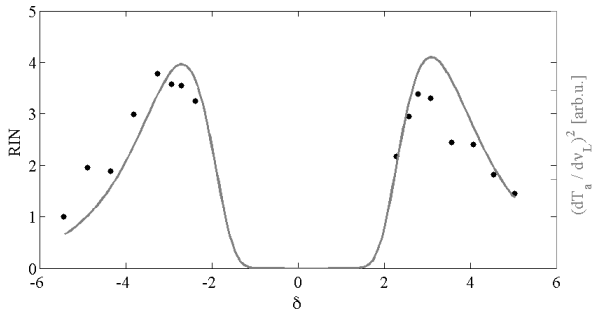

Figure 4.20 – The value of transmission noise from a cloud of cold atoms with optical thickness $b_0 = 19$ at $f_n = 500\,\text{kHz}$ taken with different laser detuning δ (dots), compared to the square of discriminator slope (solid gray line).

function in Eqs. 4.21 and 4.22. Thus

$$T_a = \frac{I_T}{I_i} = \exp\left(\frac{-b_0}{1+4\frac{\delta^2}{\Gamma^2}}\right), \tag{4.36}$$

where b_0 is the on-resonance optical thickness, $\delta = \nu_\text{L} - \nu_0$ is the laser detuning from the atomic transition, and $\Gamma = 6.06\,\text{MHz}$ is the atomic transition linewidth. As explained before, the frequency fluctuations can be converted to the intensity noise thanks to the frequency discriminator.

Based on Eq. 4.19, the relation between the PSD of the normalized transmitted intensity I_T/I_{inc} (S_T) and the FNPSD is given by

$$S_T = \left(\frac{dT_a}{d\nu_\text{L}}\right)^2 \times S_{\nu_\text{L}} = \left(\frac{dT_a}{d\delta}\right)^2 \times S_{\nu_\text{L}} = D^2 S_{\nu_\text{L}}, \tag{4.37}$$

where D is the derivative of the frequency discriminator and it is defined as

$$D = \frac{dT_a}{d\delta} = \frac{8b_0\delta}{\Gamma^2\left[1+4\left(\frac{\delta}{\Gamma}\right)^2\right]^2}\exp\left(\frac{-b_0}{1+4\frac{\delta^2}{\Gamma^2}}\right). \tag{4.38}$$

Eq. 4.37 is valid when the transmission curve can be locally approximated by a line whose slope is equal to $dT_a/d\nu_\text{L}$ (assumption of linear filtering). Moreover, the laser linewidth has to be much smaller than Γ. As we will see in Sec. 4.2, this is a good approximation for low Fourier frequencies. It is clear that the discriminator slope $dT_a/d\nu_\text{L}$ depends on b_0 as well as on the laser detuning δ.

The transmission and its derivative are plotted in Fig. 4.21 for three different on-resonance optical thickness. The optimal frequency to intensity fluctuations conversion is typically at half of the transmission. This optimum conversion is reduced as the optical thickness is increased. On the other hand, the frequency range where the conversion is linear increases. From this point of view, this system can be regarded as a Fabry-Perot cavity with an adjustable linewidth. This is particularly interesting when one wants to measure the frequency noise of a laser with a linewidth of the order of the cavity or the atomic resonance linewidth.

The efficiency of frequency to intensity noise conversion depends on the square of the discriminator slope. This is confirmed by taking the values of transmission intensity noise at the output of the discriminator at a given frequency while the incident laser frequency is scanned. This measurement results to a famous M-shaped spectrum [160, 161, 162, 163] (Fig. 4.20).

We have measured the transmitted intensity noise PSD for three different on-resonance optical thicknesses: $b_0 = 6.5$, 19 and 51.5. For each b_0, the laser detuning is adjusted to be at the maximum of the discriminator slope on the blue side of the atomic transition. We have first checked that our measurements are not limited by the detection background and that the intrinsic laser intensity noise, measured without atoms, are well below the intensity noise PSD measured with atoms. The PSD S_T is then converted to FNPSD using Eq. 4.37. The results are plotted in Fig. 4.22 for the three optical thicknesses. The frequency noise obtained via the Fabry-Perot cavity is also plotted together with the β-separation line. Although all the PSDs collapse onto the same curve at low frequencies, typically below 1 MHz, some differences appear at higher frequencies.

For low Fourier frequencies, typically below 1 MHz, Eq. 4.37 is valid and the curves plotted in Fig. 4.22 thus correspond to the laser FNPSD. Now applying the β-separation line technique, analogous to what have been done with the Fabry-Perot cavity, we estimated the laser linewidth. The results are listed and compared with the other linewidth measurement techniques in table 4.6. The uncertainties obtained with the cold atomic cloud take into account the statistical uncertainty (standard deviation of the linewidth measurements obtained in similar conditions) as well as the estimation of the maximum error due to the β-separation line approach [164].

Table 4.6 shows an agreement between all the linewidth measurements, obtained by different techniques. Thus all the methods used in this chapter to extract the linewidth of the lasers are consistent. Furthermore, it confirms that our assumption of the linear filtering is valid in our experiment.

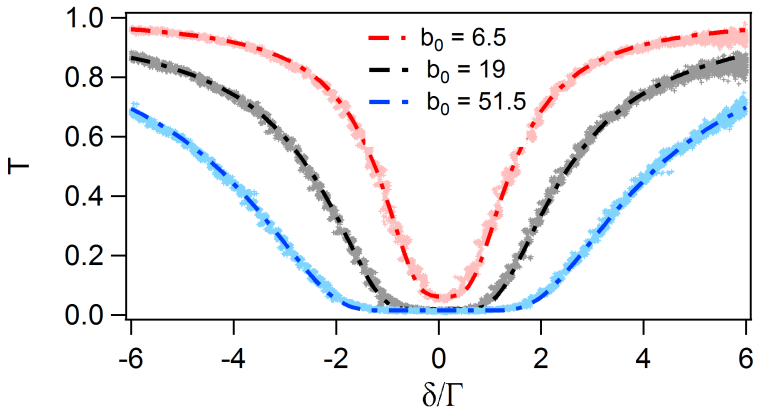

(a)

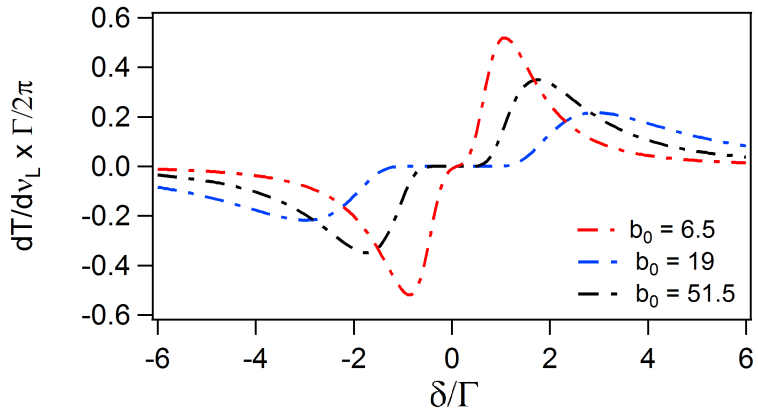

(b)

Figure 4.21 – (a) Transmission through an atomic cloud as a function of the laser detuning and for three different optical thicknesses. (b) Frequency discriminator as a function of the laser detuning. These curves are obtained from the derivative of the transmission fits and will be used for the frequency intensity noise conversion.

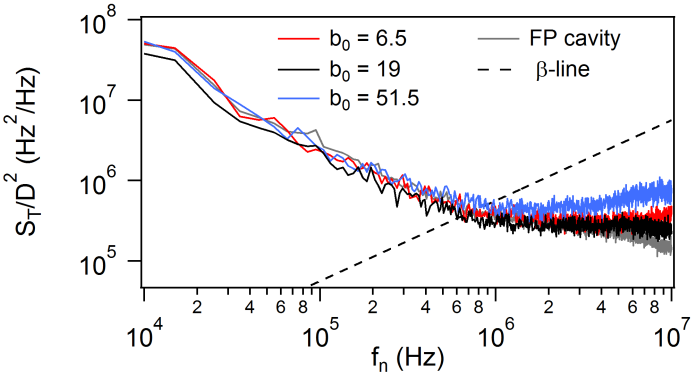

Figure 4.22 – Laser transmission noise PSD S_{In} divided by the square of the discriminator slope $D^2 = \left(dT_a/d\nu_{\mathrm{L}}\right)^2$, measured using a cold atomic cloud as a frequency discriminator. For low Fourier frequencies, Eq. 4.37 is valid and the curves thus correspond to the laser FNPSD. The FNPSD measured with the Fabry-Perot cavity is plotted in grey. The β-line corresponds to the dashed line.

Table 4.6 – DFB laser linewidth measured by different techniques.

Experimental technique		**Linewidth $\Delta\nu_{\mathrm{L}}$**
Beat-note		3 ± 0.2 MHz
Fabry-Perot cavity		3.4 ± 0.4 MHz
Cold atoms transmission	$b_0 = 6.5$	3.7 ± 0.5 MHz
	$b_0 = 19$	3.3 ± 0.5 MHz
	$b_0 = 51.5$	3.7 ± 0.5 MHz
deconvolution of a small transmission spectra Fig. 3.20		3.6 MHz

4.2 Noise spectroscopy with the cold atoms

Although the frequency noise measurement using atomic transmission in the previous section indicated a satisfying results, FNPSDs show some discrepancies at higher frequencies (typically above 1 MHz). Fig. 4.22 displays some qualitative features at high frequencies. We realized that these features depend on the laser detuning and optical thickness of the atomic cloud. This part of the FNPSDs is limited by our detector bandwidth ($\simeq 6$ MHz). To resolve these features properly, we changed our photodiode with a larger bandwidth ($0.01 - 240$ MHz) and lower noise equivalent power (NEP) transimpedance photodiode provided by Laser Components company (model: A-CUBE-S500-240). One possibility which explains those features could be the impact of the broad Lorentzian wings in the optical spectrum of the lasers. These broad wings produce frequency noise at high frequencies. Even though the amplitude of this noise is much smaller than the main Gaussian part, it is enough to produce some spectroscopic features. For our DFB, the Lorentzian wings has typically 1000 times weaker noise power rather than the center of the Gaussian part.

Indeed, the broad wings behave such as a scanning frequency probe and perform spectroscopy. This is known as noise spectroscopy. In this type of spectroscopy, the laser frequency is neither scanned nor modulated. High resolution spectra in a wide radio-frequency range can be observed simultaneously by only frequency analyzing of the intensity fluctuations of the light transmitted through a sample [96]. Noise spectroscopy of an atomic transition have been applied in several experiments, usually using room temperature or hot vapors, for instance to perform spectroscopy of the Zeeman [96] or hyperfine levels [160, 161, 162], or study the effect of pressure on the spectroscopy [163], and observation of the electromagnetically induced transparency (EIT) [165]. However in this regime the Doppler effect has to be taken into account and limits the atomic spectral linewidth. On the other hand, cold atomic samples correspond to a system where the Doppler effect can generally be ignored, which improves the frequency to intensity noise conversion by reducing the atomic spectral linewidth.

In this section we predict the effect of the laser line-shape on the noise spectra in the transmission through the ^{85}Rb atoms, using phase modulation (PM) and amplitude modulation (AM) models.

4.2.1 Phase-modulation model

A simple approach to study the effect of noise on the transmitted intensity spectrum is modeled based on the phase modulation (PM) theory. The phase modulation at f_{n} is due to the carrier and two sidebands at $\nu_{\mathrm{L}} \pm f_{\mathrm{n}}$ as done in [158] (Fig. 4.23).

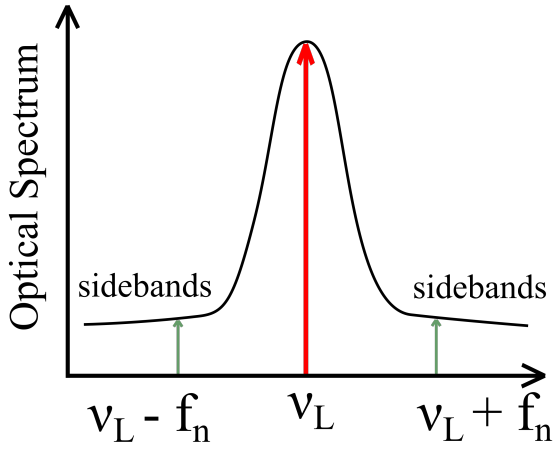

Figure 4.23 – Schematic of the phase modulation model by treating the broad optical spectrum wings as frequency sidebands. For more information see text.

The laser electric field with a phase modulating term can be written as

$$E(t) = E_0 e^{i[2\pi\nu_L t + \zeta \sin(2\pi f_n t)]}, \tag{4.39}$$

where ζ is the depth of the phase modulation. Thus the corresponding amplitude of the frequency noise at frequency f_n is ζf_n. Eq. 4.39 is expanded using the JacobiAnger expansion

$$E(t) = E_0 e^{i2\pi\nu_L t}\Big[J_0(\zeta) + \sum_{k=1}^{\infty} J_k(\zeta) e^{i2\pi k f_n t} + \sum_{k=1}^{\infty} J_{-k}(\zeta) e^{-i2\pi k f_n)t}\Big], \tag{4.40}$$

where $J_k(\zeta)$ is the k-th order Bessel functions and $J_{-k}(\zeta) = (-1)^k J_k(\zeta)$. Eq. 4.40 actually assumes infinite number of sidebands. Supposing a very small modulation depth $\zeta \ll 1$, Eq. 4.39 can be approximated by the Taylor expansion using only the first term

$$E(t) \simeq E_0 \left[e^{i2\pi\nu_L t} + \frac{\zeta}{2} e^{i2\pi(\nu_L + f_n)t} - \frac{\zeta}{2} e^{i2\pi(\nu_L - f_n)t}\right]. \tag{4.41}$$

The expression gives the main carrier frequency at ν_L with two small sidebands at $\nu_\pm = \nu_L \pm f_n$. The intensity is then given by

$$I(t) = |E|^2 = |E_0|^2 = I_0 = \text{const.} \tag{4.42}$$

The transmission of the electric field through the atoms is given by

$$E_t = E_i e^{i\gamma}, \tag{4.43}$$

where $\gamma = \phi + i\alpha/2$ is a phase which contains a dephasing ϕ and an absorption terms $\alpha/2$. According to the Beer-Lambart law (Eq. 3.12),

$$\begin{aligned} \gamma(x,y) &= -\frac{\sigma_0/2}{i+2\delta/\Gamma}\int dz\, n(x,y,z) \\ &= -\frac{\sigma_0/2}{1+(2\delta/\Gamma)^2}\Big(2\delta/\Gamma - i\Big)\int dz\, n(x,y,z), \end{aligned} \tag{4.44}$$

where $\delta = \nu_{\rm L} - \nu_0$ is the detuning of the laser carrier frequency from the atomic resonance and with z the propagation axis of the laser beam. Thus the dephasing and absorption will be defined as

$$\begin{aligned} \frac{\alpha(x,y)}{2} &= \frac{\sigma_0/2}{1+(2\delta/\Gamma)^2}\int dz\, n(x,y,z) \\ \phi(x,y) &= -\frac{\sigma_0\delta/\Gamma}{1+(2\delta/\Gamma)^2}\int dz\, n(x,y,z). \end{aligned} \tag{4.45}$$

Concerning the definition of optical thickness in Eq. 3.15, the above equations can be rewritten for $x = y = 0$, that is, at the center of the cloud

$$\begin{aligned} \alpha(\delta) &= b(\delta) = \frac{b_0}{1+4(\frac{\delta}{\Gamma})^2} \\ \phi(\delta) &= -b(\delta)\frac{\delta}{\Gamma}, \end{aligned} \tag{4.46}$$

with $b_0 = \sigma_0 \int dz n(x,y,z)$. Examples of phase shift and transmission as a function of laser detuning are depicted in Fig. 4.24 for three different cloud optical thicknesses. Note that the phase shift induced by the atoms can be larger than π. This makes a difference between the atoms and a Fabry-Perot cavity as frequency discriminators. In a Fabry-Perot cavity, the phase shift is given by $\phi(\delta) = \arctan(-2\delta/\Gamma_c)$ and is limited to a range between $-\pi$ to $+\pi$. For atomic clouds on the contrary there is no upper or lower bound for the phase shift. The transmitted intensity is given by

$$I_T = |E_t|^2 = I_i e^{-\alpha} = I_i e^{-b(\delta)}. \tag{4.47}$$

Combining Eqs. 4.43 and 4.46 one finds

$$\gamma = \frac{b_0}{1+4(\frac{\delta}{\Gamma})^2}\left(\frac{i}{2} - \frac{\delta}{\Gamma}\right). \tag{4.48}$$

Now considering the transmission of the phase modulated electric field introduced in Eq. 4.41, three components can be defined as the transmission

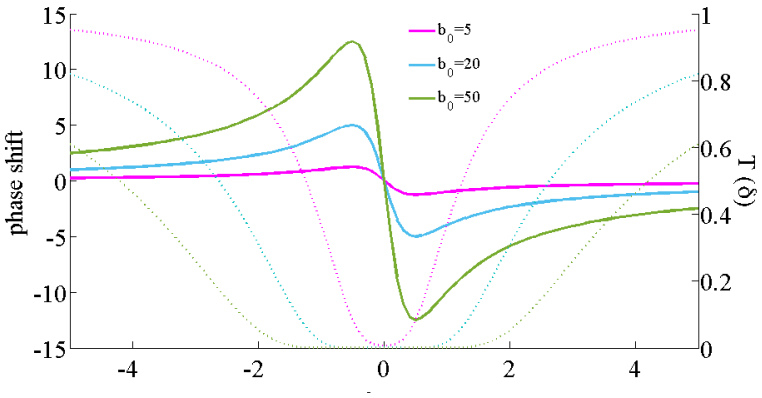

Figure 4.24 – Examples of phase shift $\phi(\delta)$ in radian and normalized transmission $T(\delta) = \exp[-\alpha(\delta)]$ as a function of laser detuning δ, for three different cloud optical thickness $b_0 = 5$, 20 and 50.

of a main carrier part in addition to two sidebands

$$\begin{aligned} E_{t,0} &= E_0 e^{i2\pi\nu_L t} e^{-\alpha_0/2} e^{i\phi_0} \\ E_{t,1} &= E_0 \frac{\zeta}{2} e^{i2\pi\nu_+ t} e^{-\alpha_1/2} e^{i\phi_1} \\ E_{t,-1} &= E_0 \frac{\zeta}{2} e^{i2\pi\nu_- t} e^{-\alpha_{-1}/2} e^{i\phi_{-1}}, \end{aligned} \tag{4.49}$$

with $\nu_\pm = \nu_\mathrm{L} \pm f_\mathrm{n}$ and

$$\begin{aligned} \alpha_0 &= \alpha(\delta) = b(\delta) \\ \alpha_1 &= \alpha(\delta + f_\mathrm{n}) = b(\delta + f_\mathrm{n}) \\ \alpha_{-1} &= \alpha(\delta - f_\mathrm{n}) = b(\delta - f_\mathrm{n}), \end{aligned} \tag{4.50}$$

and

$$\begin{aligned} \phi_0 &= \phi(\delta) = -b(\delta)\frac{\delta}{\Gamma} \\ \phi_1 &= \phi(\delta + f_\mathrm{n}) = -b(\delta + f_\mathrm{n})\frac{\delta + f_\mathrm{n}}{\Gamma} \\ \phi_{-1} &= \phi(\delta - f_\mathrm{n}) = -b(\delta - f_\mathrm{n})\frac{\delta - f_\mathrm{n}}{\Gamma}. \end{aligned} \tag{4.51}$$

Now neglecting all the ζ^2 terms ($\zeta \ll 1$) one obtains the transmitted intensity

$$\begin{aligned} I_T &= |E_{t,0} + E_{t,1} + E_{t,-1}|^2 \\ &= E_{t,0}E_{t,0}^* + E_{t,1}E_{t,0}^* + \mathrm{c.c} + E_{t,-1}E_{t,0}^* + \mathrm{c.c.} \end{aligned} \tag{4.52}$$

Replacing Eq. 4.49 in above expression leads to

$$\begin{aligned} I_T \quad &= |E_0|^2 e^{-\alpha_0} \quad + \frac{|E_0|^2\zeta}{2} e^{i(\phi_1-\phi_0+2\pi f_\mathrm{n} t)} e^{-\frac{\alpha_0+\alpha_1}{2}} + \text{c.c} \\ &\quad - \frac{|E_0|^2\zeta}{2} e^{i(\phi_{-1}-\phi_0-2\pi f_\mathrm{n} t)} e^{-\frac{\alpha_0+\alpha_{-1}}{2}} + \text{c.c.} \end{aligned} \tag{4.53}$$

Then this equation can be written as

$$\begin{aligned} I_T = I_0 e^{-\alpha_0} \Bigg(1 + \zeta \Big[\quad & \cos\left(\phi_1 - \phi_0 + 2\pi f_\mathrm{n} t\right) e^{\frac{\alpha_0-\alpha_1}{2}} \\ & - \cos\left(\phi_{-1} - \phi_0 - 2\pi f_\mathrm{n} t\right) e^{\frac{\alpha_0-\alpha_{-1}}{2}} \Big] \Bigg). \end{aligned} \tag{4.54}$$

The term $|E_0|^2 e^{-\alpha_0}$ in above equation describes the transmission of the main carrier part of the electric field, while the second and the third terms corresponds to the beat-note between the carrier and each sideband and can be described by an oscillatory function. Therefore the normalized time-dependent transmission in such system becomes

$$\frac{I_T(t)}{I_0} = T_0 \left[1 + \frac{\zeta}{\sqrt{T_0}} A \cos\left(\omega_\mathrm{n} t + \psi\right) \right], \tag{4.55}$$

where $\omega_\mathrm{n} = 2\pi f_\mathrm{n}$, $T_0 = e^{-\alpha_0}$, ψ is a phase and A is defined as

$$\begin{aligned} A\cos\left(\omega_\mathrm{n} t + \psi\right) = \quad & \cos\left(\phi_1 - \phi_0 + \omega_\mathrm{n} t\right) e^{-\frac{\alpha_1}{2}} \\ & - \cos\left(\phi_{-1} - \phi_0 - \omega_\mathrm{n} t\right) e^{-\frac{\alpha_{-1}}{2}}. \end{aligned} \tag{4.56}$$

At $t = 0$

$$A\cos\left(\psi\right) = \sqrt{T_1}\cos\left(\phi_1 - \phi_0\right) - \sqrt{T_{-1}}\cos\left(\phi_{-1} - \phi_0\right), \tag{4.57}$$

and at $\omega_\mathrm{n} t = \pi/2$

$$-A\sin\left(\psi\right) = \sqrt{T_1}\sin\left(\phi_0 - \phi_1\right) + \sqrt{T_{-1}}\sin\left(\phi_0 - \phi_{-1}\right), \tag{4.58}$$

with $T_1 = e^{-\alpha_1}$ and $T_{-1} = e^{-\alpha_{-1}}$. Therefore A is given by

$$A = \sqrt{T_1 + T_{-1} - 2\sqrt{T_1 T_{-1}}\cos\left(2\phi_0 - \phi_1 - \phi_{-1}\right)}. \tag{4.59}$$

The term $\zeta A\sqrt{T_0}$ describes the amplitude of the transmitted intensity at frequency f_n. Therefore the expected transmitted intensity noise is given by

$$S_T = \frac{1}{df}\left(\frac{\delta I_T}{I_0}\right)^2 = \frac{1}{df}\left(\zeta A\sqrt{T_0}\right)^2, \tag{4.60}$$

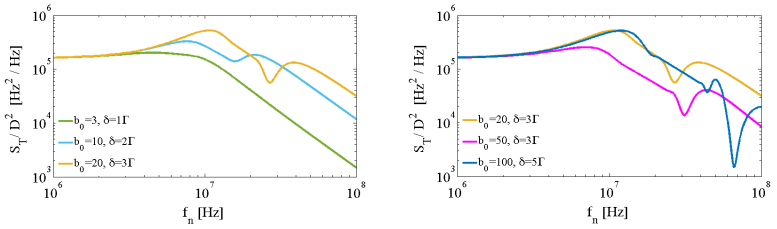

(a) (b)

Figure 4.25 – The simulation based on Eq. 4.61 for different optical thicknesses b_0 and laser detuning δ as mentioned in the figures legend. The optical thickness and detuning has been chosen to keep almost the best frequency to intensity noise conversion due to D^2.

where df is the frequency resolution of the oscilloscope. This model is used to calculate the expected noise of the transmitted intensity. Reminding Eq. 4.39, ζf_n is the amplitude of the frequency fluctuations at the sidebands frequency f_n. Thus $\zeta^2/df = S_{\nu_\mathrm{L}}(f_\mathrm{n})/f_\mathrm{n}^2$. Moreover the FNPSD measured with the Fabry-Perot indicated a white frequency noise for laser frequencies higher than 1 MHz. Hence in our model it was supposed that for $f_\mathrm{n} >$ 1 MHz the sidebands correspond only to the white frequency noise and have constant amplitude. So ζ is extracted from the measured FNPSD at $f_\mathrm{n} =$ 1 MHz, $S_{\nu_\mathrm{L}} \simeq 10^5\,[\mathrm{Hz}^2/\mathrm{Hz}]$ (Fig. 4.26). Finally applying Eqs. 4.37 and 4.38, the theoretical frequency to intensity noise conversion is obtained

$$S_{\nu_T}(f_\mathrm{n}) = \frac{S_T}{D^2} = \left(\frac{A\sqrt{T_0}}{f_\mathrm{n}}\right)^2 \frac{S_{\nu_\mathrm{L}}}{D^2}, \tag{4.61}$$

where

$$D^2 = \left(\frac{dT_\mathrm{a}}{d\delta}\right)^2. \tag{4.62}$$

Eq. 4.61 is plotted in Fig. 4.25 for several on-resonance optical thicknesses b_0 and laser detuning δ.

4.2.2 Experimental results

We can see in Fig. 4.22 that the PSDs differ at high frequencies, with in particular the appearance of a small "bump". However, these curves become limited by the noise floor of the photodiode for frequencies higher than 1 MHz. To overcome this problem, the photodiode and the amplifier have been replaced by a new photodiode, with a high cutoff frequency of 240 MHz and with a lower noise floor.

Typical FNPSDs, obtained with this low noise photodiode, are zoomed at high frequencies in Fig. 4.26. The three curves have been measured with

the same optical thickness $b_0 = 19$ but for three different laser detunings. We clearly see the appearance of bumps whose frequency positions depend on the laser detuning. These positions also depend on the optical thickness as shown in Fig. 4.30, where the frequency position of the first and second bump is plotted as a function of the laser detuning and for the three previous optical thicknesses.

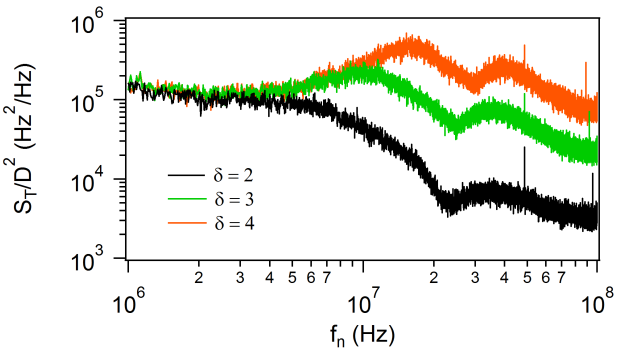

Figure 4.26 – Zoom at high frequencies of laser transmission noise PSD S_T divided by the square of the discriminator slope D^2 using a cold atomic cloud with an optical thickness of $b_0 = 19$ and for three different laser detunings.

A typical calculated and measured PSD is compared with the model in Fig. 4.27. The optical thickness is $b_0 = 19$ and the laser detuning is $\delta = 3$. We see a good overlap between the measured and the calculated PSD. In particular, the model predicts the existence of two bumps whose frequency positions correspond to the ones experimentally observed. These bumps are intrinsically related to the fact that we deal with frequency noise. On the contrary, as we will see in the next section, if we do the calculations assuming an incident laser with amplitude noise, one sees the appearance of dips instead of bumps. The presence of bumps or dips is thus a clear signature of the nature of the laser noise [166, 167].

In Fig. 4.28, the experimental and calculated transmission noise PSDs are plotted for different probe laser detuning but at a fix optical thickness $b_0 = 19$ in order to demonstrate the impact of the laser detuning on the bumps and dips features of the noise PSDs. Similarly, Fig. 4.29 shows the impact of the optical thickness ($b_0 = 19$ and 51) at a given laser detuning $\delta = 3\,\Gamma$. As a conclusion we observed a good agreement between the theoretical and the experimental results.

Finally, we have compared the measured and the calculated bump positions, corresponding to the frequency position of the local maxima, as a function of the laser detuning and for the three different optical thicknesses.

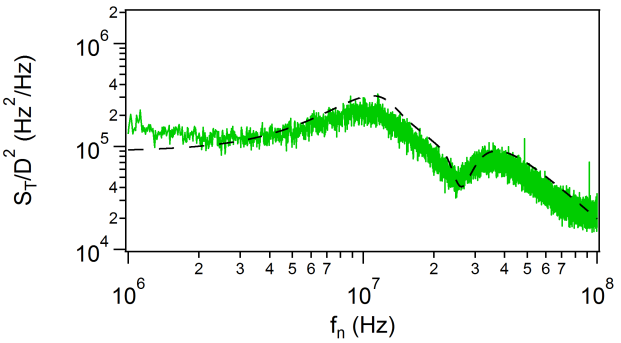

Figure 4.27 – Green solid line: laser transmission noise PSD S_T divided by the square of the discriminator slope $D^2 = (dT_a/d\delta)^2$ using a cold atomic cloud with an optical thickness of $b_0 = 19$ and a laser detuning of $\delta = 3$. Dashed line: $S_{\nu_{\mathrm{L,th}}}/D^2$ calculated using Eqs. 4.59 and 4.60 assuming a white frequency noise.

The results are plotted in Fig. 4.30. We obtain a very good agreement between measurements and calculations, validating the model used to understand the frequency to intensity noise conversion. We can also notice that the frequency difference between both bump positions remains constant, at least for sufficiently high laser detuning, and that this difference roughly corresponds to the frequency range where the transmission curve is closed to zero. Both bumps can thus be interpreted as one sideband going from one side of the transmission curve to the other [166, 167]. Fig. 4.31 describes an intuitive picture for the origin of the bumps in a noise spectrum.

4.2.3 Amplitude modulation model

Alternatively, we model the amplitude modulation.

$$E(t) = E_0 \left(1 + \varepsilon \cos\left(\omega_{\mathrm{n}} t\right)\right) e^{i\omega_L t}, \tag{4.63}$$

where ε is the amplitude of the modulation. Eq. 4.63 can be written as

$$E(t) = E_0 e^{i\omega_L t} + \frac{E_0 \varepsilon}{2}\left[e^{i\omega_+ t} + e^{i\omega_- t}\right]. \tag{4.64}$$

Eq. 4.64 shows two sidebands at $\omega_\pm = \omega_L \pm \omega_{\mathrm{n}}$. The intensity would be

$$I(t) = |E(t)|^2 = I_0 \left(1 + 2\varepsilon \cos(\omega_{\mathrm{n}} t) + |\varepsilon|^2 \cos^2(\omega_{\mathrm{n}} t)\right). \tag{4.65}$$

In case of weak modulation amplitude ($\varepsilon \ll 1$) Eq. 4.65 is approximated by

$$I(t) = I_0 \left(1 + 2\varepsilon \cos(\omega_{\mathrm{n}} t)\right). \tag{4.66}$$

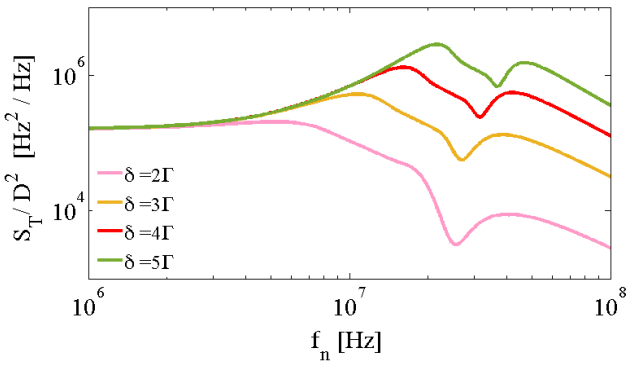

(a)

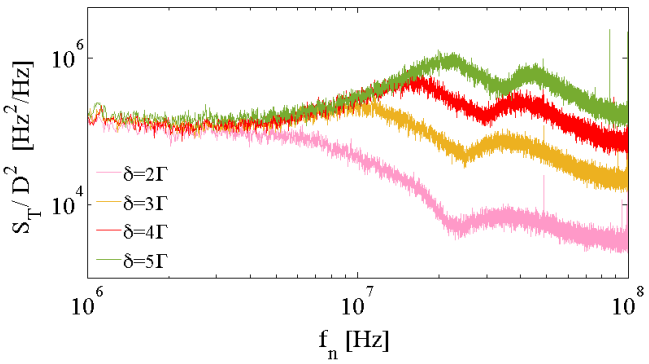

(b)

Figure 4.28 – Comparison of (a) calculated Eq. 4.61 and (b) experimental laser transmission noise PSD for optical thickness $b_0 = 19$ and detuning $\delta = 2, 3, 4, 5$.

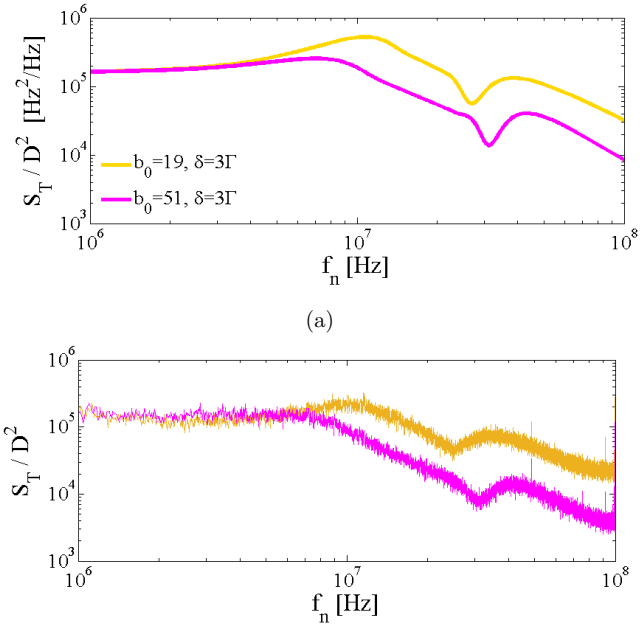

Figure 4.29 – Comparison of (a) calculated Eq. 4.61 and (b) experimental laser transmission noise PSD for optical thicknesses $b_0 = 19$ and $b_0 = 51$ and detuning $\delta = 3$.

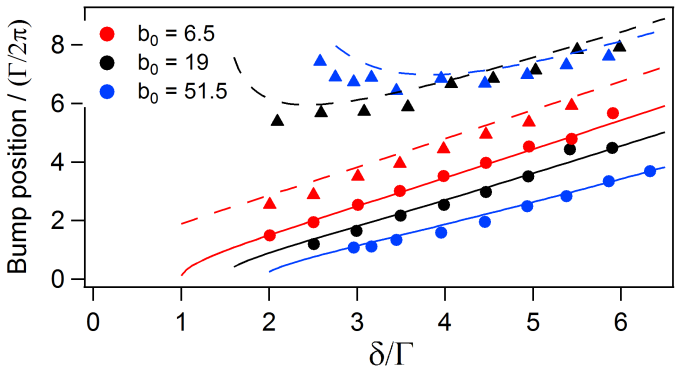

Figure 4.30 – Points: experimental frequency position of the bumps (circles: first bump, triangles: second bump) observed in the frequency noise PSD, obtained with the cold atomic cloud, as a function of the laser detuning. Solid line: calculated frequency position of the first bump. Dashed line: calculated frequency position of the second bump.

Using Eq. 4.43, and recalling Eqs. 4.50 and 4.51,

$$\begin{aligned} E_{t,0} &= E_0 e^{-\alpha_0/2} e^{i(\omega_L t+\phi_0)} \\ E_{t,1} &= E_0 \frac{\varepsilon}{2} e^{-\alpha_1/2} e^{i(\omega_+ t+\phi_1)} \\ E_{t,-1} &= E_0 \frac{\varepsilon}{2} e^{-\alpha_{-1}/2} e^{i(\omega_- t+\phi_{-1})}. \end{aligned} \tag{4.67}$$

Similar to the previous section, the transmitted intensity is given by

$$\frac{I_T(t)}{I_0} = T_0 \left[1 + \frac{\varepsilon}{\sqrt{T_0}} A' \cos\left(\omega_{\rm n} t + \psi\right)\right], \tag{4.68}$$

with

$$A' = \sqrt{T_1 + T_{-1} + 2\sqrt{T_1 T_{-1}} \cos\left(2\phi_0 - \phi_1 - \phi_{-1}\right)}, \tag{4.69}$$

and therefore the theoretical anticipated PSD of the normalized transmission would be

$$S_T = \frac{1}{df}\left(\frac{\delta I_T}{I_0}\right)^2 = \frac{\left(\varepsilon A' \sqrt{T_0}\right)^2}{df}. \tag{4.70}$$

In this model the amplitude of modulation ε is assumed to be white noise ($\varepsilon^2/df = \text{const}$). To compare the noise created by the amplitude modulation with the one created by phase modulation and also with our experimental measurements, ε can be extracted by

$$\frac{\varepsilon^2}{df} = S_T|_{f_{\rm n}=1\,\rm MHz}. \tag{4.71}$$

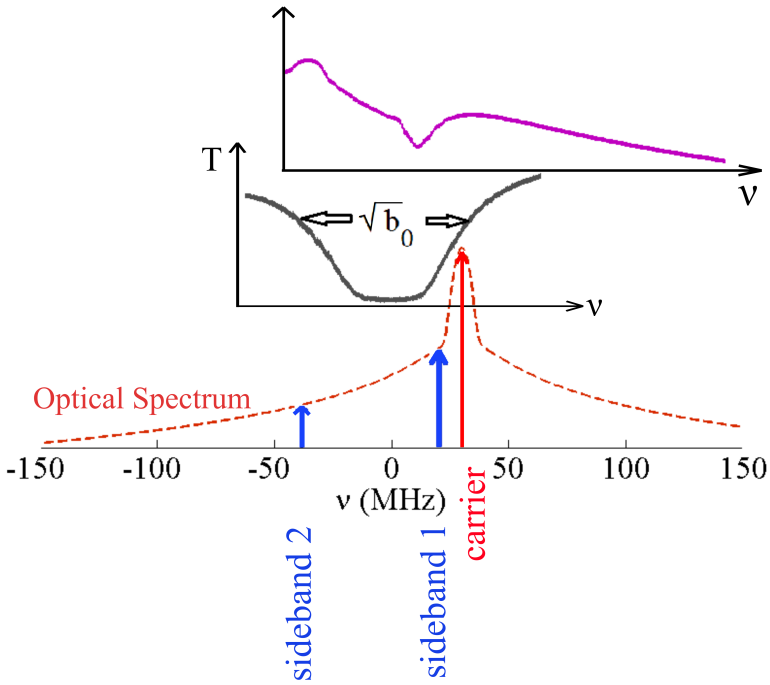

Figure 4.31 – An intuitive picture for the origin of the bumps in a transmission noise PSD. below, the laser optical spectrum at its carrier frequency is supposed to encounter a cloud of cold atoms with a transmission function T as described by the black curve in the center of the figure. The width of transmission curve scales as $\sqrt{b_0}$. This means that by increasing b_0, the width of transmission function increases proportional to $\sqrt{b_0}$. In the top a relevant transmission noise PSD is depicted. The bumps represent two group of sidebands in the laser optical spectrum which encounter two different sides of the transmission spectrum at about maximum frequency-to-intensity conversion. We observed that the space between two bumps changes proportional to $\sqrt{b_0}$.

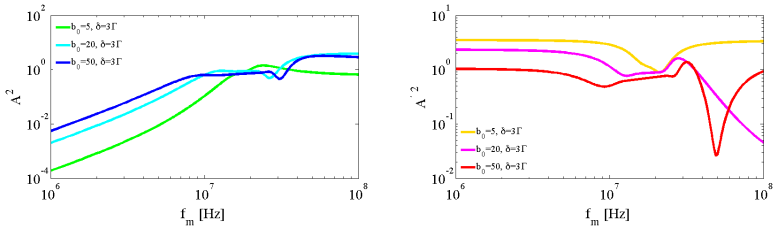

(a) (b)

Figure 4.32 – The calculation of (a) A^2 based on Eq. 4.59 and (b) A'^2 in Eq. 4.69 for optical thicknesses $b_0 = 5$, 20, 50 with the same detuning $\delta = 3\Gamma$. Note that A^2 has an overall behavior as $1/f_n^2$ at low frequencies while A'^2 is nearly flat.

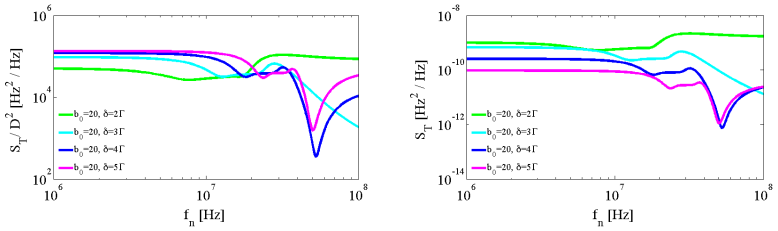

(a) (b)

Figure 4.33 – (a) The FNPSD and (b) the transmission intensity noise calculated based on amplitude modulation model in Eq. 4.72 and 4.70, for optical thickness $b_0 = 19$.

In order to compare the results with the experimental data, we use the same strategy as done in the previous section. Thus Eq. 4.70 is divided by the square of discriminator slope $D^2 = (dT_a/d\delta)^2$.

$$S_{\nu_T}(f_\mathrm{n}) = \frac{S_T}{D^2}. \tag{4.72}$$

Typical results are depicted in Fig. 4.33.

Figs. 4.34 shows clearly that the amplitude modulation does not match with the experimental results. As a conclusion, the noise of the DFB laser used in this experiment can be described by mainly the noise in the frequency of the laser and the intensity noise of the laser is negligible as expected from Sec. 4.1.1.

As done in Fig. 4.20, it is also possible to recover the M-shaped spectrum from the transmission noise PSD S_T, predicted by both amplitude and phase modulation, at low frequencies (typically at few MHz). Fig. 4.35a represents the value of the calculated transmission noise PSD S_T from Eqs. 4.60

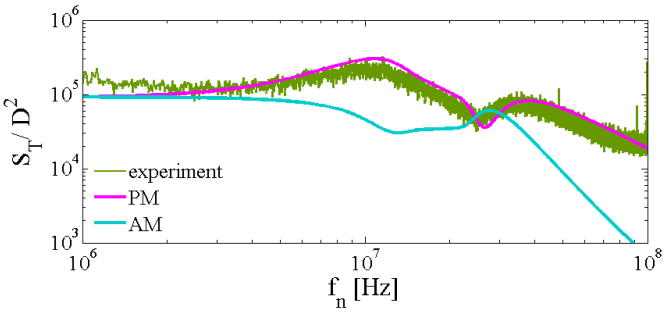

Figure 4.34 – Laser transmission noise PSD S_T divided by the square of the discriminator slope D^2 using a cold atomic cloud with an optical thickness of $b_0 = 19$ and a laser detuning of $\delta = 3\Gamma$. Experimental data (green), compared with theoretical simulation based on phase modulation (pink) and amplitude modulation models (blue).

and 4.70 at a certain frequency $f_n = 1\,\text{MHz}$ while the laser frequency is scanned around the atomic resonance. This figure shows that the strength of fluctuations in the transmitted intensity, in particular at low frequencies ($f_n < 4\,\text{MHz}$), varies in a same way as the square of derivative of the frequency discriminator D^2. At high frequencies however the M-shape might be distorted (Fig. 4.35b). This distortion might be due to the complicated bumps and dips features in the FNPSD.

Similarly, we can study the variation of the transmitted intensity noise at a particular frequency as a function of on-resonance optical thickness b_0 of a cloud. Fig. 4.36a demonstrates some examples of the transmission noise PSD for different b_0, and in Fig. 4.36b the variation of the noise level at two specific frequencies ($f_n = 1$ and $40\,\text{MHz}$) are depicted, which represent the behavior of S_T at low and high Fourier frequencies. Although at low frequencies the variation only shows a simple frequency-to-intensity conversion factor, at higher frequencies it demonstrates a more complicated oscillatory behavior related to the bumps and depths features in the noise spectra. A better understanding on the origin of the oscillation in Fig. 4.36b for example, needs further investigations.

4.3 Conclusion

In this chapter, we have studied the intensity noise of a laser beam transmitted through a cold atomic cloud. In this forward configuration, we have observed the conversion of the intrinsic laser frequency noise to intensity noise, the atomic transition playing the role of a frequency discriminator whose slope is adjustable through the optical thickness. While we recover

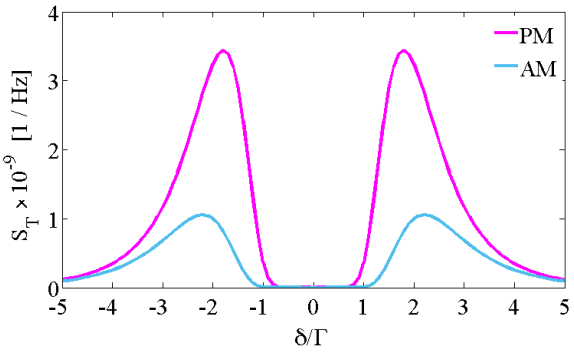

(a)

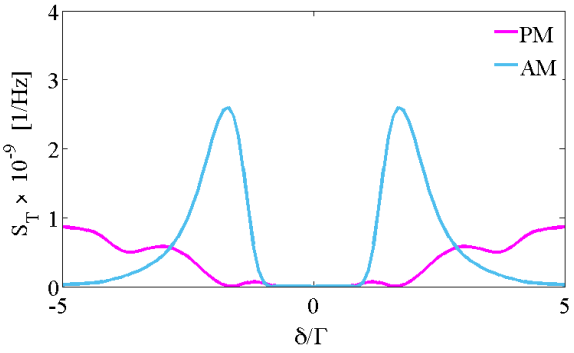

(b)

Figure 4.35 – Transmitted intensity noise PSD S_T calculated based on phase and amplitude modulation models in Eqs. 4.60 and 4.70 at a given frequency (a) $f_{\mathrm{n}} = 1\,\mathrm{MHz}$ and (b) $f_{\mathrm{n}} = 30\,\mathrm{MHz}$ while the detuning δ is scanned between -5 to $5\,\Gamma$. The optical thickness $b_0 = 19$. The noise created by phase modulation is larger than the one generated by amplitude modulation. At high frequencies, the M-shaped spectrum corresponding to phase modulation is distorted. This might be due to the complicated bumps and dips features in the spectrum and the dependence of their positions to the different detunings.

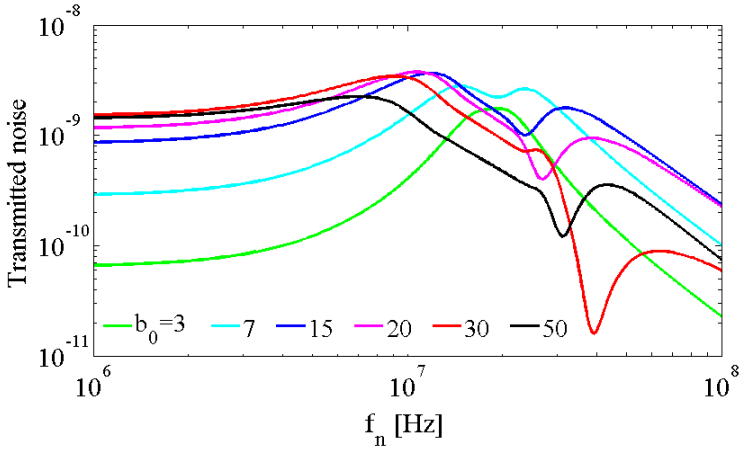

(a)

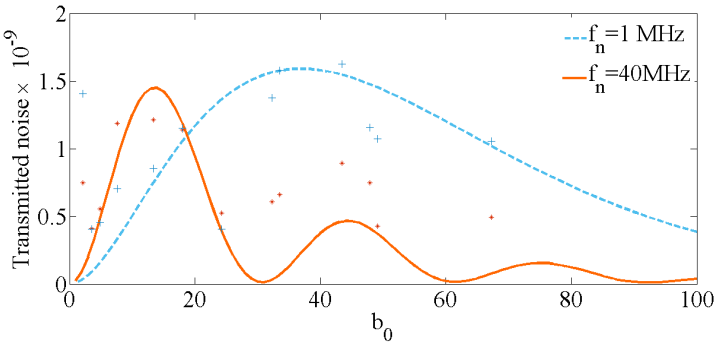

(b)

Figure 4.36 – (a) Transmitted intensity noise PSD S_T for different optical thicknesses $b_0 = 3$, 7, 15, 20, 30 and 50. Note that here the intensity noise PSD after transmission is not normalized by the derivative of the frequency discriminator. (b) The noise power at $f_n = 1\,\text{MHz}$ (dashed blue line) and $f_n = 40\,\text{MHz}$ (solid orange line) as a function of b_0 computed by the phase modulation model. The blue plus and orange star symbols correspond to experimental measurements. The experimental data confirms the prediction from computations. The deviation between computation and experimental data at $f_n = 40\,\text{MHz}$ could be due to the noise floor of our detection system. In this measurement, b_0 was modified by applying different TOF durations to a cold-atom cloud (i.e. Fig. 3.26).

the same FNPSD at low Fourier frequencies using a Fabry-Perot cavity, some differences appear at higher Fourier frequencies and one needs to go beyond the linear response of the discriminator. We have shown that a simple model in which the frequency noise is modeled as a carrier with two sidebands and the atomic cloud as a medium with an index of refraction is sufficient to describe the observations.

The conversion of the laser frequency noise to intensity noise can be used to characterize the laser noise. Conversely, if the laser frequency noise spectrum is known, one can exploit the frequency to intensity noise conversion to extract information on the discriminator medium itself. We have seen that the frequency positions of the bumps in the FNPSD depend on the laser detuning from the atomic transition and on the optical thickness. One could thus imagine to extract the two last quantities by directly measuring one FNPSD instead of measuring the entire transmission curve by scanning the laser frequency around the atomic transition.

The frequency noise in the transmission converts to intensity noise and as we showed by the phase modulation model the intensity noise PSD represents the atomic spectrum. When the intensity noise of the incident laser is dominant, based on the amplitude modulation model, we showed the transmitted intensity noise corresponding to a same atomic sample represents a different qualitative features. Indeed based on those qualitative features, one can infer the type of dominant noise in the incident laser. This picture however, has to be modified in an atomic sample with a large optical thickness, $b(\delta) \gg 1$, or in the case of very large atomic sample [168].

Finally, in the forward direction, the conversion of the intrinsic laser frequency noise to intensity noise is usually one of the main process. A good understanding of this effect is thus of crucial importance. With this conversion now well characterized, intensity noise measurements could possibly be used to extract some signatures of more involved phenomena, such as the observation of the influence of atomic motion.

Chapter 5

Conclusion and outlook

Conclusion

This thesis has presented my work on characterization of the noise in light scattered by a cloud of cold rubidium atoms in forward direction. Part of my work as a PhD student during the last three years has consisted in manipulating the cold-atom experiment and upgrading the experimental setup. We have installed a noise detection setup in the transmission geometry in order to study the noise induced by cold atoms on a probe laser beam. We characterized first the laser noises, as well as its line shape and linewidth. Finally we studied the effect of laser frequency and intensity noises in the transmission. Using a basic mathematical model, we succeeded in demonstrating noise spectroscopy of a hyperfine level in a large cloud of cold ^{85}Rb atoms.

In chapter 2 of this manuscript, random laser was introduced. It is a laser which is based on highly disordered gain medium. No cavity is needed to generate random lasing. Thus its spatial and spectral modes are completely different from the conventional lasers. Here the multiple scattering provides feedback and determines the spectral modes of the emission. Although some theoretical and experimental works have shown that random laser emission is partially coherent, its coherence is reduced compared to conventional lasers. Due to sophisticated properties of multiple scattering, there is no precise conclusion about the coherence of random laser yet, and it needs further studies in this field.

Although cold-atom random laser has been observed in our team, coherence measurements can support the prior observation in a more direct fashion.

In chapter 3 our experimental setup of the magneto-optical trap (MOT) was described. We have a ^{85}Rb MOT with $\sim 10^{10}$ atoms, optical thickness $b_0 = 100$, size $\sigma = 1$ mm, and temperature $100\,\mu$K. The setup was equipped with an offset lock system, to stabilize and control the laser frequency of the cooling beams as well as pump and probe beams. This is important for maintaining the intensity and frequency of pump beams unchanged when the Raman beam is swept across the resonance in order to generate and observe a random laser. Moreover some useful technical informations

regarding the control and characterization of MOT were explained.

To understand the noise imprinted by the atoms to a light beam propagating through the MOT, first one needs to characterize the intrinsic noises which exist in the incident light. These noises can nontrivially evolve and be converted to other types of noise after interaction with atoms. By applying a so-called β-separation line approach, the linewidth of the laser was estimated from the frequency noise power spectral density (PSD). The result confirmed the beat-note measurements.

Similarly, the frequency noise of a laser can be also measured in forward direction using the atomic resonance as the frequency discriminator. In chapter 4 we reported our frequency noise measurement using the MOT. The Doppler effect is negligible and the hyperfine transitions can convert the fluctuations in the frequency into intensity ones. One interesting feature of cold atoms is that by controlling the optical thickness of the cloud one can change the efficiency of this frequency to intensity noise conversion. This is analogous to changing the cavity linewidth. Similar to the Fabry-Perot cavity the laser frequency noise was measured and consequently applying the β-line separation approach, the laser linewidth was estimated with a good agreement with the other results.

The broad wings of the laser optical spectrum is considered as a frequency span. Thus one can perform spectroscopy even with a fixed laser frequency. This is known as noise spectroscopy [96]. The noise in the transmitted laser through a cloud of cold atoms was modeled based on the phase modulation. The resulting sidebands simulate the large optical spectrum wings. Analogously the amplitude modulation can make similar sidebands and can describe noise spectroscopy. However the final results have qualitatively different features. Using both phase and amplitude modulation models and comparing with the experimental results we succeeded in performing noise spectroscopy of a hyperfine level of a large cloud of rubidium atoms. The qualitative and quantitative understanding of the frequency-to-intensity noise conversion will be helpful in any experiment where a laser beam is detected after transmission through a cloud of cold atoms, even though the modeling presented in this thesis does not yet account for the Zeeman degeneracy.

Outlook

Several practical coherence measurement techniques have been already performed in the cold-atom community to characterize the scattered light through the MOT in a single scattering regime. However to understand the coherence properties of cold-atom random laser, we proposed to begin

with determining the coherence properties of light multiply scattered by the atoms. Diffusing-wave spectroscopy (DWS) is an optical technique which deals with the dynamics of the scattered light in the limit of strong scattering [169]. This technique allows to probe the displacements of the scatterers with very high precision. DWS can be applied to the scattered light by cold atoms. As DWS probes tiny displacements of the scatterers and also the efficiency of this technique depends on the mean number of scattering events, any variation in the temperature and optical thickness of the cloud can lead to a significant change in the results.

As explained in Sec. 2.1.4, one interesting measurement can be done by studying the photon statistics of cold atom random lasers. As shown by Cao et al. [13], the photon statistics of the random laser below and above lasing threshold are governed by Bose-Einstein and Poisson statistics respectively.

One can also perform temporal intensity correlation measurements in a photon counting regime. Extracting coherence time for different optical thickness b_0, might reflect some information about the impact of the threshold on the random laser coherence.

Bibliography

[1] V. Letokhov, "Generation of light by a scattering medium with negative resonance absorption," Sov. J. Exp. Theor. Phys. **26**, 835 (1968).

[2] H. Cao, "Lasing in random media," Waves in random media **13**, R1–R39 (2003).

[3] A. F. Molisch and B. P. Oehry, *Radiation trapping in atomic vapours* (Oxford University Press, 1998).

[4] Q. Baudouin, N. Mercadier, V. Guarrera, W. Guerin, and R. Kaiser, "A cold-atom random laser," Nat. Phys. **9**, 357–360 (2013).

[5] H. Weaver, D. R. Williams, N. Dieter, and W. Lum, "Observations of a strong unidentified microwave line and of emission from the oh molecule," Nature **208**, 29–31 (1965).

[6] M. Johnson, A. Betz, R. McLaren, C. Townes, and E. Sutton, "Nonthermal 10 micron co2 emission lines in the atmospheres of mars and venus," ApJ **208**, L145–L148 (1976).

[7] M. J. Mumma, D. Buhl, G. Chin, D. Deming, F. Espenak, T. Kostiuk, and D. Zipoy, "Discovery of natural gain amplification in the 10-micrometer carbon dioxide laser bands on mars: a natural laser," Science **212**, 45–49 (1981).

[8] V. Strelnitski, M. R. Haas, H. A. Smith, E. F. Erickson, S. W. Colgan, and D. J. Hollenbach, "Far-infrared hydrogen lasers in the peculiar star mwc 349a," (1996).

[9] J. J. Goldstein, M. J. Mumma, T. Kostiuk, D. Deming, F. Espenak, and D. Zipoy, "Absolute wind velocities in the lower thermosphere of venus using infrared heterodyne spectroscopy," Icarus **94**, 45–63 (1991).

[10] V. Letokhov and S. Johansson, *Astrophysical lasers* (Oxford University Press, 2008).

[11] B. Sherwood, "Engineering planetary lasers for interstellar communication. ms thesis," (1988).

[12] G. Zacharakis, N. A. Papadogiannis, G. Filippidis, and T. G. Papazoglou, "Photon statistics of laserlike emission from polymeric scattering gain media," Opt. Lett. **25**, 923–925 (2000).

[13] H. Cao, Y. Ling, J. Xu, C. Cao, and P. Kumar, "Photon statistics of random lasers with resonant feedback," Phys. Rev. Lett. **86**, 4524 (2001).

[14] M. Patra, "Theory for photon statistics of random lasers," Phys. Rev. A **65**, 043809 (2002).

[15] C. Westbrook, R. Watts, C. Tanner, S. Rolston, W. Phillips, P. Lett, and P. Gould, "Localization of atoms in a three-dimensional standing wave," Phys. Rev. Lett. **65**, 33 (1990).

[16] C. Jurczak, K. Sengstock, R. Kaiser, N. Vansteenkiste, C. Westbrook, and A. Aspect, "Observation of intensity correlations in the fluorescence from laser cooled atoms," Opt. Commun. **115**, 480–484 (1995).

[17] S. Bali, D. Hoffmann, J. Simán, and T. Walker, "Measurements of intensity correlations of scattered light from laser-cooled atoms," Phys. Rev. A **53**, 3469 (1996).

[18] D. S. Wiersma, M. v. Albada, and A. Lagendijk, "Random laser?" Nature **373**, 203–204 (1995).

[19] D. Wiersma, "Laser physics: The smallest random laser," Nature **406**, 132–135 (2000).

[20] N. M. Lawandy, R. Balachandran, A. Gomes, and E. Sauvain, "Laser action in strongly scattering media," Nature **368**, 436–438 (1994).

[21] S. John, "Localization of light," Phys. Today **44**, 32–40 (1991).

[22] Y. Kuga and A. Ishimaru, "Retroreflectance from a dense distribution of spherical particles," J. Opt. Soc. Am. A **1**, 831–835 (1984).

[23] P.-E. Wolf and G. Maret, "Weak localization and coherent backscattering of photons in disordered media," Phys. Rev. Lett. **55**, 2696 (1985).

[24] M. P. Van Albada and A. Lagendijk, "Observation of weak localization of light in a random medium," Phys. Rev. Lett. **55**, 2692 (1985).

[25] J. Zhu, D. Pine, and D. Weitz, "Internal reflection of diffusive light in random media," Phys. Rev. A **44**, 3948 (1991).

[26] H. Cao, Y. Zhao, S. Ho, E. Seelig, Q. Wang, and R. Chang, "Random laser action in semiconductor powder," Phys. Rev. Lett. **82**, 2278 (1999).

[27] H. Cao, Y. Zhao, H. Ong, S. Ho, J. Y. Dai, J. Y. Wu, and R. Chang, "Ultraviolet lasing in resonators formed by scattering in semiconductor polycrystalline films," Appl. Phys. Lett. **73**, 3656–3658 (1998).

[28] S. Frolov, Z. V. Vardeny, K. Yoshino, A. Zakhidov, and R. Baughman, "Stimulated emission in high-gain organic media," Phys. Rev. B **59**, R5284 (1999).

[29] H. Cao, J. Xu, S.-H. Chang, and S. Ho, "Transition from amplified spontaneous emission to laser action in strongly scattering media," Phys. Rev. E **61**, 1985 (2000).

[30] H. Cao, J. Xu, D. Zhang, S.-H. Chang, S. Ho, E. Seelig, X. Liu, and R. Chang, "Spatial confinement of laser light in active random media," Phys. Rev. Lett. **84**, 5584 (2000).

[31] X. Jiang and C. Soukoulis, "Time dependent theory for random lasers," Phys. Rev. Lett. **85**, 70 (2000).

[32] A. Burin, M. Ratner, H. Cao, and R. Chang, "Model for a random laser," Phys. Rev. Lett. **87**, 215503 (2001).

[33] V. Apalkov, M. Raikh, and B. Shapiro, "Random resonators and prelocalized modes in disordered dielectric films," Phys. Rev. Lett. **89**, 016802 (2002).

[34] M. Patra, "Decay rate distributions of disordered slabs and application to random lasers," Phys. Rev. E **67**, 016603 (2003).

[35] L. Florescu and S. John, "Photon statistics and coherence in light emission from a random laser," Phys. Rev. Lett. **93**, 013602 (2004).

[36] R. Loudon, *The quantum theory of light* (Oxford University Press, 2000).

[37] R. Lang, M. O. Scully, and W. E. Lamb Jr, "Why is the laser line so narrow? a theory of single-quasimode laser operation," Phys. Rev. A **7**, 1788 (1973).

[38] D. S. Wiersma, "The physics and applications of random lasers," Nat. Phys. **4**, 359–367 (2008).

[39] M. Fox, *Quantum Optics: An Introduction: An Introduction* (Oxford University Press, 2006).

[40] U. Fano, "Ionization yield of radiations. ii. the fluctuations of the number of ions," Phys. Rev. **72**, 26 (1947).

[41] K. Shimoda, H. Takahasi, and C. H. Townes, "Fluctuations in amplification of quanta with application to maser amplifiers," Journal of the Physical Society of Japan **12**, 686–700 (1957).

[42] S. García-Revilla, J. Fernández, M. Barredo-Zuriarrain, E. Pecoraro, M. Arriandiaga, I. Iparraguirre, J. Azkargorta, and R. Balda, "Coherence characteristics of random lasing in a dye doped hybrid powder," J. Lumin. **169**, 472–477 (2016).

[43] M. A. Webster, K. J. Webb, A. M. Weiner, J. Xu, and H. Cao, "Temporal response of a random medium from speckle intensity frequency correlations," J. Opt. Soc. Am. A **20**, 2057–2070 (2003).

[44] J. C. Dainty, "Stellar speckle interferometry," in "Laser speckle and related phenomena," (Springer, 1975), pp. 255–280.

[45] J. W. Goodman, "Some fundamental properties of speckle," J. Opt. Soc. Am. **66**, 1145–1150 (1976).

[46] M. Noginov, S. Egarievwe, N. Noginova, H. Caulfield, and J. Wang, "Interferometric studies of coherence in a powder laser," Optical Materials **12**, 127–134 (1999).

[47] H. Cao, Y. Ling, J. Xu, and A. Burin, "Probing localized states with spectrally resolved speckle techniques," Phys. Rev. E **66**, 025601 (2002).

[48] G. van Soest, F. J. Poelwijk, and A. Lagendijk, "Speckle experiments in random lasers," Phys. Rev. E **65**, 046603 (2002).

[49] C. Gouedard, F. Auzel, A. Migus, D. Husson, and C. Sauteret, "Generation of spatially incoherent short pulses in laser-pumped neodymium stoichiometric crystals and powders," J. Opt. Soc. Am. B **10**, 2358–2363 (1993).

[50] S. Der, B. Redman, and R. Chellappa, "Simulation of error in optical radar range measurements," Appl. Opt. **36**, 6869–6874 (1997).

[51] B. Karamata, P. Lambelet, M. Laubscher, R. Salathé, and T. Lasser, "Spatially incoherent illumination as a mechanism for cross-talk suppression in wide-field optical coherence tomography," Opt. Lett. **29**, 736–738 (2004).

[52] B. Redding, M. A. Choma, and H. Cao, "Spatial coherence of random laser emission," Opt. Lett. **36**, 3404–3406 (2011).

[53] W. Z. W. Ismail, D. Liu, S. Clement, D. W. Coutts, E. M. Goldys, and J. M. Dawes, "Spectral and coherence signatures of threshold in random lasers," J. Opt. **16**, 105008 (2014).

[54] V. M. Papadakis, A. Stassinopoulos, D. Anglos, S. H. Anastasiadis, E. P. Giannelis, and D. G. Papazoglou, "Single-shot temporal coherence measurements of random lasing media," J. Opt. Soc. Am. B **24**, 31–36 (2007).

[55] Q. Baudouin, W. Guerin, and R. Kaiser, "Cold and hot atomic vapors: a testbed for astrophysics?" Annual Review of Cold Atoms and Molecules **2**.

[56] G. Labeyrie, E. Vaujour, C. A. Mueller, D. Delande, C. Miniatura, D. Wilkowski, and R. Kaiser, "Slow diffusion of light in a cold atomic cloud," Phys. Rev. Lett. **91**, 223904 (2003).

[57] J. Tabosa, G. Chen, Z. Hu, R. Lee, and H. Kimble, "Nonlinear spectroscopy of cold atoms in a spontaneous-force optical trap," Phys. Rev. Lett. **66**, 3245 (1991).

[58] D. Grison, B. Lounis, C. Salomon, J. Courtois, and G. Grynberg, "Raman spectroscopy of cesium atoms in a laser trap," Europhys. Lett. **15**, 149 (1991).

[59] T. M. Brzozowski, M. Brzozowska, J. Zachorowski, M. Zawada, and W. Gawlik, "Probe spectroscopy in an operating magneto-optical trap: The role of raman transitions between discrete and continuum atomic states," Phys. Rev. A **71**, 013401 (2005).

[60] W. Guerin, F. Michaud, and R. Kaiser, "Mechanisms for lasing with cold atoms as the gain medium," Phys. Rev. Lett. **101**, 093002 (2008).

[61] L. Hilico, C. Fabre, and E. Giacobino, "Operation of a cold-atom laser in a magneto-optical trap," Europhys. Lett. **18**, 685 (1992).

[62] W. Guerin, N. Mercadier, F. Michaud, D. Brivio, R. Carminati, V. Eremeev, A. Goetschy, S. Skipetrov, R. Kaiser *et al.*, "Towards a random laser with cold atoms," J. Opt. **12**, 024002 (2010).

[63] J. McKeever, A. Boca, A. D. Boozer, J. R. Buck, and H. J. Kimble, "Experimental realization of a one-atom laser in the regime of strong coupling," Nature **425**, 268–271 (2003).

[64] G. Vrijsen, O. Hosten, J. Lee, S. Bernon, and M. A. Kasevich, "Raman lasing with a cold atom gain medium in a high-finesse optical cavity," Phys. Rev. Lett. **107**, 063904 (2011).

[65] J. G. Bohnet, Z. Chen, J. M. Weiner, D. Meiser, M. J. Holland, and J. K. Thompson, "A steady-state superradiant laser with less than one intracavity photon," Nature **484**, 78–81 (2012).

[66] B. Mollow, "Stimulated emission and absorption near resonance for driven systems," Phys. Rev. A **5**, 2217 (1972).

[67] A. Yariv and D. M. Pepper, "Amplified reflection, phase conjugation, and oscillation in degenerate four-wave mixing," Opt. Lett. **1**, 16–18 (1977).

[68] N. Mercadier, *Diffusion résonante de la lumière: laser aléatoire à atomes et vols de Lévy des photons* (PhD thesis, Université Nice Sophia Antipolis, 2011).

[69] F. Michaud, *Diffusion multiple de la lumière en présence de gain dans un nuage d'atomes froids : vers un laser aléatoire* (PhD thesis, Université Nice Sophia Antipolis, 2008).

[70] G. L. Gattobigio, *Manipulation of a Large Magneto-Optical Trap: application to Four-Wave Mixing* (PhD thesis, Università degli Studi di Ferrara, 2008).

[71] K. M. Case and P. F. Zweifel, *Linear transport theory* (Addison-Wesley Pub. Co., 1967).

[72] K. Drozdowicz, E. Krynicka, and J. Dabrowska, "Diffusion cooling of thermal neutrons in basic rock minerals by monte carlo simulation of the pulsed neutron experiments," Applied radiation and isotopes **58**, 727–733 (2003).

[73] S. Chandrasekhar, *Radiative transfer, ed* (New York: Dover, 1960).

[74] R. Elaloufi, R. Carminati, and J.-J. Greffet, "Diffusive-to-ballistic transition in dynamic light transmission through thin scattering slabs: a radiative transfer approach," J. Opt. Soc. Am. A **21**, 1430–1437 (2004).

[75] N. Lavrinovich and V. Letokhov, "The possibility of the laser effect in stellar atmospheres," Zh. Eksp. Teor. Fiz. **67**, 1609–1620 (1974).

[76] S. Johansson and V. Letokhov, "Astrophysical lasers and nonlinear optical effects in space," New Astronomy Reviews **51**, 443–523 (2007).

[77] V. V. Sobolev, "A treatise on radiative transfer." Princeton, NJ, Van Nostrand **1** (1963).

[78] W. Unno and E. Spiegel, "The eddington approximation in the radiative heat equation," Publ. Astron. Soc. Japan **18**, 85 (1966).

[79] W. Guerin, Y. Chong, Q. Baudouin, M. Liertzer, S. Rotter, and R. Kaiser, "Diffusive to quasi-ballistic random laser: incoherent and coherent models," arXiv preprint arXiv:1606.03679 (2016).

[80] A. Lagendijk and B. A. Van Tiggelen, "Resonant multiple scattering of light," Phys. Rep. **270**, 143–215 (1996).

[81] L. S. Froufe-Pérez, W. Guerin, R. Carminati, and R. Kaiser, "Threshold of a random laser with cold atoms," Phys. Rev. Lett. **102**, 173903 (2009).

[82] J. D. Jackson, *Classical electrodynamics* (Wiley, New York, 1999), 3rd ed.

[83] W. Guerin, N. Mercadier, D. Brivio, and R. Kaiser, "Threshold of a random laser based on raman gain in cold atoms," Opt. Express **17**, 11236–11245 (2009).

[84] A. Goetschy and S. Skipetrov, "Euclidean matrix theory of random lasing in a cloud of cold atoms," Europhys. Lett. **96**, 34005 (2011).

[85] H.-A. Bachor and T. C. Ralph, *A guide to experiments in quantum optics* (Wiley, 2004).

[86] Q. Baudouin, *Lumière dans des vapeurs atomiques opaques: piégeage radiatif, laser aléatoire et vols de Lévy* (PhD thesis, Université Nice Sophia Antipolis, 2013).

[87] R. H. Brown and R. Q. Twiss, "Correlation between photons in two coherent beams of light," Nature **177**, 27–29 (1956).

[88] D. Kleppner, "Hanbury brown's steamroller," Phys. Today **61**, 8 (2008).

[89] B. Mollow, "Power spectrum of light scattered by two-level systems," Phys. Rev. **188** (1969).

[90] B. Gao, "Effects of zeeman degeneracy on the steady-state properties of an atom interacting with a near-resonant laser field: Resonance fluorescence," Phys. Rev. A **50**, 4139 (1994).

[91] K. Nakayama, Y. Yoshikawa, H. Matsumoto, Y. Torii, and T. Kuga, "Precise intensity correlation measurement for atomic resonance fluorescence from optical molasses," Opt. Express **18**, 6604–6612 (2010).

[92] M. Shafi, D. Pandey, and H. Ramachandran, "Time-delayed intensity-interferometry with light from laser-cooled atoms," in "International Conference on Fibre Optics and Photonics," (Optical Society of America, 2014), pp. S5A–83.

[93] K. M. Shafi, D. Pandey, B. Suryabrahmam, B. Girish, and H. Ramachandran, "Time-delayed intensity–interferometry of the

emission from ultracold atoms in a steady-state magneto-optical trap," J. Phys. B **49**, 025301 (2015).

[94] S. Yoon, Y. Choi, S. Kang, W.-R. Kim, J.-R. Kim, and K. An, "Fluorescence spectra of atomic ensembles in a magneto-optical trap as an optical lattice," arXiv preprint arXiv:1504.00623 (2015).

[95] H. Florez, L. Cruz, M. de Miranda, R. de Oliveira, J. Tabosa, M. Martinelli, and D. Felinto, "Power-broadening-free correlation spectroscopy in cold atoms," Phys. Rev. A **88**, 033812 (2013).

[96] T. Yabuzaki, T. Mitsui, and U. Tanaka, "New type of high-resolution spectroscopy with a diode laser," Phys. Rev. Lett. **67**, 2453 (1991).

[97] G. Labeyrie, F. De Tomasi, J.-C. Bernard, C. Müller, C. Miniatura, and R. Kaiser, "Coherent backscattering of light by cold atoms," Phys. Rev. Lett. **83**, 5266 (1999).

[98] G. Labeyrie, D. Delande, C. A. Mueller, C. Miniatura, and R. Kaiser, "Coherent backscattering of light by cold atoms: Theory meets experiment," Europhys. Lett. **61**, 327 (2003).

[99] G. Labeyrie, F. Michaud, and R. Kaiser, "Self-sustained oscillations in a large magneto-optical trap," Phys. Rev. Lett. **96**, 023003 (2006).

[100] G. Gattobigio, T. Pohl, G. Labeyrie, and R. Kaiser, "Scaling laws for large magneto-optical traps," Phys. Scripta **81**, 025301 (2010).

[101] D. A. Steck, "Rubidium 85 d line data (2008)," URL http://steck.us/alkalidata/rubidium85numbers. pdf. Rubidium **85**.

[102] A. Camara, R. Kaiser, and G. Labeyrie, "Scaling behavior of a very large magneto-optical trap," Physical Review A **90**, 063404 (2014).

[103] "https://www.sacher-laser.com, technical report," .

[104] G. Puentes, "Laser frequency offset locking scheme for high-field imaging of cold atoms," Appl. Phys. B **107**, 11–16 (2012).

[105] D. Aktas, *Upgrade of a cold-atom experimental setup for the study of random lasers* (MSc thesis, Université Nice Sophia Antipolis, 2008).

[106] "www.ozoptics.com, oz optics ltd." .

[107] T. Walker, D. Sesko, and C. Wieman, "Collective behavior of optically trapped neutral atoms," Phys. Rev. Lett. **64**, 408 (1990).

[108] W. Petrich, M. H. Anderson, J. R. Ensher, and E. A. Cornell, "Behavior of atoms in a compressed magneto-optical trap," J. Opt. Soc. Am. B **11**, 1332–1335 (1994).

[109] M. T. DePue, S. L. Winoto, D. Han, and D. S. Weiss, "Transient compression of a mot and high intensity fluorescent imaging of optically thick clouds of atoms," Opt. Commun. **180**, 73–79 (2000).

[110] W. Ketterle, K. B. Davis, M. A. Joffe, A. Martin, and D. E. Pritchard, "High densities of cold atoms in a dark spontaneous-force optical trap," Phys. Rev. Lett. **70**, 2253 (1993).

[111] M. Anderson, W. Petrich, J. Ensher, and E. Cornell, "Reduction of light-assisted collisional loss rate from a low-pressure vapor-cell trap," Phys. Rev. A **50**, R3597 (1994).

[112] C. Townsend, N. Edwards, K. Zetie, C. Cooper, J. Rink, and C. Foot, "High-density trapping of cesium atoms in a dark magneto-optical trap," Phys. Rev. A **53**, 1702 (1996).

[113] S. Chu, L. Hollberg, J. E. Bjorkholm, A. Cable, and A. Ashkin, "Three-dimensional viscous confinement and cooling of atoms by resonance radiation pressure," Phys. Rev. Lett. **55**, 48 (1985).

[114] J. Dalibard and C. Cohen-Tannoudji, "Laser cooling below the doppler limit by polarization gradients: simple theoretical models," J. Opt. Soc. Am. B **6**, 2023–2045 (1989).

[115] D. S. Weiss, E. Riis, Y. Shevy, P. J. Ungar, and S. Chu, "Optical molasses and multilevel atoms: experiment," J. Opt. Soc. Am. B **6**, 2072–2083 (1989).

[116] P. D. Lett, W. D. Phillips, S. Rolston, C. E. Tanner, R. Watts, and C. Westbrook, "Optical molasses," J. Opt. Soc. Am. B **6**, 2084–2107 (1989).

[117] G. Reinaudi, T. Lahaye, Z. Wang, and D. Guéry-Odelin, "Strong saturation absorption imaging of dense clouds of ultracold atoms," Opt. Lett. **32**, 3143–3145 (2007).

[118] "http://www.hellma-worldwide.de, technical report," .

[119] D. Hoffmann, P. Feng, R. Williamson III, and T. Walker, "Excited-state collisions of trapped rb 85 atoms," Phys. Rev. Lett. **69**, 753 (1992).

[120] S. Gensemer, V. Sanchez-Villicana, K. Tan, T. T. Grove, and P. Gould, "Trap-loss collisions of 85 rb and 87 rb: Dependence on trap parameters," Phys. Rev. A **56**, 4055 (1997).

[121] C. Jurczak, B. Desruelle, K. Sengstock, J. Y. Courtois, C. I. Westbrook, and A. Aspect, "Atomic transport in an optical lattice: An

investigation through polarization-selective intensity correlations," Phys. Rev. Lett. **77**, 1727–1730 (1996).

[122] J. A. Grover, P. Solano, L. A. Orozco, and S. L. Rolston, "Photon-correlation measurements of atomic-cloud temperature using an optical nanofiber," Phys. Rev. A **92**, 013850 (2015).

[123] C. A. Müller, B. Grémaud, and C. Miniatura, "Speckle-intensity correlations of photons scattered by cold atoms," Phys. Rev. A **92**, 013819 (2015).

[124] A. Lambrecht, T. Coudreau, A. M. Steinberg, and E. Giacobino, "Squeezing with cold atoms," Europhys. Lett. **36**, 93–98 (1996).

[125] J. Ries, B. Brezger, and A. I. Lvovsky, "Experimental vacuum squeezing in rubidium vapor via self-rotation," Phys. Rev. A **68**, 025801 (2003).

[126] A. Lezama, R. Rebhi, A. Kastberg, S. Tanzilli, and R. Kaiser, "Fluctuation properties of laser light after interaction with an atomic system: Comparison between two-level and multilevel atomic transitions," Phys. Rev. A **92**, 033853 (2015).

[127] T. Peyronel, O. Firstenberg, Q.-Y. Liang, S. Hofferberth, A. V. Gorshkov, T. Pohl, M. D. Lukin, and V. Vuletić, "Quantum nonlinear optics with single photons enabled by strongly interacting atoms," Nature **488**, 57 (2012).

[128] J. R. Ott, M. Wubs, P. Lodahl, N. A. Mortensen, and R. Kaiser, "Cooperative fluorescence from a strongly driven dilute cloud of atoms," Phys. Rev. A **87**, 061801 (2013).

[129] D. J. Pine, D. A. Weitz, P. M. Chaikin, and E. Herbolzheimer, "Diffusing wave spectroscopy," Phys. Rev. Lett. **60**, 1134–1137 (1988).

[130] T. Takano, M. Fuyama, R. Namiki, and Y. Takahashi, "Spin squeezing of a cold atomic ensemble with the nuclear spin of one-half," Phys. Rev. Lett. **102**, 033601 (2009).

[131] P. Dumont, F. Camargo, J.-M. Danet, D. Holleville, S. Guerandel, G. Pillet, G. Baili, L. Morvan, D. Dolfi, I. Gozhyk *et al.*, "Low-noise dual-frequency laser for compact cs atomic clocks," Journal of Lightwave Technology **32**, 3817–3823 (2014).

[132] K. Döringshoff, I. Ernsting, R.-H. Rinkleff, S. Schiller, and A. Wicht, "Low-noise, tunable diode laser for ultra-high-resolution spectroscopy," Opt. Lett. **32**, 2876–2878 (2007).

[133] T. Nazarova, C. Lisdat, F. Riehle, and U. Sterr, "Low-frequency-noise diode laser for atom interferometry," J. Opt. Soc. Am. B **25**, 1632–1638 (2008).

[134] J. Pfeifle, A. Coillet, R. Henriet, K. Saleh, P. Schindler, C. Weimann, W. Freude, I. V. Balakireva, L. Larger, C. Koos *et al.*, "Optimally coherent kerr combs generated with crystalline whispering gallery mode resonators for ultrahigh capacity fiber communications," Phys. Rev. Lett. **114**, 093902 (2015).

[135] X. Baillard, A. Gauguet, S. Bize, P. Lemonde, P. Laurent, A. Clairon, and P. Rosenbusch, "Interference-filter-stabilized external-cavity diode lasers," Opt. Commun. **266**, 609–613 (2006).

[136] S. Kraft, A. Deninger, F. Lison, C. Zimmermann *et al.*, "Rubidium spectroscopy at 778? 780 nm with a distributed feedback laser diode," Laser Phys. Lett. **2**, 71 (2004).

[137] F. Riehle, *Frequency standards: basics and applications* (John Wiley & Sons, 2006).

[138] D. Elliott, R. Roy, and S. Smith, "Extracavity laser band-shape and bandwidth modification," Phys. Rev. A **26**, 12 (1982).

[139] G. Di Domenico, S. Schilt, and P. Thomann, "Simple approach to the relation between laser frequency noise and laser line shape," Appl. Opt. **49**, 4801–4807 (2010).

[140] N. Bucalovic, V. Dolgovskiy, C. Schori, P. Thomann, G. Di Domenico, and S. Schilt, "Experimental validation of a simple approximation to determine the linewidth of a laser from its frequency noise spectrum," Appl. Opt. **51**, 4582–4588 (2012).

[141] O. Llopis, P. H. Merrer, H. Brahimi, K. Saleh, and P. Lacroix, "Phase noise measurement of a narrow linewidth cw laser using delay line approaches," Opt. Lett. **36**, 2713–2715 (2011).

[142] N. Bucalovic, V. Dolgovskiy, C. Schori, P. Thomann, G. D. Domenico, and S. Schilt, "Experimental validation of a simple approximation to determine the linewidth of a laser from its frequency noise spectrum," Appl. Opt. **51**, 4582–4588 (2012).

[143] H. Dinesan, E. Fasci, A. D'Addio, A. Castrillo, and L. Gianfrani, "Characterization of the frequency stability of an optical frequency standard at 1.39 µm based upon noise-immune cavity-enhanced optical heterodyne molecular spectroscopy," Opt. Express **23**, 1757–1766 (2015).

[144] I. Ricciardi, S. Mosca, M. Parisi, P. Maddaloni, L. Santamaria, P. D. Natale, and M. D. Rosa, "Sub-kilohertz linewidth narrowing of a mid-infrared optical parametric oscillator idler frequency by direct cavity stabilization," Opt. Lett. **40**, 4743–4746 (2015).

[145] Q. Zhou, J. Qin, W. Xie, Z. Liu, Y. Tong, Y. Dong, and W. Hu, "Power-area method to precisely estimate laser linewidth from its frequency-noise spectrum," Appl. Opt. **54**, 8282–8289 (2015).

[146] Q. Zhou, J. Qin, W. Xie, Z. Liu, Y. Tong, Y. Dong, and W. Hu, "Dynamic frequency-noise spectrum measurement for a frequency-swept dfb laser with short-delayed self-heterodyne method," Opt. Express **23**, 29245–29257 (2015).

[147] B. C. Young, F. C. Cruz, W. M. Itano, and J. C. Bergquist, "Visible lasers with subhertz linewidths," Phys. Rev. Lett. **82**, 3799–3802 (1999).

[148] T. Yabuzaki, T. Mitsui, and U. Tanaka, "New type of high-resolution spectroscopy with a diode laser," Phys. Rev. Lett. **67**, 2453–2456 (1991).

[149] R. Walser and P. Zoller, "Laser-noise-induced polarization fluctuations as a spectroscopic tool," Phys. Rev. A **49**, 5067–5077 (1994).

[150] I. V. Jyotsna, G. S. Agarwal, and G. Vemuri, "Deriving spectroscopic information from intensity-intensity correlations," Phys. Rev. A **51**, 3169–3173 (1995).

[151] K. V. Vasavada, G. Vemuri, and G. S. Agarwal, "Diode-laser-noise-based spectroscopy of allowed and crossover resonances," Phys. Rev. A **52**, 4159–4166 (1995).

[152] T. L. Myers, R. M. Williams, M. S. Taubman, C. Gmachl, F. Capasso, D. L. Sivco, J. N. Baillargeon, and A. Y. Cho, "Free-running frequency stability of mid-infrared quantum cascade lasers," Opt. Lett. **27**, 170–172 (2002).

[153] S. Bartalini, S. Borri, P. Cancio, A. Castrillo, I. Galli, G. Giusfredi, D. Mazzotti, L. Gianfrani, and P. De Natale, "Observing the intrinsic linewidth of a quantum-cascade laser: Beyond the schawlow-townes limit," Phys. Rev. Lett. **104**, 083904 (2010).

[154] R. J. McLean, C. E. Fairchild, P. L. Dyson, and P. Hannaford, "Tunable diode-laser heterodyne spectroscopy of atmospheric oxygen," Opt. Lett. **18**, 1675–1677 (1993).

[155] M. Rosenbluh, A. Rosenhouse-Dantsker, A. Wilson-Gordon, M. Levenson, and R. Walser, "Spectroscopy with diode-laser noise," Opt. Commun. **146**, 158 – 162 (1998).

[156] D. H. McIntyre, J. Cooper, R. Walser, and C. E. Fairchild, "Diode-laser noise spectroscopy of rubidium," Opt. Lett. **18**, 1816–1818 (1993).

[157] J. C. Camparo and J. G. Coffer, "Conversion of laser phase noise to amplitude noise in a resonant atomic vapor: The role of laser linewidth," Phys. Rev. A **59**, 728–735 (1999).

[158] M. Bahoura and A. Clairon, "Diode-laser noise conversion in an optically dense atomic sample," Opt. Lett. **26**, 926–928 (2001).

[159] J. J. Townsend, J. G. Coffer, and J. C. Camparo, "Breakdown of the born approximation in laser phase-noise to amplitude-noise conversion," Phys. Rev. A **72**, 033807 (2005).

[160] J. C. Camparo and J. G. Coffer, "Conversion of laser phase noise to amplitude noise in a resonant atomic vapor: The role of laser linewidth," Phys. Rev. A **59**, 728 (1999).

[161] M. Bahoura and A. Clairon, "Diode-laser noise conversion in an optically dense atomic sample," Opt. Lett. **26**, 926–928 (2001).

[162] M. Rosenbluh, A. Rosenhouse-Dantsker, A. Wilson-Gordon, M. Levenson, and R. Walser, "Spectroscopy with diode-laser noise," Opt. Commun. **146**, 158–162 (1998).

[163] J. G. Coffer, M. Anderson, and J. C. Camparo, "Collisional dephasing and the reduction of laser phase-noise to amplitude-noise conversion in a resonant atomic vapor," Phys. Rev. A **65**, 033807 (2002).

[164] Q. Zhou, J. Qin, W. Xie, Z. Liu, Y. Tong, Y. Dong, and W. Hu, "Power-area method to precisely estimate laser linewidth from its frequency-noise spectrum," Appl. Opt. **54**, 8282–8289 (2015).

[165] V. A. Sautenkov, H. Li, Y. V. Rostovtsev, and M. O. Scully, "Power spectra and correlations of intensity fluctuations in electromagnetically induced transparency," J. Mod. Optic. **54**, 2451–2457 (2007).

[166] S. V. Kashanian, A. Eloy, W. Guerin, M. Lintz, M. Fouché, and R. Kaiser, "Noise spectroscopy with large clouds of cold atoms," to appear in Phys. Rev. A (2016).

[167] S. V. Kashanian, A. Eloy, W. Guerin, M. Lintz, M. Fouché, and R. Kaiser, "Noise spectroscopy with large clouds of cold atoms," arXiv preprint arXiv:1606.07658 (2016).

[168] J. Townsend, J. Coffer, and J. Camparo, "Breakdown of the born approximation in laser phase-noise to amplitude-noise conversion," Phys. Rev. A **72**, 033807 (2005).

[169] G. Maret and P. Wolf, "Multiple light scattering from disordered media. the effect of brownian motion of scatterers," Z. Phys. B Cond. Mat. **65**, 409–413 (1987).